Universität Augsburg
University of Manchester Institute of
Science and Technology

Investigation of Intermittent Transport Events in Toroidal Confinement Systems

Diplom thesis
by Werner Schabert
November 2001

Lehrstuhl für Experimentelle Plasmaphysik Universität Augsburg
Department of Physics UMIST
Department of Mathematics UMIST

Acknowledgements

I would like to thank the following people for their invaluable assistance during the course of this diplom thesis:

- Prof. Dr.-Ing. Kurt Behringer for his support and for the reading and correction of this thesis.
- Prof. Dr. Gert-Ludwig Ingold for the reading and correction of this thesis.
- Prof. PhD Dave Broomhead and Prof. PhD Jan Hugill for their continuous support and guidance. Also for checking and reading this thesis.
- Dr. Jerry Huke, Dr. Nikita Sidorov, Dr. Sergei Fedotov and Danny Pudjianto for their support and hospitality throughout my thesis.
- The other members of the Departments of Mathematics and Physics for their support.

Contents

1 Introduction

The discovery of the H- or high confinement mode by the ASDEX group [1] has led to a variety of experimental and theoretical study of this phenomenon. The H-mode is an improved confinement regime for tokamak reactors in which the performance of individual devices improves typically by a factor of two or more. It is characterized by steep gradients in density and temperature indicating the existence of a transport barrier in the plasma edge. Therefore the fusion capabilities of future tokamaks can be greatly enhanced if they can access this operational regime. Since the basic processes that cause the plasma to perform the transition to the H-mode are not clearly identified the qualitative and quantitative understanding of the physics of this transition is an important issue for the design of future fusion reactors.

Although the overall performance improves during the H-mode this operating regime is not without problems. The H-mode is often perturbed by a intermittent series of relaxation oscillations known as ELMs. ELMs show bursts of MHD activity and a fast (0.1 ms) loss of particles and energy from the plasma. In many experiments stationary ELM-free H-modes could not be obtained. Although ELMs seem at first to be a disadvantage of the H-mode they could improve the fusion capability of tokamaks since they could release particles from the plasma in a controlled way. This gives a strong motivation for the investigation and control of the ELMs. A summary of the properties and present understanding of the H-mode and of the ELMs is given in section 2.

The analytical understanding of the H-mode and the ELMs can benefit from the fact that the dynamics of plasmas can in many cases be reduced to low-dimensional mathematical models. In this case the complex behaviour of the plasma can be described by simple models. An important technique for obtaining details of the dynamics of the plasma from measured data is given by the method of delays, which is described in section 3. The key idea of this method is to create a dynamical system that shows qualitatively the same behaviour as the investigated plasma. Thus the study of this dynamical system allows us to investigate the physical process in great detail and to obtain qualitative and quantitative results.

For the investigation of the plasma dynamics, data from COMPASS-D has been used. COMPASS-D is a divertor tokamak with a magnetic field topology that is very similar to that proposed for ITER (see section 4). Since a high time resolution is necessary for quantitative results the time derivative of the magnetic field was investigated, which was sampled with a frequency of 200 kHz. The data indicates the presence of several modes during the L-H transition and the H-mode. To estimate the time evolution and stability of these modes the time dependence of the growth and decay rates was calculated. Section 5 deals with the linear and nonlinear analysis of these modes.

In order to compare the results found by the analysis of the experimental data with existing models a closer look at L-H transition and ELM models is done in section 6. Since the main interest of this section lies in the qualitative behaviour of the models, the discussion focuses on their mathematical description. It turns out that the majority of them are based on the same partial differential equations for the pressure and the plasma velocity. Since these equations play a central role for the further comparison, a discussion of their limitations will be given.

In sections 7 and 8 two different classes of low-dimensional models derived from these equations are presented. For the first class, the pressure and the plasma velocity are approximated by different sets of orthogonal functions. The second class defines new quantities of the plasma, based on spatial integrals over the region of the transport barrier, and derives equations for the evolution of them. The comparison of the properties of these models with the results of section 5 identifies a model due to Sugama and Horton as the most promising candidate to describe the L-H transition and the ELMs. Section 8 gives a detailed discussion of the properties of this model.

2 Transitions from L-mode to H-mode and Edge Localized Modes

2.1 A short introduction to magnetically confined fusion plasmas

The following introduction to magnetically confined fusion plasmas concentrates on the aspects needed for the understanding of the later work. As such, it is by no means a complete introduction to the properties of plasmas. A more detailed introduction - on which this summary is based - can be found in [2].

Generally speaking a plasma is an ionized gas. When a gas is heated up strongly enough for its atoms and molecules to collide with sufficient energy to knock off their electrons, a plasma is formed. A plasma is often called the 'fourth state of matter' and consists of three parts: the electron gas, the ion gas and the gas consisting of neutral particles. The term gas is used since in many cases the electrons, ions and neutral particles can be described as an ideal gas. In nature plasmas can be found very often, indeed, most of the known matter in the Universe is in the plasma state. As there are almost equally many negative and positive particles inside the plasma, macroscopically the plasma appears to be neutral although microscopically there are deviations from the neutrality. Because of the free electrons and ions the plasma is conducting and magnetic and electric fields exert forces upon the plasma. In contrast to gases, where the forces act on a short range, in a plasma the electromagnetic forces can affect charged particles over a long distance.

Plasmas have a wide range of practical applications. In nuclear fusion a plasma of deuterium and tritium is heated up to the temperatures necessary for the fusion reactions to start. During the fusion the following reaction happens

$$D + T \rightarrow {}^{4}_{2}He + n + 17.6MeV \tag{1}$$

The neutron carries the major part of the released energy and can leave the plasma easily. Its energy is used for the generation of electric energy. The α-particle's energy is needed to heat up the plasma. On its way out of the plasma it collides with deuterium and tritium and loses its energy. Since the temperature of the plasma is very high ($\geq$ 10 keV) the plasma must be confined in a toroidal magnetic cage. To obtain a good confinement of the plasma, the magnetic field lines are closed and move helically on magnetic flux surfaces around the axis of the torus. For nuclear fusion two different types of fusion reactors are proposed, the tokamak and the stellarator. The difference between these two types lies in the creation of the magnetic cage. While in stellarators the magnetic field

is created only by coils, the tokamak creates the poloidal magnetic field with a current inside the plasma. Figure 1 shows a typical tokamak reactor.

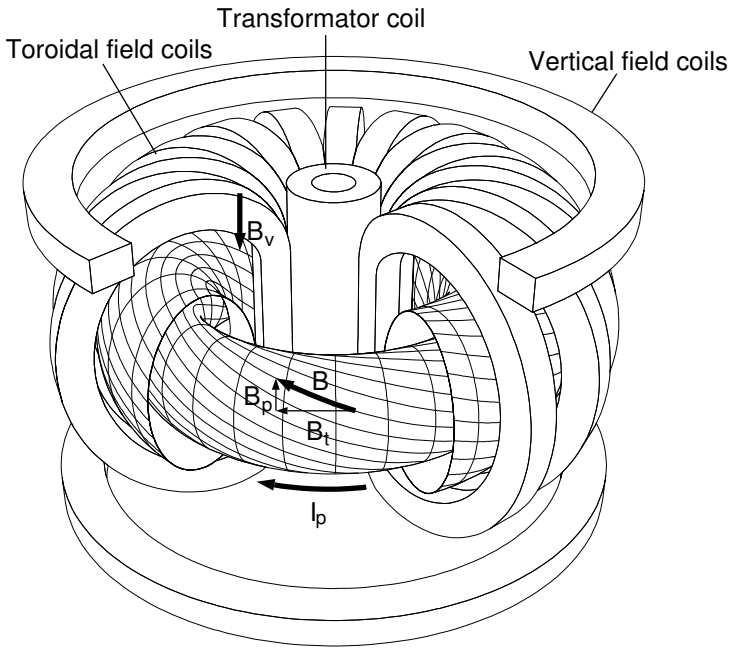

Figure 1: Schematic view of a tokamak reactor. The magnetic field lines move helically around the torus on magnetic flux surfaces.

Because of the toroidal form of the cage non-Cartesian coordinate systems are used very often. Figure 2 shows two typically coordinate systems. The first coordinate system $(\vec{e}_\Phi, \vec{e}_\Theta, \vec{e}_r)$ is similar to the cylindrical coordinate system, the only difference is that the z-axis is not a real axis and forms a circle. Φ is called the toroidal and Θ the poloidal angle. $\vec{e}_r$ points normally out of the torus. The second coordinate system $(\vec{e}_\parallel, \vec{e}_\perp, \vec{e}_r)$ is closely related to the magnetic cage. $\vec{e}_{||}$ points in the direction of the magnetic field and $\vec{e}_r$ points normally out of the torus. The last basis vector $\vec{e}_\perp$ is parallel to the magnetic surface and points in the direction necessary to form a orthogonal right hand side system.

Since the confinement of the plasma is not perfect, particles can escape from the plasma, leading to a decrease in the plasma energy and an enhanced H_α/D_α-light of the recombining hydrogen/deuterium atoms. Because of their high kinetic energy, the escaping particles can hit the walls of the reactor and cause damage to them. Hereby particles of the wall, the so called impurity ions, are released which can enter the plasma resulting in a decrease of the plasma temperature. To control the escape of the particles from and the entry of impurity ions into the plasma the outer field lines are open and start and end on special plates, the

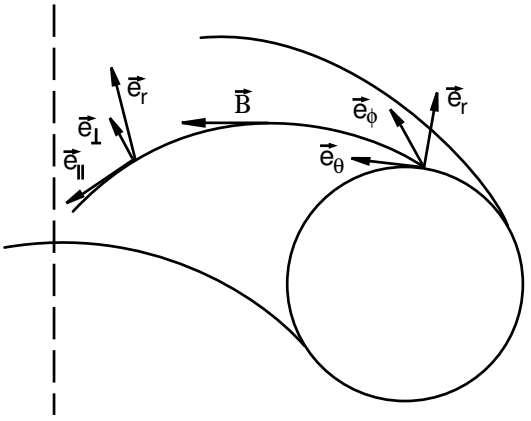

Figure 2: Two typical coordinate systems used in magnetically confined nuclear fusion.

divertor plates. The closed field lines are separated from the closed ones by a separatrix.

In plasmas with magnetic confinement two different confinement modes can be distinguished: A low confinement mode called L-mode and a high confinement mode called H-mode. The properties of these two confinement modes are discussed in the next section.

2.2 L-mode and H-mode

The L-mode was the typical confinement mode for tokamak plasmas until the discovery of the H-mode by the ASDEX team. The L-mode can be characterized by poor confinement that becomes worse with increasing heating of the plasma [1]. In L-mode plasmas turbulence occurs throughout the plasma with broad frequency and wave number spectra [3]. The relative level of the turbulence has a maximum near the plasma boundary and can approach 100%. In some plasmas more than half of the particle losses are associated with high peaks of the fluctuations.

In the H-mode, the confinement of the plasma is enhanced. The energy confinement improves by a factor of 2, resulting in a decrease of the intensity of the Balmer lines of hydrogenic neutrals at the boundary, signifying a decrease in the neutral recycling rate and thus a decrease in the particle outflux [4]. The transition from L- to H-mode is accompanied by the formation of a pedestal due to steep gradients in the electron temperature and in the electron density in the plasma edge a few centimetres inside the separatrix. The region between the pedestal and the scrape-off layer is referred to as a transport barrier where the particle and energy transport is significantly reduced [3]. The H-mode can be reached in a wide variety of toroidal confined systems, however there is a strong link to divertor tokamaks with a separatrix [5]. Experiments indicate the existence of a critical heating power for the transition into H-mode. This critical

heating power increases with electron density, magnetic field, and the size of the tokamak. Recent experiments indicate a lower limit for the density below which the H-mode cannot be reached [6]. In numerous experiments a hysteresis between the forward L-H transition and the backward H-L transition has been observed [7]. This hysteresis manifests itself in a much lower critical heating power for the H-L transition than for the L-H transition. Additionally the pressure gradient and the electron density show differences between the two transition.

For the transition from L- to H-mode a large number of different theories exist. One common idea of many of these theories is the stabilization of at least one plasma instability during the transition. However this instability is not identified and many theories, based on different instabilities, exist. As a consequence the stabilization mechanism is unknown, but most theories explain the suppression of turbulence by a shear in the $E \times B$-drift velocity [8]. This drift affects all particles in the same way, independent of their charge or mass. Due to the velocity shear turbulence become decorrelated and thus particle transport across magnetic field lines reduces significantly. Although this velocity shear can explain the transition it is still unknown what kind of mechanism creates the shear.

2.3 Edge localized modes

A characteristic of the H-mode is the occurrence of an intermittent instability in the plasma edge, the so-called edge localized modes (ELMs). In toroidal magnetic fusion devices a number of ELM types occur during the L-H transition and during H-mode [9]. Although the following classification is widely accepted, the terminology for the description of ELMs varies. To prevent misunderstandings the name ELM is used here for the short burst of MHD activity and particle loss. The cycle between two successive ELMs is called the ELM-cycle. During ELMs the loss of energy and particles increases suddenly, reducing the average global confinement by 10-20% [10]. This particle loss leads to an increase in electron temperature outside the separatrix and a spike in the H_α-signal due to recycling of expelled plasma particles. The plasma core inside the separatrix is only weakly affected by ELMs. Different types of ELMs can be distinguished [11]:

- At the L-H transition dithering cycles occur. Since the edge pressure and current gradients are close to their L-mode values the dithering cycles are not specific MHD instabilities, but back-and-forth transitions between L- and H-modes.
- With increasing power type III or small ELMs are encountered. The repetition frequency of the type III ELMs decreases with increasing heating power until they disappear above a critical heating power. Before an ELM, coherent structures known as precursors are encountered.

- At higher power levels larger amplitude ELMs, the type I or giant ELMs, are observed. Their repetition frequency increases with increasing applied power. For these ELMs precursors have been found, too.
- A further class of ELMs are the type II or grassy ELMs. Type II ELMs occur in tokamaks with higher elongation and triangularity and high edge pressure. Here the edge plasma is in the connection regime between the first and second stable region of ideal MHD stability at the plasma edge.

Figure 3 shows the typical sequence of ELMs during a power rise in DIII-D. With stepwise increasing heating power, first type III ELMs occur at the transition from L- to H-mode. Their repetition frequency decreases with heating power until an ELM-free period is reached. At higher heating powers Type I ELMs occur. Their repetition frequency is now increasing with increasing heating power.

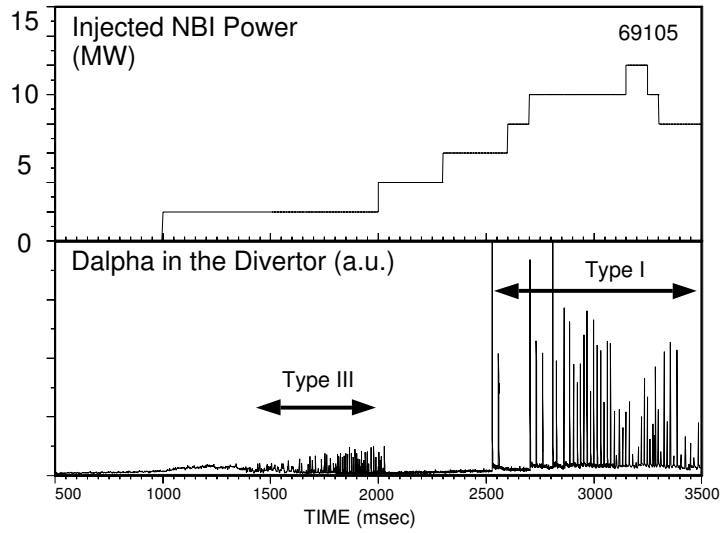

Figure 3: Time sequence of ELMs during a power ramp experiment in DIII-D. From reference [11].

During the ELM-free H-mode the stored energy saturates while the density rises steadily. This points towards a much higher particle than energy confinement time [12]. In addition the impurity content of the plasma also rises in this period, as observed in various tokamaks. Thus it is necessary to lower the transport barrier periodically to release the impurity content and the helium ash. A possible method for this could be obtained by the control of the ELMs.

Since the later work will concentrate on the L-H transition and the ELMy H-mode it is necessary to develop a better understanding of the type III ELMs. A more detailed characterization of this ELM type will be given in the next section.

2.4 Type III ELMs

As shown in the last section type III ELMs are distinguished from other ELMs by the dependence of their repetition frequency on the total heating power. The repetition frequency is independent of the plasma current but experiments show that there is a connection to the electron density and to the gradients of both the temperature and the pressure [13]. The repetition frequency ranges from 2kHz down to 200 Hz for ELMy H-modes. However it is difficult to give a lower limit for the repetition frequency since it is arguable whether the frequency becomes very small or the ELMs disappear. The ELM itself is located at the closed surface of maximum electron pressure and it is bounded to a small region around this surface. In the inner part of this region, inside the surface, the ELM causes a decrease in both temperature and density while in the outer part the temperature and density are increased. Thus the radial position where the ELM perturbation changes from decrease to increase is called the radius of the ELM perturbation centre ρ_{ELM} or inversion radius.

Often type III ELMs are accompanied by coherent oscillating structures in the magnetic field, known as precursors. In the Fourier spectrum of the precursors a few dominant frequencies can be identified, ranging from 30 kHz to 150 kHz. For COMPASS-D the frequencies lie in a range of 70 kHz to 120 kHz [14]. Figures 4 and 5 show precursors of a type III ELM and the corresponding Fourier spectrum of one precursor. The precursor consists of a high frequency oscillation with a low frequency envelope. The Fourier spectrum shows two beating modes at 93 kHz and 116 kHz. Shortly before the ELM-event the precursors grow exponentially.

The frequencies of the precursors depend on the heating method (ohmic, radiative) and in the case of neutral beam injection on the direction of the neutral beams. Since the ELMs precursors show clear modes many theories consider plasma modes, like tearing or ballooning modes, as causes for the ELM. These modes become unstable during the ELM or couple with each other resulting in a huge particle loss. In most cases the precursors are detected by Mirnov coils that measure the magnetic field near their position. The oscillation of the magnetic field with poloidal and toroidal mode numbers m and n, are caused by perturbation currents flowing parallel to the field lines on rational magnetic surfaces with a q value of m/n [15]. In a toroidal coordinate system which rotates with the plasma the magnetic field can be written in the following way

$$B(t, r, \Theta, \Phi) = \sum_{mnl} B_{mnl}(t, r, \Theta, \Phi) + B_0(r, \Theta, \Phi) \tag{2}$$

$$B_{mnl}(t, r, \Theta, \Phi) = f_{mnl}(t) \cdot \varphi_{mnl}(r) \cdot cos(m\Theta + n\Phi) \tag{3}$$

Where Θ and Φ are the poloidal and toroidal angle respectively and r is the radial distance from the centre of the plasma. B_0 is an additional time-independent

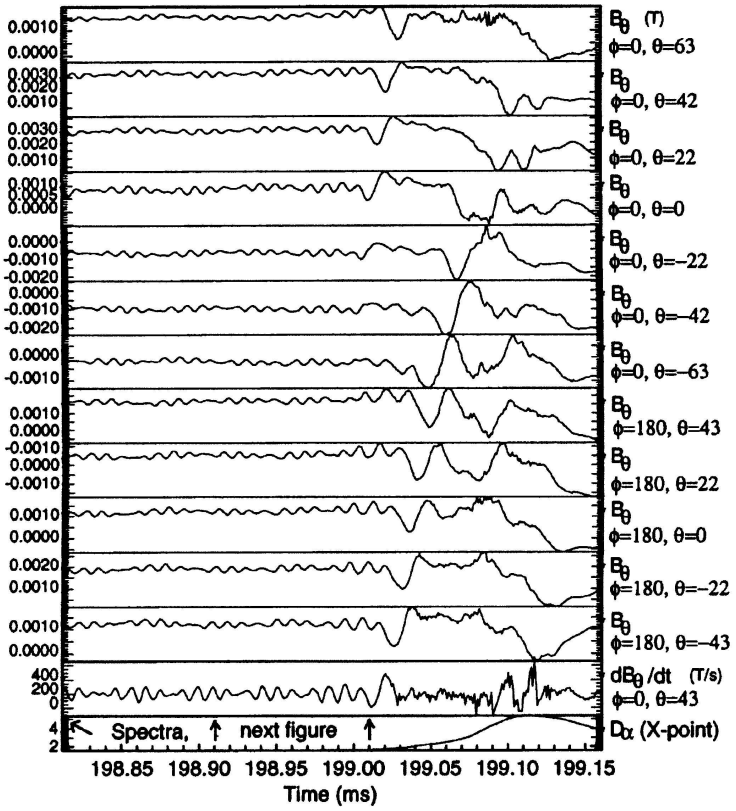

Figure 4: Precursors of a type III ELM for several toroidal and poloidal positions. From reference [14].

magnetic field that could be created by the coils around the plasma. To take the poloidal variation of the slope of the magnetic field into account a correction factor λ is introduced and Θ has to be transformed to

$$\Theta^* = \Theta - \lambda sin\Theta \tag{4}$$

This variation of the slope causes a poloidal variation of the wavelength that is larger at the outer (low field) side. The time dependence of the magnetic signal is split up into two parts. In addition to the time-dependent coefficients $f_{mnl}(t)$ the rotation of the plasma creates a second time dependence. The field perturbation is expected to be frozen within the plasma, which means that the Θ- and Φ-coordinates are time-dependent for a non-rotating frame. Since the position of the Mirnov coils is fixed in space the rotation of the plasma leads to a poloidal ω_m and a toroidal ω_n rotation frequency and modes with mode numbers m and n can be observed in measurements. The toroidal rotation is caused by two different mechanism: the electron drift and an external drive from the particle injections.

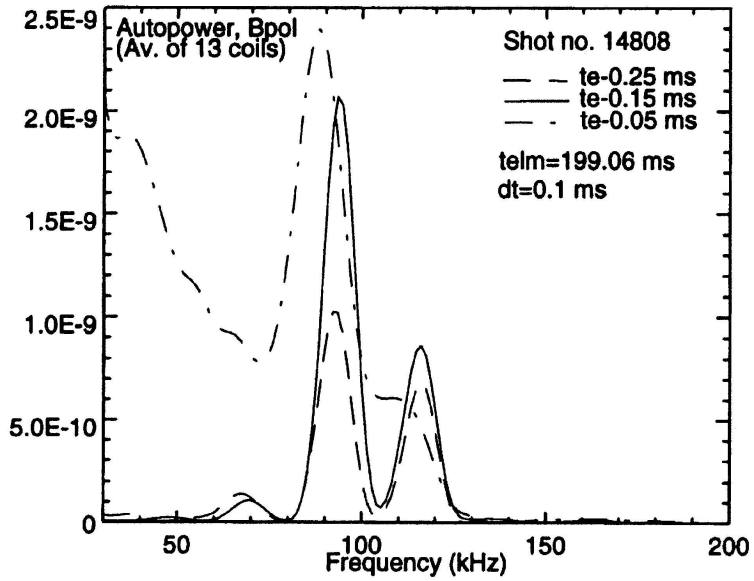

Figure 5: Fourier spectrum of the precursor. From reference [14].

Thus the toroidal rotation frequency can be written as

$$\omega_n = \omega^* \pm \omega_{dr} \tag{5}$$

where ω^* is the frequency caused by the electron drift and ω_{dr} is the frequency created by the particle injections. Note that in equation (5) ω_{dr} can increase or decrease the toroidal rotation frequency. Since the neutral beam injection drives a toroidal current the dependence of the precursor frequency on the direction of particle injection can be explained with this formula. In the case of counter-injection the toroidal rotation and the toroidal part of the electron drift velocity are in the same direction increasing the precursor frequency (+ sign) while in the case of co-injection the rotation is in the opposite direction which decreases the frequency (- sign).

Although the radial dependence of a mode with mode numbers m and n is split up into several radial functions $\varphi_{mnl}(r)$ - sometimes called radial modes - the different radial functions cannot be distinguished in the later analysis. To reflect this, new spatio-temporal coefficients of the form

$$f_{mn}(r,t) = \sum_l f_{mnl}(t) \cdot \varphi_{mnl}(r) \tag{6}$$

are introduced. The coefficient $f_{mn}(r,t)$ acts as an envelope for the corresponding m-n mode and will be called ELM-envelope in the following. This representation

of the magnetic field is used to separate the mode structure, which is caused by the rotation of the plasma and is mostly independent of the ELMs, from the dynamics caused by the ELMs, which is represented by $f_{mn}(t)$. In the following the term "high-dimensional ELM-envelope" or "high-dimensional mode" will be used to take into account that actually the ELM-envelope $f_{mn}(t)$ consists of several radial functions $\varphi_{mnl}(r)$.

Since the magnetic field is a superposition of several magnetic fields created by different modes with different frequencies, the measured signal can show a modulated shape. Figure 6b shows the effect of multiplying a given ELM-envelope of four identical ELMs with the sum of two cosines of different frequencies. In this case the difference between the ELM repetition frequency and the frequencies of the cosines causes identical ELMs to appear differently. The magnitude of the second ELM for example is only half the magnitude of the other ELMs. Although the different ELM precursors grow to their full magnitude their interaction prevents an ELM from taking place. This modulation effect could explain why in some measurements the precursors grow and vanish without causing an ELM.

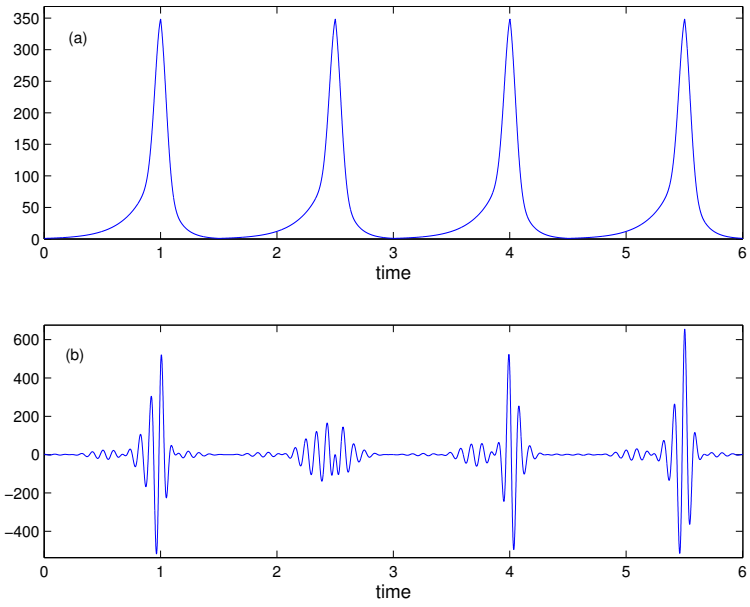

Figure 6: ELM signal and modulated ELM signal. Although the ELM-envelope (a) is identical for all ELMs, they seem to be different (b) when modulated with cosines.

Several models have been developed to explain the dynamics of the L-H transition. If the dynamics of the transition is not too complicated, information about the differential equations, which describe the system, can be obtained by a time series analysis of the measured data, which allows to test the different models.

3 Dynamical Systems and the Method of Delays

Experimental investigation of most dynamical systems is done by measuring the time dependence of some characteristic properties of the system. Since only few properties are measured it would seem that it is only possible to obtain a low-level description of the dynamics of the system. However the method of delays, which will be introduced in this section, provides an excellent method for extracting qualitative and quantitative information about the dynamics of a physical system from experimental data.

3.1 Dynamical systems, dimensions and manifolds

The basic description of dynamical systems consists of two parts. First it is necessary to specify the state of a system at a certain time, to be able to distinguish this state from other states of the system. This can be done by using a set of parameters x_1, x_2,..., x_n. The state of a ball moving in the x-y plane for example could be described by coordinates giving its position and velocity, say, x, y, v_x and v_y. Since the aim is a mathematical description of the dynamical system these parameters are elements of a linear space R^n or - more generally - of a manifold. This linear space (manifold) is called state space or phase space and the parameters are its coordinates. Here, by manifold is meant an object that can be approximated locally by a linear space (see figure 7). This linear space is called the tangent space and the dimension of a manifold is the dimension of its tangent space. Though the idea of a manifold as state space sounds strange at first it is very common in physics. An example of a system that has a non-trivial manifold as its state space is the pendulum. A state of the pendulum can be completely specified by its angle from the vertical and its angular velocity. Since the angle lies between 0 and 2π, where $0\hat{=}2\pi$ the state space is the surface of a cylinder which is a two dimensional manifold.

However the description of a state is not unique and a dynamical system can be well described by different choices of coordinates. The reason for this is that some of the coordinates are nonlinear functions of the others. In the case of the pendulum a state can also be described by the position of the pendulum in the x-z plane and the corresponding velocities. Since the distance of the pendulum from the pivot point is constant the z coordinate is a function of the x coordinate and vice versa (there is a fixed mathematical relationship between these two coordinates since $x^2 + z^2 = const$). The same statement holds for the velocities. To simplify the mathematical description of the system it is necessary to reduce the number of coordinates. Thus one of the key tasks is to find a minimum set of independent coordinates to describe a physical system. In Lagrange mechanics for example these coordinates are called generalized coordinates.

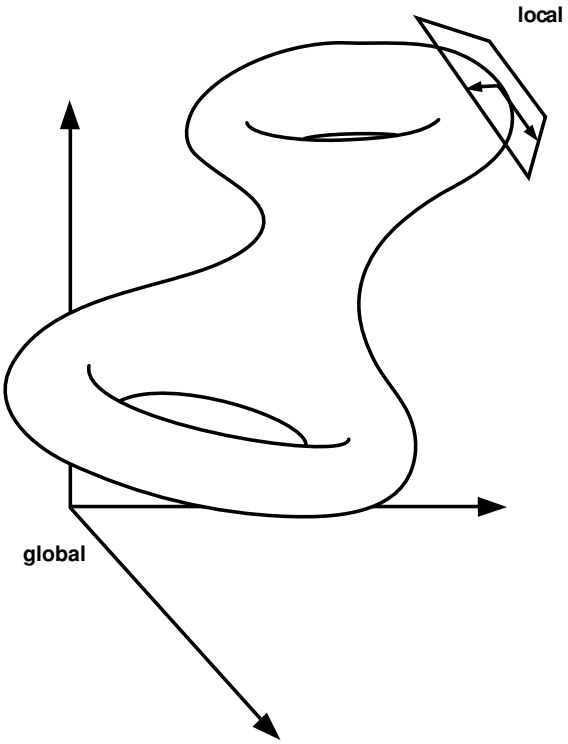

Figure 7: Example of a two dimensional manifold. At every point the manifold can be approximated locally by a two dimensional linear space, its tangent space. From reference [16].

The second part of the description of dynamical systems is to give the evolution of the systems. Thus it is necessary to find what causes the evolution and describe it by a set of equations. Most dynamical systems can be described by a limited set of ordinary differential equations of different orders for the coordinates. Each ODE of order n can simply be transformed into a system of n first order ODEs. In classical mechanics this transformation corresponds to the change from Lagrangian to Hamiltonian mechanics.

Even if the system is described by partial differential equations, as it is the case in plasma physics, a system of first order differential equations can be obtained by an expansion in a series of complete orthogonal functions. In this case the number of ordinary differential equations for the coefficients of the functions would be infinite. However by a proper choice of the orthogonal functions it may emerge that only few of them are important or most of them decay rapidly. Thus the system can be well described by neglecting most of the orthogonal functions and restricting the equations to the dominant functions. Consider for example a bar of copper of length L with an initial temperature distribution $T(x, 0)$, where x ϵ $[0, L]$. The time evolution of the temperature distribution is governed by the heat equation

$$\frac{\partial T(x,t)}{\partial t} = \kappa \frac{\partial^2 T(x,t)}{\partial x^2} \tag{7}$$

where κ is the thermal diffusivity of the bar. If we expand $T(x,t)$ in a Fourier series we get

$$T(x,t) = a_0(t) + \sum_{k=1}^{\infty} a_k(t) cos(\frac{2\pi}{L}kx) + \sum_{k=1}^{\infty} b_k(t) sin(\frac{2\pi}{L}kx) \tag{8}$$

The substitution of this expansion into the equation (8) gives an infinite set of ordinary first order differential equations for the Fourier coefficients $a_k(t)$ (similarly for $b_k(t)$)

$$\frac{da_k(t)}{dt} = -\kappa k^2 a_k(t) \qquad k \geq 0 \tag{9}$$

The state space is now the infinite-dimensional space spanned by the Fourier modes. However, except for a_0 all the $a_k(t)$ and $b_k(t)$ decay exponentially and thus if we look at the long time dynamics we can restrict our expansion to a limited number m of a_ks. Thus the state space can be reduced to R^m. In [17] for example the Karhunen-Loève expansion for reduced MHD equations, used for the description of the edge of a plasma, gives good agreement between the partial differential equations and the system of ordinary differential equations for $m \approx 20$, which is a relatively small number.

3.2 Qualitative dynamics

In many cases the differential equations for the descriptions of the system let alone the solution of them is not known. Nevertheless a great deal of qualitative information about the dynamics can be obtained by a qualitative study of the phase portrait of the system [18]. Consider a dynamical system of the form

$$\frac{dx}{dt} = F(x) \tag{10}$$

where x is a point in the phase space $S \subseteq R^n$. The vector field $F(x)$ is in general a non-linear operator acting on points in S. Under well-known conditions on $F(x)$ equation (10) defines an initial value problem in the sense that for each initial value a unique solution exists. The solution for a given initial value x_0 at a time t may be written as $x(t) = \varphi_t(x_0)$.

However, for most problems the complete solution of (10) is not known. The analysis can be simplified to some extent since many physical systems have similar basic equations which means their behaviour is also very similar. Thus it is enough to choose only one of the similar systems for the investigation and transfer the results from the analysis to the other systems. In order to be able to compare

and classify phase portraits of different systems, it is necessary to introduce an equivalence relation between differential equations.

Two C^r vector fields F and G are C^k equivalent ($k \leq r$) if there exists a C^k diffeomorphism, Φ, which maps orbits $\varphi_t(x)$ of F to orbits $\phi_t(y)$ of G in such way that their orientation is preserved. The orbits $\varphi_t(x)$ and $\phi_t(y)$ are connected via the relationship

$$\phi_t(y) = \Phi \circ \varphi_t \circ \Phi^{-1}(y) \tag{11}$$

In some way Φ is an invertible change of coordinates, which distorts the flow without changing the order in which the points of the trajectory are visited. One consequence of this equivalence is that the stability properties of fixed points are preserved. If $k = 0$ the systems are said to be topologically equivalent, because the distortion of the orbits need only be continuous. Although the stability of fixed points are the same for topologically equivalent systems the ratios of eigenvalues associated with linearization of the flow near the fixed points can be different for the individual system. This means that a distinction between say foci, where the trajectories are circling around the fixed point, and nodes, where the trajectories are not circling, cannot be obtained.

If $k = 1$ the equivalence between two systems is stronger and is called differentiable equivalence. In addition to the properties of the topological equivalence the linearized maps of F and G have the same ratios of eigenvalues at their fixed points and thus a distinction between nodes and foci can be made. Since members of the same equivalence class share common aspects of behaviour they are said to have the same qualitative dynamics.

To get a better feeling for this concept consider the following two simple differential equations for which the solutions can be calculated very easily

$$\frac{dy}{dt} = -3y \tag{12}$$

$$\text{and} \quad \frac{dx}{dt} = -x \tag{13}$$

Both equations have a very similar structure, actually the only difference is the coefficient on the right hand side. Thus one would expect that their solutions show similar behaviour. In fact the solutions

$$y(t) = y_0 e^{-3t} \tag{14}$$

$$x(t) = x_0 e^{-t} \tag{15}$$

are also very similar. Again the only difference is the exponent of the exponential function. Without knowing the solution the similarity can be shown since both systems are connected via the homeomorphism $y = \Phi(x) = x^3$

$$\frac{dy}{dt} = \frac{d}{dt}\Phi(x) = 3x^2\frac{dx}{dt} = -3x^3 = -3y \tag{16}$$

and thus are topologically equivalent. Since $\Phi^{-1}(y) = y^{1/3}$ is not differentiable at $y = 0$, $\Phi(x)$ is not a diffeomorphism. Thus the two systems are only topologically equivalent as indicated by the different coefficients of the right hand sides. Because of this equivalence it is sufficient to study only one of the two systems and deduce the properties of the other one using $\Phi(x)$.

3.3 Method of delays

The concept of topological and differentiable equivalence is a very elegant method from the theoretical point of view but has a big disadvantage for practical purposes since it gives no recipe of how to find the equivalence relation $\Phi(x)$ or an equivalent system for a given one. Especially in the context of experimental research, it is very difficult to find equivalent systems for measured data. Luckily this search can be simplified by creating an equivalent system from the given data. A way of creating a system with equivalent dynamics as the physical system of interest is given by Takens' theorem:

Let M be a compact manifold of dimension m. For pairs (F, v), F a smooth (i.e. C^2) vector field and v a smooth function on M, it is a generic property that $\Phi_{F,v}(x) : M \to R^n$ defined by

$$\Phi_{F,v}(x) = (v(x), v(\varphi_\tau(x)), ..., v(\varphi_{(n-1)\tau}(x)))^T$$

is an embedding, provided that $n \geq 2m + 1$. Here φ_t is the solution of equation (10) and $\tau > 0$.

An embedding is a smooth map, say Φ, from the manifold M to a space U such that $\Phi(M)$ is a smooth submanifold of U and Φ is a diffeomorphism between M and $\Phi(M)$. Since $v(x)$ corresponds to the value of a measurement made on the system it is called the measurement function. The space which contains the image of Φ is called the embedding space and its dimension the embedding dimension. As Φ is a diffeomorphism between two manifolds one prerequisite for a differentiable equivalence relation is fulfilled. Thus the dynamics of the physical system can be investigated by analyzing the dynamics in the embedding space R^n.

The practical implementation of this theorem is the method of delays. Let $\{v_i\}$, $i = 1, 2, ..., N_m$ be a time series of measurements made on the system, where

$v_i = v(\varphi_{i\tau}(x))$ and τ is the sampling time. Since the sampling time τ for the flow $\varphi_\tau(x)$ is unspecified in the theorem there is theoretically no condition on the choice of τ of the measurement as long as τ does not change during the measurement. A schematic representation of this method is given in figure 8.

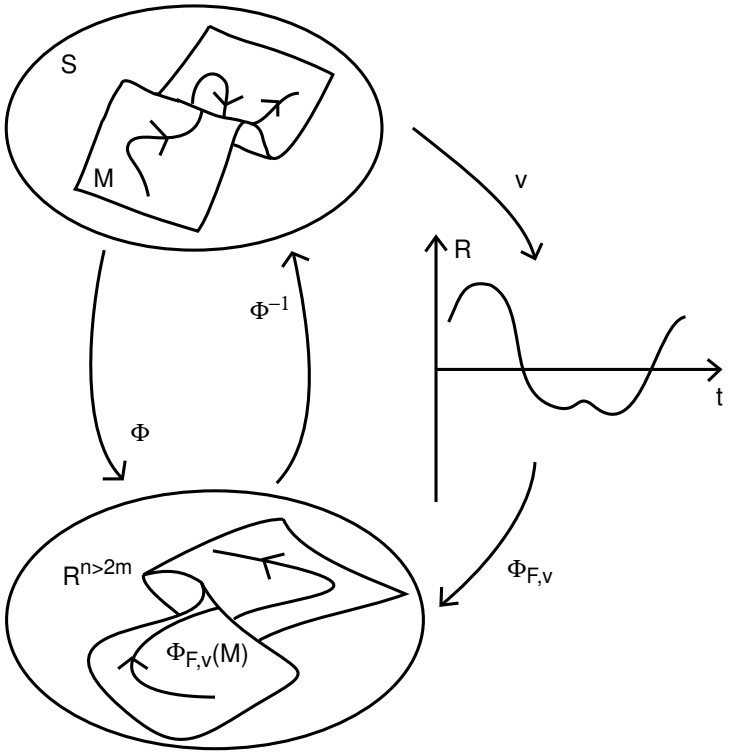

Figure 8: Schematic representation of the method of delays. From reference [18].

A useful concept is an (n, J)-window which makes visible n elements of the time series with the sub-sampling time $J \cdot \tau$. As the window is advanced step-wise through the time series a sequence of vectors is generated which form a discrete trajectory in the embedding space. These vectors are called delay vectors and are of the following form

$$x_i = (v_i, v_{i+J}, ..., v_{i+(n-1)J})^T$$

Though this method is an elegant way to reconstruct the dynamics of the system there are several difficulties in applying this method to measurements made on the system. Most of these problems arise from the fact that Takens' theorem considers the problem from the theoretical point of view and is not concerned about the actual process of measurement. One of the most obvious problems comes from the unspecified time scales. In the concept of the (n, J)-window

there exist three time scales, the sampling time τ_s, the lag time $\tau_L = J \cdot \tau_s$, and the window length $\tau_w = n \cdot \tau_L$. On the one hand a small sampling time is desirable to get a good and smooth approximation of the dynamics. On the other hand if the sampling time is too small the samples are highly correlated and only a one dimensional reconstruction of the system can be achieved in practice. To avoid this problem the lag time introduces a degree of statistical independence between the samples.

Another problem arises from the unknown dimension m of the phase space or to be more precise from the unknown dimension n of the embedding space. If n is to small then the dynamics will be projected onto a lower-dimensional space and the trajectories intersect in the delay space. Takens' theorem imposes the condition that n has to be greater than $2 \cdot m$ but in practice sometimes a smaller embedding dimension is enough or for noisy systems a much bigger number than $2 \cdot m$ is needed. The simple approach to increase n until the trajectories no longer intersect is a rather subjective criterion which becomes unworkable in higher dimensions and the presence of noise. Several techniques for estimating the dimensions of the manifold and the embedding space have been published [19, 20], however most of them fail for noisy data and have limitations [21]. A method for coping with most of the mentioned problems is given by the singular value decomposition which will be described in the following section.

3.4 Singular value decomposition

Consider the case of a series of N_m-measurements made on the system. After applying an $(n, 1)$-window, or an n-window as it is often called, we get a new series of $N = N_m - (n-1)$ delay vectors $\{x_i\}$ in the embedding space. The sequence can be used to create the trajectory matrix X, which is defined by:

$$X = \frac{1}{\sqrt{N}} \begin{pmatrix} y_1^T \\ y_2^T \\ \cdot \\ \cdot \\ \cdot \\ y_N^T \end{pmatrix} = \frac{1}{\sqrt{N}} \begin{pmatrix} v_1 & v_2 & \dots & v_n \\ v_2 & v_3 & \dots & v_{n+1} \\ \cdot & \cdot & \cdot & \cdot \\ \cdot & \cdot & \cdot & \cdot \\ \cdot & \cdot & \cdot & \cdot \\ v_{N_m-n+1} & v_{N_m-n+2} & \dots & v_{N_m} \end{pmatrix} \tag{17}$$

where $\sqrt{N}$ is used as a normalization. Information about the dynamics of the physical system can be obtained from the trajectory matrix by performing a singular value decomposition (SVD). The global singular value decomposition of a real N by n matrix X where $N > n$ is the expansion of X in terms of matrices S, Σ and C such that:

$$X = S\Sigma C^T$$

where S is an N by n matrix with orthonormal columns, C is an n by n orthogonal matrix, and $\Sigma = diag(\sigma_1, ..., \sigma_n)$ is n by n. The columns c_i of C are eigenvectors of the covariance matrix $\Theta = X^T X$ and the σ_i^2 are the corresponding eigenvalues. Thus the c_i are called singular vectors and the σ_i are called singular values and can be chosen to be non-negative. The set of singular values is often referred to as the singular value spectrum. In addition the σ_i^2 are eigenvalues of the structure matrix $\Xi = XX^T$ where the corresponding eigenvectors are the columns of the matrix S. Since both Ξ and Θ are real and symmetric their eigenvectors form a complete orthonormal basis for R^n and R^N respectively.

Without loss of generality let's assume that the singular values are ordered so that $\sigma_1 \geq \sigma_2 \geq ...\sigma_n \geq 0$. In some cases the rank of Ξ and Θ will be less than n. Thus by projecting the delay vectors onto the singular vectors the embedding space can be separated into two subspaces R^d and R^{n-d}, where $d = rank(\Theta)$. The subspace R^d contains the embedded manifold which means that d is an upper limit for the dimension of the manifold and a dimensionality reduction is obtained. In fact the global singular value decomposition gives an estimate for the minimum dimension that is needed to embed the physical system. This dimension is not necessarily the same as the dimension of the phase space. Take for example a simple torus as phase space whose dimension is two. However to embed the torus at least a three dimensional space is needed.

The projection onto the delay vectors corresponds to a basis transformation in the embedding space. In the singular vector basis the coordinates of the delay vectors are linearly independent. The projection of the trajectory matrix onto this basis results in a new trajectory matrix P

$$P = X \cdot C = S\Sigma = \begin{pmatrix} P_{1,1} & P_{1,2} & ... & P_{1,n} \\ P_{2,1} & P_{2,2} & ... & P_{2,n} \\ . & . & . & . \\ . & . & . & . \\ . & . & . & . \\ P_{N,1} & P_{N,2} & ... & P_{N,n} \end{pmatrix} \tag{18}$$

whose columns are the linearly independent. The columns of P are called principal components and represent the time evolution of the coordinates of the delay vectors in the singular vector basis.

However there are two limitations on this method. One problem arises from the non-linear parts of equation (10). It can be shown that singular values can be zero if and only if the time series can be expressed as an nth order linear difference equation [25]. Thus in non-linear systems no singular value will be zero. The same problem occurs, if the measurement function v is non-linear. The second problem is caused by noise. Since in most cases noise is included in the time series the number of non-zero singular values is increased.

Consider a noisy time series with additive zero mean white noise. The observed time series has the form:

$$v_j = \bar{v}_j + n_j$$

where $\bar{v}_j$ is the noise-free deterministic component, and n_j is a white noise with zero mean and variance σ_n^2. Since n_j and $\bar{v}_j$ are uncorrelated the covariance matrix is of the form

$$\Theta_{ij} = \bar{\Theta}_{ij} + \sigma_n^2 \delta_{ij} \tag{19}$$

where $\bar{\Theta}$ is the noise-free covariance matrix. From equation (19) it can be seen, that for $1 \leq i \leq n$ the σ_i^2's are of the form

$$\sigma_i^2 = \bar{\sigma}_i^2 + \sigma_n^2 \tag{20}$$

According to equation (20) the squares of all singular values are shifted by the variance of the noise. Nevertheless a reduction of dimensionality and a linearization of the time series can be done by projecting the trajectory matrix on the singular vectors, whose singular values lie above the noise floor σ_n^2.

A better estimation of the dynamics near one point on the trajectory in the embedding space say $y = y_{k_0}$, can be achieved by doing a local singular value decomposition which means that the trajectory matrix is restricted to delay vectors that lie in a neighborhood of radius ε around y. The basic idea behind this method is that the dynamics of the delay vectors should locally be confined to the tangent space of the manifold. Thus a local singular value decomposition should give the dimension of the manifold. Let's consider a ball $B_\varepsilon(y)$ of radius $\epsilon > 0$ centred at y.

$$B_\epsilon(y) = \{y_k : |y_k - y| < \varepsilon\}$$

Let N_ε be the number of points in $B_\varepsilon(y)$. Then we can write $B_\varepsilon(y) = \{y'_1, y'_2, ..., y'_{N_\varepsilon}\}$ and create a new trajectory matrix X_ε.

$$X_\varepsilon = \frac{1}{\sqrt{N_\varepsilon}} \begin{pmatrix} (y'_1 - y)^T \\ (y'_2 - y)^T \\ . \\ . \\ . \\ (y'_{N_\varepsilon} - y)^T \end{pmatrix} \tag{21}$$

However the notion of locally is problem dependent and it is very difficult to give limits for a local neighborhood. To address this problem the radius ε of B_ε is

increased and for every radius a singular value decomposition of B_ε is performed. The scaling of the singular values $\sigma_i(\varepsilon)$ with respect to ε gives information about the dimensionality of $\Phi(M)$ [16]. The non-zero singular values that correspond to the dynamics of the system scale linearly with ε. The other non-zero singular values represent the curvature of $\Phi(M)$ in the delay space and thus will scale as ε^α for $\alpha > 1$. However this scaling behaviour is only true for small ε since curvature effects become dominant and will cause all non-zero singular values to scale non-linearly. Thus by performing the local singular value decomposition an estimation $\hat{m}$ of the number of degrees of freedom is obtainable which is smaller than the actual number, i.e. $\hat{m} \leq m$.

In noisy systems the scaling changes slightly. Consider again a time series of the form

$$v_j = \bar{v}_j + n_j$$

with zero mean white noise n_j uncorrelated with $\bar{v}_j$. As mentioned above the singular values for a given ball radius ε can be written as

$$\sigma_i^2(\varepsilon) = \bar{\sigma}_i^2(\varepsilon) + \sigma_n^2(\varepsilon) \tag{22}$$

To see the influence of noise on the scaling of the singular values a closer look at the scaling of the noise is necessary. Define the noisy part η_i of the ith delay vector and the diameter of noise D_n as below

$$\eta_i = (n_i, n_{i+1}, ..., n_{i+n-1})^T \tag{23}$$

$$D_n = \max_{1 \leq j \leq N} (\|\eta_j\|) \tag{24}$$

If ε is smaller than D_n the noise will extend in all directions an so $\sigma_n(\varepsilon)$ will scale linearly. As ε becomes bigger than D_n, $\sigma_n(\varepsilon)$ saturates and reaches a constant value. If $\bar{\sigma}_i(\varepsilon)$ is large compared to $\sigma_n(\varepsilon)$ the scaling of $\sigma_i(\varepsilon)$ is dominated by the scaling of $\bar{\sigma}_i(\varepsilon)$ and thus will show the same results as if no noise were present. However if $\bar{\sigma}_i(\varepsilon)$ is small compared to $\sigma_n(\varepsilon)$ the scaling is dominated by $\sigma_n(\varepsilon)$ and will be linear for small ε but constant for $\varepsilon > D_n$. Thus surprisingly high values for $\hat{m}$ can be caused by noise.

The local singular value decomposition provides a good method for estimating the dimensionality of the system. By setting all singular values which correspond to non-linearities and noise to zero a linearization and cleaning of the time series data is possible. After applying the local singular value decomposition the local linear structure of the dynamical system can be obtained, as shown in the next section.

3.5 The local linear model

Since the delay embedding creates a differentiable equivalence between the original system and the reconstruction in the embedding space, the local dynamics at fixed points are preserved. Thus if $\bar{x}$ is a fixed point of the system and $x = \bar{x} + \delta x$, where δx is small, equation (10) can be approximated by

$$\delta \dot{x} = DF_x(\bar{x})\delta x \tag{25}$$

where $DF_x(\bar{x})$ is the Jacobian of the vector field F evaluated at the fixed point $\bar{x}$. The flow at the associated fixed point $\bar{y} = \Phi(\bar{x})$ can be approximated in the same way by

$$\delta \dot{y} = DG_y(\bar{y})\delta y \tag{26}$$

where $y = \bar{y} + \delta y$ and δy is small. $DG_y(\bar{y})$ is the Jacobian of the induced vector field. As there is a differential equivalence between the two systems (caused by the diffeomorphism $\Phi(x) = \Phi_{F,v}(x)$) the linear approximations (25) and (26) are connected by

$$DG_y(\bar{y}) = D\Phi_x(\bar{x}) \cdot DF_x(\bar{x}) \cdot D\Phi_y^{-1}(\bar{y}) \tag{27}$$

Since (27) is a similarity transform $DG_y(\bar{y})$ and $DF_x(\bar{x})$ have the same eigenvalue spectrum and thus the dynamics near a fixed point of the original system can be obtained by analysis of the point in the embedding space.

Since $DG_y(\bar{y})$ is time-independent the solution of equation (26) is

$$\delta y(t) = e^{DG_y(\bar{y})t}\delta y(0) \tag{28}$$

The eigenvalues μ_k of $\Psi_t = e^{DG_y(\bar{y})t}$ are related to the eigenvalues λ_k of $DG_y(\bar{y})$ through

$$\lambda_k = \frac{1}{\tau} \cdot ln(\mu_k) \qquad , \quad 1 \leq k \leq d \tag{29}$$

where τ is the sampling time of the time series.

The flow $\Psi_t = e^{DG_y(\bar{y})t}$ can be obtained from the dynamics of the trajectory matrix, since

$$X_\varepsilon(t+\tau)^T = \Psi_\tau X_\varepsilon(t)^T = e^{DG_y(\bar{y})\tau} X_\varepsilon(t)^T \tag{30}$$

As equation (30) is an overdetermined system of linear equations it can be solved by a least squares solution.

3.6 The Rossler system

To illustrate the power of the methods of delays and the singular value decomposition both methods will now be applied to the Rossler system. The Rossler system is a 3-dimensional dynamical system described by the following equation:

$$\begin{aligned} \dot{x} &= -y - z \\ \dot{y} &= x + ay \\ \dot{z} &= bx - cz + xz \end{aligned} \tag{31}$$

where a, b and c are non-zero constants. The solution Ψ_t of (31) is unknown but can be approximated numerically. For this example $a = 0.36$, $b = 0.3$ and $c = 4.2$ and the delay $\tau = 0.05$ have been chosen and for several initial points $N = 20000$ points of the trajectory have been calculated. For the numerical solution of (31) and for the following analysis several algorithms have been written in MATLAB (a mathematical and graphical package) using its in-built mathematical routines. The time series was created by measuring the x-component of each point of the trajectory. As expected the results obtained from the following analysis of the trajectories are independent of the initial point. Thus only the results for the initial point $x_0 = (0.9501, 0.2311, 0.6068)$ are shown. The first 5000 elements of the time series are shown in figure 9.

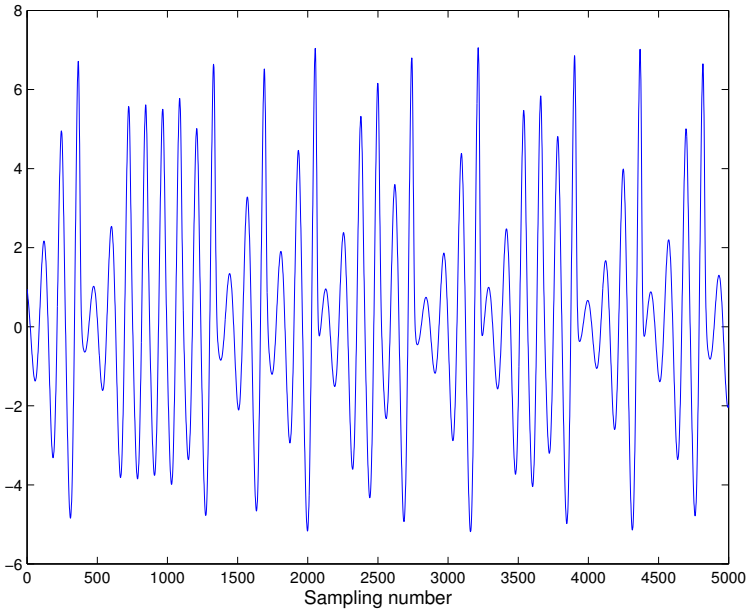

Figure 9: First 5000 points of x-component of the trajectory of the Rossler system.

The trajectory of the Rossler system is shown in figure 10. Although the Rossler

system is a 3-dimensional system the phase-portrait is - except for the origin - locally 2-dimensional. This local 2-dimensional behaviour poses a big problem for the estimation of the dimension of the phase space with the local singular value decomposition.

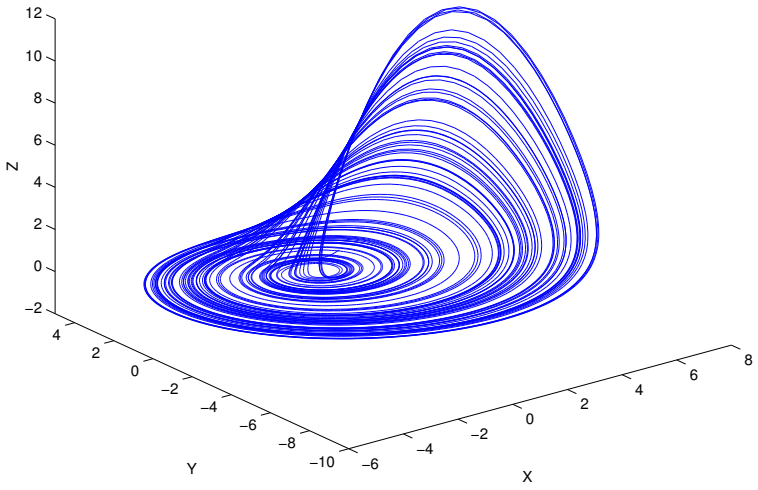

Figure 10: Trajectory of the Rossler system. Shown are the x-, y- and z-coordinate of the trajectory.

The singular value spectrum and the scaling of the singular values are given in figures 11 and 12. The trajectory matrix was constructed by using an embedding dimension of $n = 7$ and a delay of $\tau = 0.05$. The singular value spectrum shows three singular values that lie above the noise floor. In this case the noise is generated by the numerical solution of the ODE and by the numerical calculation of the singular value decomposition. Thus the global singular value decomposition gives $m = 3$ as an estimation for the degrees of freedom of the Rossler system. As mentioned above the local singular value decomposition has to be done carefully. The point y a which the ball $B_\epsilon(y)$ is centered, cannot be chosen arbitrarily but has to lie close to the origin where the trajectory passes through all three dimensions. In figure 12 the point $y = (-0.0049, -0.0016, 0.0)$ was chosen for the analysis. The first three singular values scale linearly while most other singular values scale as ε^2 in the beginning but reach a constant value very fast. Another interesting property is the step-wise scaling of the singular values greater than 4. This step-wise behaviour of the scaling reflects the fact, that the trajectory of the Rossler system has a band structure (see figure 10). Every time the ball radius becomes big enough to include the next band the singular values suddenly increase, since the number of points in the ball increases in the same way.

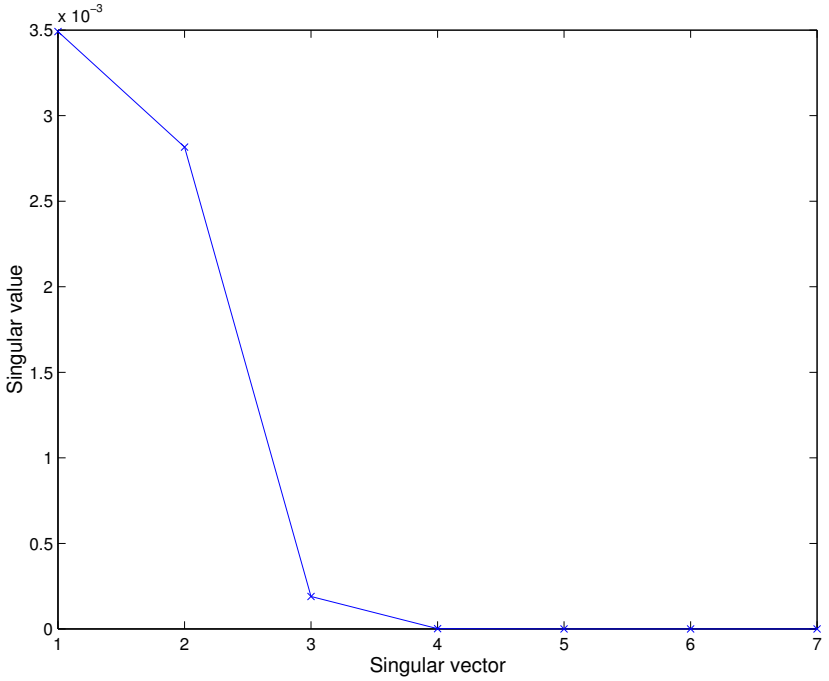

Figure 11: Global singular value decomposition. Only three singular values are bigger than zero, giving an dimension of $m = 3$.

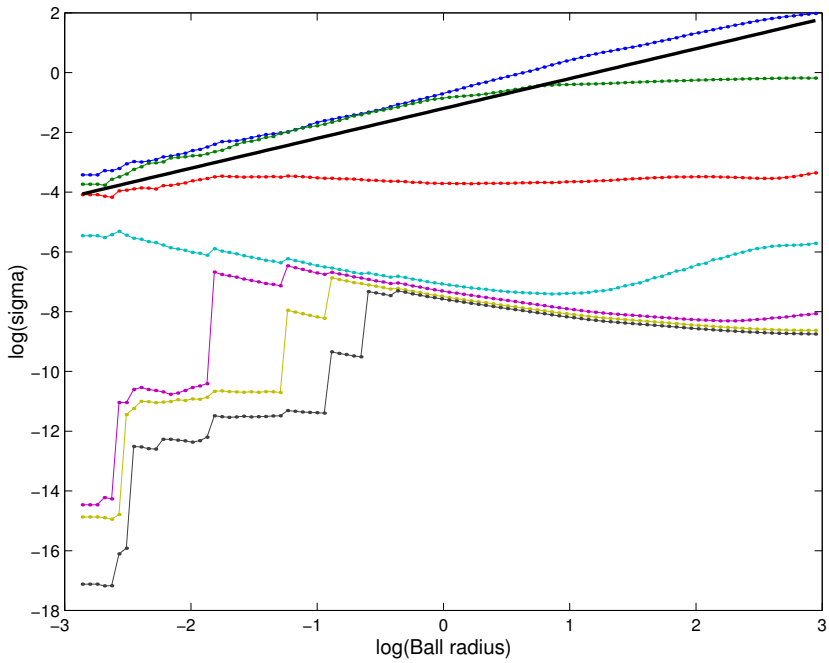

Figure 12: Local singular value decomposition. For comparison a line with slope 1 is drawn. Only the first three singular values scale linearly giving $m = 3$.

The local and global singular value decomposition give $m = 3$, which is the correct dimension of the Rossler system. Thus if we project the trajectory matrix onto the first three singular vectors the dynamics of the system should be recovered. Figures 10 and 13 show the trajectories of the Rossler system and of the projection of the delay vectors onto the first three singular vectors respectively. The comparison of both figures shows clearly that the dynamics of the Rossler system is qualitatively recovered by the combination of delay embedding and singular value decomposition.

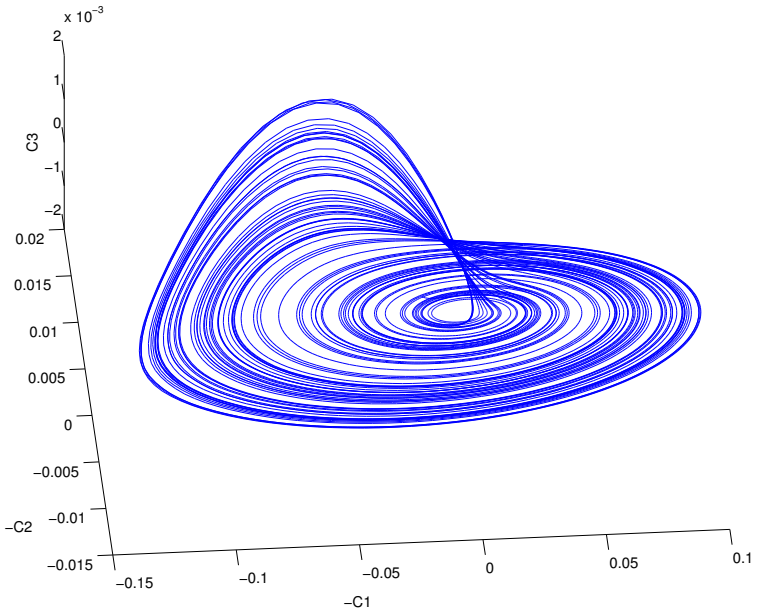

Figure 13: Projection of the singular vectors onto the first three singular vectors.

So far the comparison between the original Rossler system and the system in the delay space was except for the estimation of m purely qualitative. However, the estimation of the local linear model allows us to compare these two systems in a quantitative way. In order to compare the results of the following local analysis of the system in the delay space with the Rossler system, the Jacobians of both systems have to be calculated. The Jacobian of the Rossler system at the fixed point $x_0 = (0, 0, 0)^T$ is in this case:

$$DF_x(x_0) = \begin{pmatrix} 0 & -1 & -1 \\ 1 & 0.36 & 0 \\ 0.3 & 0 & -4.2 \end{pmatrix} \tag{32}$$

The eigenvalues of the Jacobian are given by

$$\begin{aligned} \lambda_1 &= 0.145547 + 0.984557i \\ \lambda_2 &= 0.145547 - 0.984557i \\ \lambda_3 &= -4.131094 \end{aligned} \tag{33}$$

To estimate the local linear model we create a new trajectory matrix $\hat{X}$ by projecting the trajectory matrix X onto the first three singular vectors:

$$\hat{X} = X \cdot (C_1, C_2, C_3) = \begin{pmatrix} P_{1,1} & P_{1,2} & P_{1,3} \\ P_{2,1} & P_{2,2} & P_{2,3} \\ \dots & & \\ P_{N,1} & P_{N,2} & P_{N,3} \end{pmatrix} \tag{34}$$

To get a linear equation for the linearized flow Ψ_τ we use two additional matrices Y and $\hat{Y}$ that consist of the first $N-1$ or the last $N-1$ rows of $\hat{X}$ respectively. Because of the structure of $\hat{X}$ each row $\hat{Y}_j$ of $\hat{Y}$ is connected to the corresponding row Y_j of Y via

$$\hat{Y}_j^T = (P_{j+1,1}, P_{j+1,2}, P_{j+1,3})^T = \Psi_\tau \cdot (P_{j,1}, P_{j,2}, P_{j,3})^T = \Psi_\tau Y_j^T \tag{35}$$

This means that by using only delay vectors, whose distance from the fixed point is small, the local linear model of the Rossler system can be estimated solving the linear equation

$$\hat{Y}_\varepsilon^T = \Psi_\tau Y_\varepsilon^T \tag{36}$$

Here the index ε denotes that the matrices $\hat{Y}_\varepsilon$ and Y_ε^T only contain the rows of $\hat{Y}$ and Y whose distance from the fixed point is less than ε. Since equation (36) is an overdetermined linear equation it can be solved by a least squares method. The solution Ψ_τ is of the form

$$\Psi_\tau = e^{DF_x(x_0)\tau} \tag{37}$$

Thus the eigenvalues of $DF_x(x_0)$ are

$$\lambda_i = \frac{1}{\tau} \cdot ln(\mu_i) \tag{38}$$

where μ_i are the eigenvalues of Ψ_τ. Since the linear approximation for Ψ is only valid for small ε but the notion of small is not unambiguous the linear model has been calculated for several radii ε. The dependence of real and the imaginary parts of the estimated linear model on the radius is shown in figures 14.

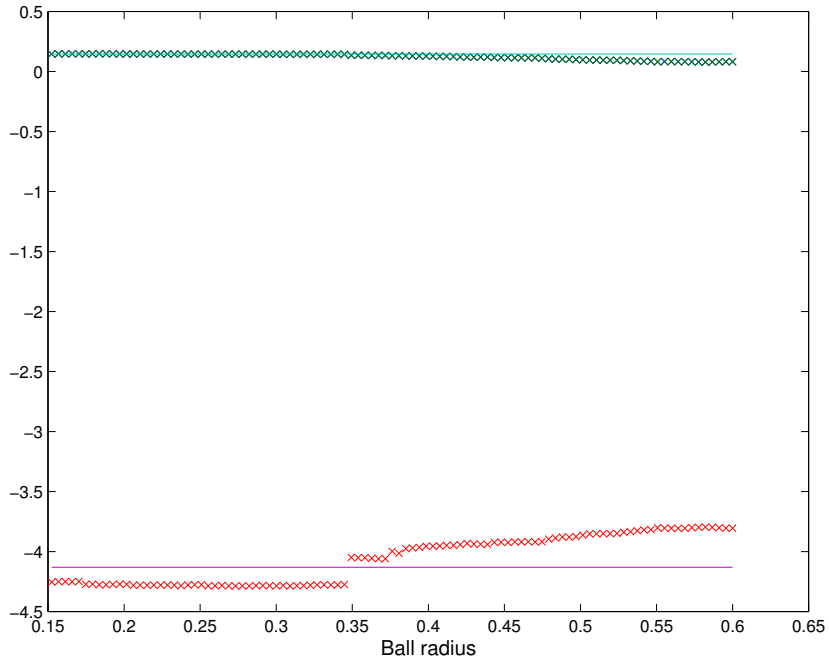

Figure 14: Scaling of the real parts of the eigenvalues. For radii smaller than 0.35 the values are quite constant.

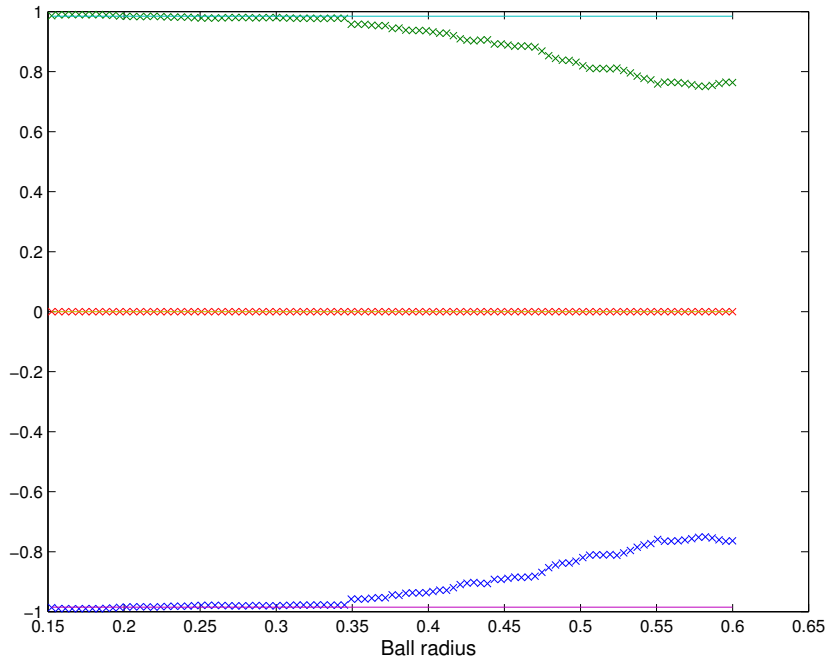

Figure 15: Scaling of the imaginary parts of the eigenvalues. Again the values are quite constant for radii smaller than 0.35.

The calculated eigenvalues are quite constant as long the radius is smaller than 0.35. Thus for the estimation of the eigenvalues of the local linear model the mean values of the calculated eigenvalues up to the radius of 0.35 have been taken and are listed in table 1 together with their relative error.

Eigenvalue	Relative error real part	Relative error imaginary parts
0.1452 $\pm$ 0.9819 i	0.002	0.003
-4.2727	0.034	-

Table 1: Estimated eigenvalues of the Rossler system and their relative error

Table 1 shows that the eigenvalues are accurate to within 3% of their analytic value. Thus the local linear model can be recovered quite accurate by the combination of the delay embedding and the singular value decomposition. This example shows how powerful this method is since although only one coordinate of the Rossler system has been used, the eigenvalues can be calculated in a very accurate way.

4 Description of COMPASS-D and the Discharge

Many theories have been developed to describe ELMs and the L- to H-mode transition. In early experiments the L- to H-mode transition was achieved by use of neutral beam power for additional heating. In these experiments the L-H transition was sharp occurring in less than a few milliseconds after the heating was increased very fast. For the study of ELMs and the transition dynamics this method has two disadvantages. Since the additional heating is applied very quickly, the plasma properties change in the same rapid manner. Thus changes in the plasma properties can be seen that are not caused by ELMs or the transition itself. A second problem arises due to the increase of the electron density caused by refuelling of the plasma by the beams. In particular the continuous refuelling makes a comparison between the forward L-H transition and the backward H-L transition very difficult. These problems can be avoided by heating the plasma gradually by applying ohmic or radio frequency heating. By using this method a slow transition can be produced in COMPASS-D which will be described in the following section.

4.1 COMPASS-D

COMPASS-D is a medium sized tokamak that has been designed to investigate key physical issues associated with magnetic confined fusion. Since its cross-section and magnetic configuration (fig. 16) are similar to Jet and to those proposed for ITER, COMPASS-D plays an important role for size scaling studies. A list of characteristic COMPASS-D parameters is shown in table 2

Major plasma radius	0.557 m
Minor plasma radius	0.232/0.385 m
Magnetic field	2.1 T
Plasma current	< 400 kA

Table 2: Characteristic COMPASS-D parameters

COMPASS-D uses a single null divertor configuration with a relevant high triangularity plasma shape and routinely operates in ELMy H-mode. COMPASS-D is equipped with three poloidal arrays each of 24 Mirnov coils inside the D-shaped vacuum vessel located at different toroidal positions. The coils are close to the plasma and can sample up to 1 MHz for a limited period of time during the discharge. Thus the spatio-temporal structure of magnetic field perturbations can be detected and investigated. For additional heating COMPASS-D is equipped with eleven ECRH antennas, five high field side (HFS) and six low field side

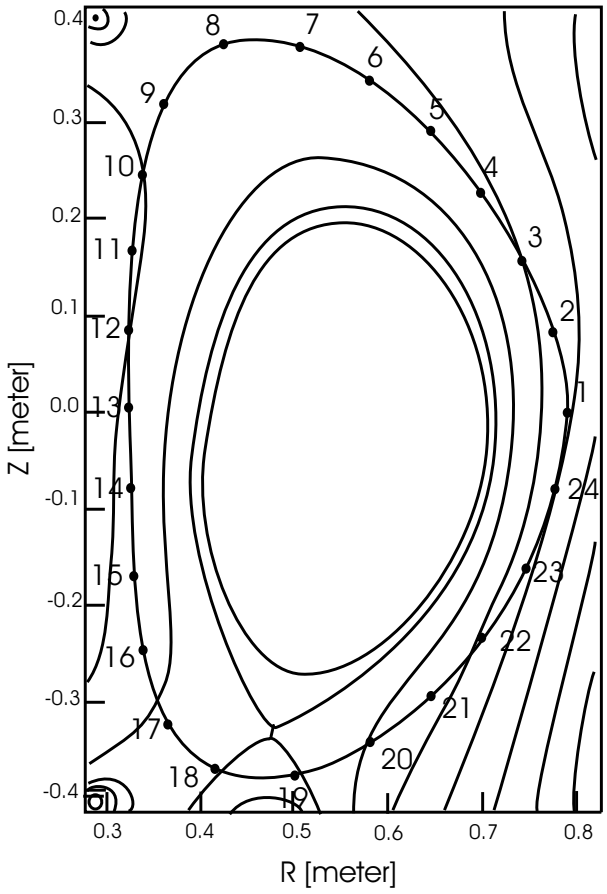

Figure 16: Poloidal cross section of Compass-D. The position of the 24 Mirnov coils is indicated with the numbers 1 - 24. From reference [27].

(LFS). Up to nine gyrotrons can be connected in O or X mode polarization, with achieved total power into the torus exceeding 1.4 MW.

4.2 The discharge

In order to study the dynamics of the L-H transition on COMPASS-D a slow transition between these modes was performed by gradually ramping up the ECRH-heating for discharge # 24815. Figure 17 shows some of the measurements of the discharge. The changes of the plasma parameter have been done on a long time scale compared with the energy confinement time and thus the plasma is in a quasi steady state close to transport equilibrium. During the discharge the plasma moves from L-mode to ELMy H-mode and back to L-mode. Between the second (0.12 seconds) and third heating step (0.145 sec.) the plasma moves from L- to H-mode. Because the transition happens gradually the determination of the transition point cannot be done exactly. After the fourth heating step the plasma reaches a quasi steady state. At the end of the discharge the heating power is reduced stepwise, causing a transition back into L-mode around 0.24 seconds.

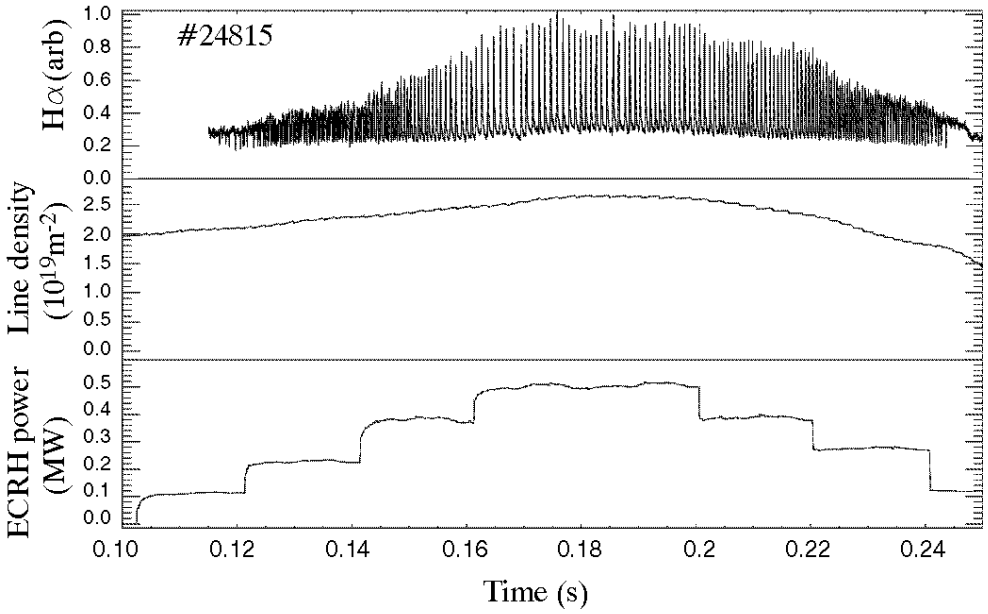

Figure 17: Transition to ELMy H-mode in Compass-D.(a) shows the H_α signal, (b) the line averaged electron density and (c) the ECRH power.

During the discharge ELMs occur as can be seen in the H_α signal in figure 17 (a). The ELMs start during the transition from L- to H-mode and thus no ELM-free period right after the transition can be seen. The repetition frequency of the ELMs decreases with increasing heating power so they can be identified as type III ELMs. During the discharge the ELM-free phase is not reached and thus density control is maintained and the plasma moves back to L-mode in a reversible manner at the end of the discharge. The two transitions between the two confinement modes are not symmetric in time. The electron density decreases faster at the transition back to L-mode than it was increasing at the forward transition. The same can be seen in the H_α signal which also decreases much faster than it increased.

5 Analysis of the measured Data

To obtain a good time and spatial resolution of the plasma dynamics during the L-H transition Mirnov coils # 5, 4, 2, 1, 24, 23, 22 and 21 have been used to measure the time derivative of the poloidal component of the magnetic field with a sampling frequency of 200 kHz (in the following the coils are labelled with 1, 2, ..., 8 corresponding to the order given above). The Mirnov coils measure the magnetic signal near their position outside the plasma. However this signal is the superposition of several magnetic fields generated by different kinds of dynamics. In addition the magnetic signals come from various locations of the plasma which complicates the investigation of the dynamics. Fig. 18 shows different plots of the data obtained from coil # 5 (compare fig. 16) on different time scales.

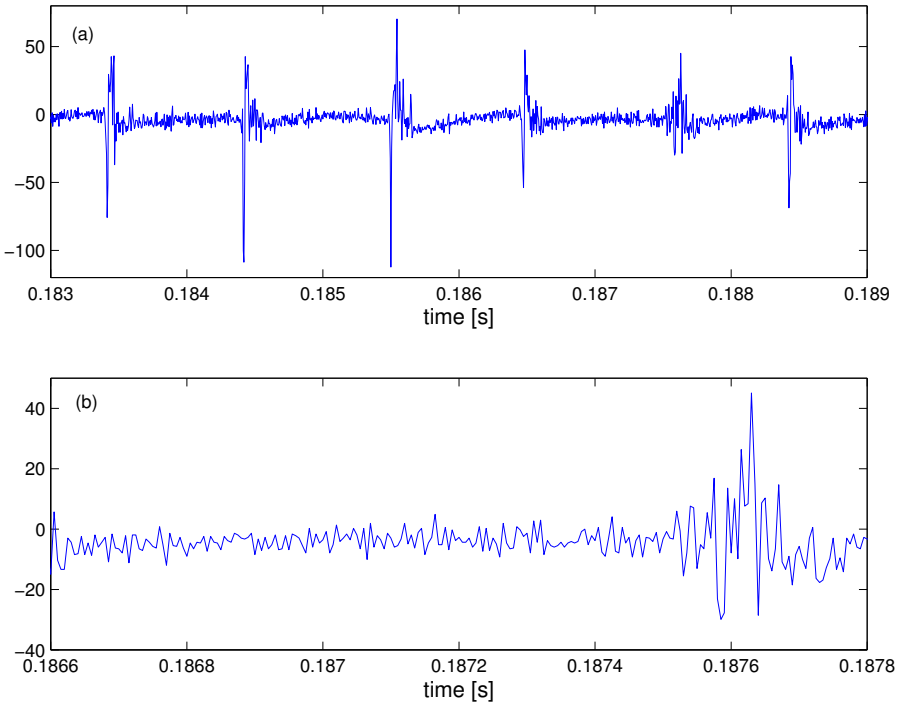

Figure 18: Two plots of the data obtained by coil # 5. (a) In addition to the pulse-like oscillation caused by the ELM precursors a second sawtooth like wave can be identified . (b) The precursors consist of a high frequency oscillation with a low frequency envelope.

At least two different kinds of dynamics can be identified in figure 18a. In addition to a pulse-like oscillation due to the ELM a second signal, a sawtooth wave - characterized by an approximatively linear increase in the local mean of the signal between ELMs and a rapid decrease in mean during an ELM - can be observed. This sawtooth oscillation is caused by the response of the bulk plasma

to an ELM. During an ELM the plasma loses particles and energy and thus the plasma pressure decreases. On the other hand an external force, that points horizontally towards the transformator coils keeps its equilibrium value and is now greater than the plasma pressure. This causes the bulk plasma to change its position and move towards the transformator coils. Between ELMs the plasma temperature increases and with it the plasma pressure causing the bulk plasma to move back to its original position. In addition to this intrinsic movement an externally applied magnetic feedback system tries to keep the plasma in position by adjusting the external magnetic field. These changes, intrinsic and external, are picked up by the Mirnov coils and thus the signal obtained by the measurement is a superposition of the changes of the magnetic field caused by the dynamics of the bulk plasma, the feedback system, and the ELMs.

Prior to the ELM clear coherent precursor oscillations can be seen (fig 18b) which start 1 ms before the ELM itself and grow rapidly. The precursor consist of a high frequency oscillation with a low frequency envelope. This behaviour might be caused by the modulation of the ELM-envelope with at least two plasma modes that cause the ELM signal to oscillate with the frequency of the modes, as mentioned in section 2. A look at the corresponding Fourier spectrum (fig. 19a) gives only hints for frequencies which correspond to the modes. The Fourier spectrum was calculated with the Fast Fourier Transform built into MATLAB. Since only 150 measurement points have been made for one ELM-cycle the Fourier spectrum is not very accurate. Even if we take several ELM-cycles (900 measurement points) the Fourier spectrum (fig. 19b) is broad-band and it is hard to identify any frequencies associated with the modes.

As the precursor frequencies lie between 60 and 120 kHz the sampling frequency of 200 kHz causes a big problem since the corresponding Nyquist frequency is 100 kHz. Thus all frequencies greater than 100 kHz will be aliased and appear below 100 kHz in the Fourier spectrum. In particular modes near the Nyquist limit are sparsely sampled and their investigation is difficult since the estimation of amplitude/power of a mode sampled at or near the Nyquist limit is not accurate. In addition since there are only a few measurements per cycle that makes it difficult to distinguish signal from noise. Because of the problems mentioned above a straight forward analysis of the data using delay embedding is not practicable. Thus it is necessary to identify the different kinds of dynamics to obtain a global picture and improve the understanding of the plasma for further investigations.

5.1 The global picture - mode identification

The oscillations of the magnetic field measured by Mirnov coils are created by rotating perturbations of current channels on rational magnetic surfaces. The use of poloidal and toroidal arrays of Mirnov coils makes it possible to identify

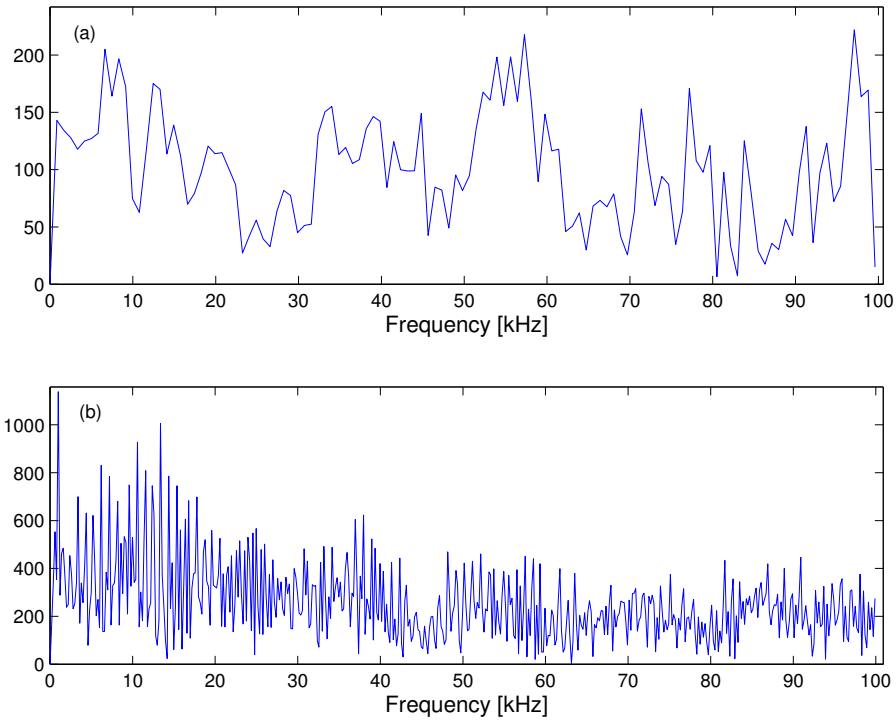

Figure 19: Fourier spectrum of the data shown in figure 18. (a) The Fourier spectrum of figure 18(a) gives only hints for the frequencies of the ELM precursors. (b) The Fourier spectrum of the six successive ELM-cycles of figure 18(b) is broad-band and it is difficult to identify any clear precursor frequencies.

the coherent structures of these rotating modes. Two different kinds of numerical techniques are used to determine the mode structure [26]:

The first method determines the mode number and structure by calculating the phase difference across a set of Mirnov coils at the frequencies of interest. Afterwards the mode numbers m and n are found by fitting the data using the function

$$\xi = m(\Theta - \lambda sin\Theta) + n\Phi + \delta_0 \tag{39}$$

where ξ is the calculated phase difference, Θ the poloidal and Φ the toroidal angle of the Mirnov coil, δ_0 is an additional phase difference between the coils and λ is a correction factor (see section 2.4). This method assumes that the modes have distinct frequencies and the phase angles are clearly identifiable. Thus the method fails in the presence of mode coupling or if the data is undersampled with respect to these frequencies.

A better analysis can be obtained by the singular value decomposition of a multichannel matrix whose columns are the measured time series [28]. Mathematically the singular value decomposition is equivalent to calculating the eigenvalues and eigenvectors of the matrix of covariances (or in short the covariance matrix) between the signals of different coils. The SVD therefore analyzes the spatial correlation in the multichannel data. As rotating coherent structures lead to repeating signals in the time series the SVD can identify the most important modes of the plasma. The singular vectors of the SVD represent the spatial structure of the modes. In most cases the singular values associated with one mode appear as a pair of values in the singular value spectrum. The corresponding singular vectors have a wave-like form and form sine-cosine pairs, which means that they are almost identical except for a phase difference of $\frac{\pi}{2}$ like sine and cosine functions of same frequency. This behaviour is a consequence of the oscillating parts of the modes, which has the form $cos(\omega t + \delta)$, where ω is the mode frequency and δ a phase angle. Since $cos(\omega t + \delta) = cos(\omega t) \cdot cos(\delta) - sin(\omega t) \cdot sin(\delta)$ the wave can be written as a sum of a time-dependent sine and a time-dependent cosine function.

If the magnetic field can be measured around the torus, the mode number of a single mode can be obtained by a polar plot of the corresponding singular vector. Fig. 20 shows the polar plot of the first two singular vectors, obtained from the SVD of the data from the Jet shot # 23324. In this plot the vessel cross-section has been used as a zero level and the components of the singular vectors have been plotted along the radii joining the centre of the vessel and the actual position of the coil. The points are joined by periodic splines and from the number of zero crossings $m = 4$ can be identified [28]. In addition the wavelength decreases from the outer to the inner side, as predicted by theory. The principal components that are the projection of the rows of the multichannel matrix onto the singular vectors, show the time evolution of the corresponding modes. Thus basic properties like growth rates of the modes and coupling between the modes can be investigated.

However, there are some limitations to this method. Modes with the same mode number but different frequencies are identified as one single mode; the same holds for modes with different mode numbers but the same frequency. A second problem is caused by the number of time series. If the number of modes is bigger than the number of time series some modes will be projected onto a single singular vector and thus they will be identified as a single mode. In addition if the dynamics of one mode is high dimensional (see section 2.4) it will be projected onto several singular vectors and thus more modes are identified than actually exist. These problems cause this simple multichannel SVD to fail in our case since only eight time series can be used for the creation of the multichannel matrix and the corresponding Mirnov coils are located only at the outer side of the torus. However, with a slight modification the method can still be made to work.

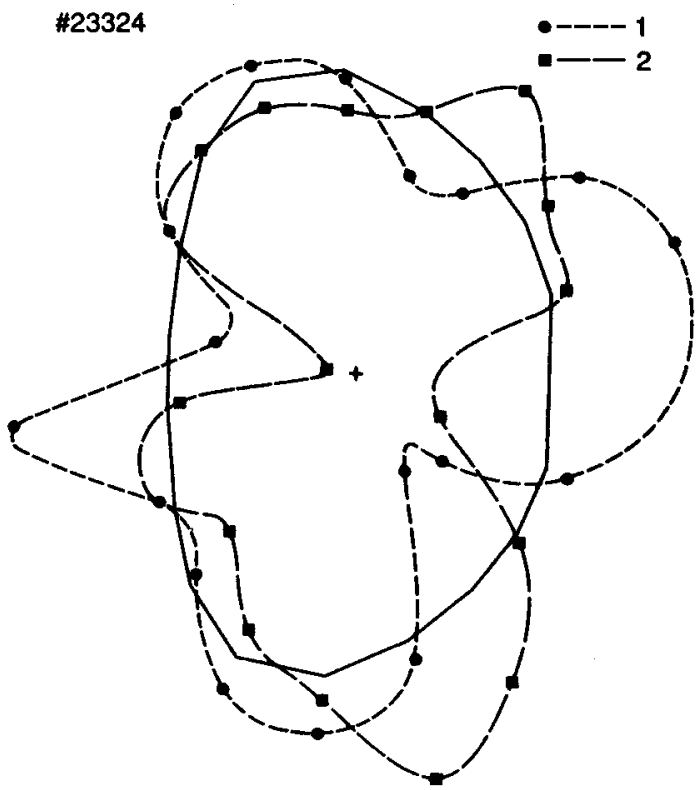

Figure 20: Polar plot of the first two singular vectors of the Jet pulse # 23324. The vessel cross-section is used as a zero line and the components of the singular vectors are joined with periodic splines. From reference [28].

Instead of using the eight time series, each time series is embedded in R^n using the method of delays. Afterwards eight trajectory matrices X_i are created and a new extended multichannel matrix is build in the following way:

$$X = (X_1|X_2|...|X_8) \tag{40}$$

This method has been used in the context of delay embedding by [29, 30]. Actually both methods - the simple and the extended multichannel method - are special cases of embeddings of the measurements. They try to create a differentiable equivalence between the dynamics of the plasma and the dynamics of the rows of the multichannel matrix. In contrast to the delay embedding of one time series this approach takes more details of the plasma dynamics into account since it uses more simultaneous measurements for the analysis. In addition the ratio between signal and noise is improved by the crosscorrelations between the single measurements, since the noise is in most cases uncorrelated between coils.

For the investigation an embedding dimension of $n = 26$ has been used for the creation of the single trajectory matrices. This embedding dimension has been chosen since the corresponding window length corresponds to the time scale of a sawtooth crash. The singular value spectrum of the multichannel trajectory matrix can be seen in figure 21.

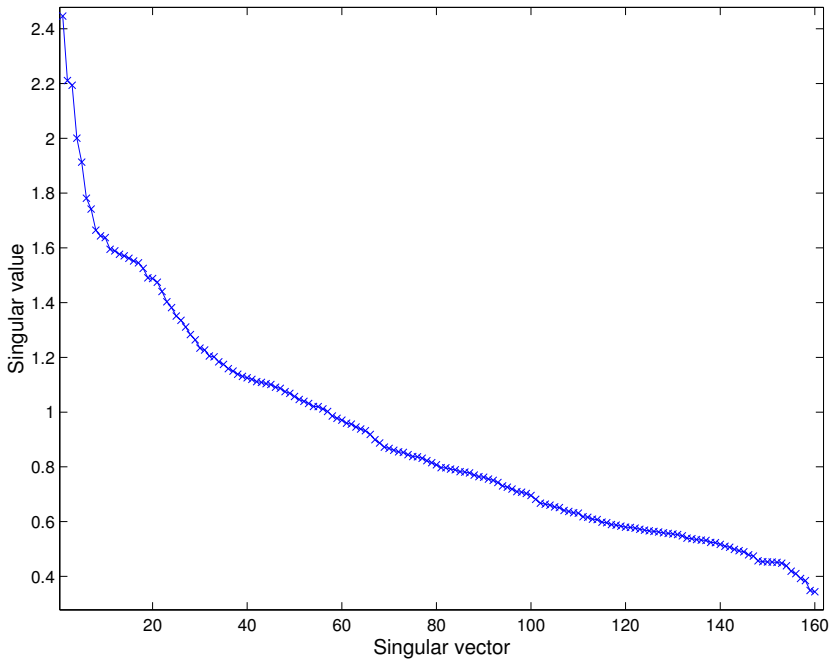

Figure 21: Singular value spectrum for the multichannel trajectory matrix. The first singular value is unpaired and significantly bigger than the others. Most singular values appear as pairs.

The first singular value is unpaired and significantly bigger than the others. The projection onto this singular value (figure 22(a)) shows the sawtooth like movement of the bulk plasma. The next two singular values are paired and their projections show a pulse-like oscillatory behaviour (fig. 22(b) and (c)). The next singular values are not paired but the corresponding singular vectors are in most cases sine-cosine pairs.

The occurrence of sine-cosine pairs supports the idea of a rotating coherent structure. However the analysis is incomplete and could be misleading. The SVD is a linear technique and is looking for linearly independent modes. However, since the modes are quasiperiodic and not perfect sinusoids, some of the principal components are or contain nonlinear copies of other principal components. This is comparable to the case of harmonics in Fourier analysis. To improve the picture of the plasma dynamics a nonlinear analysis is needed to identify which of the

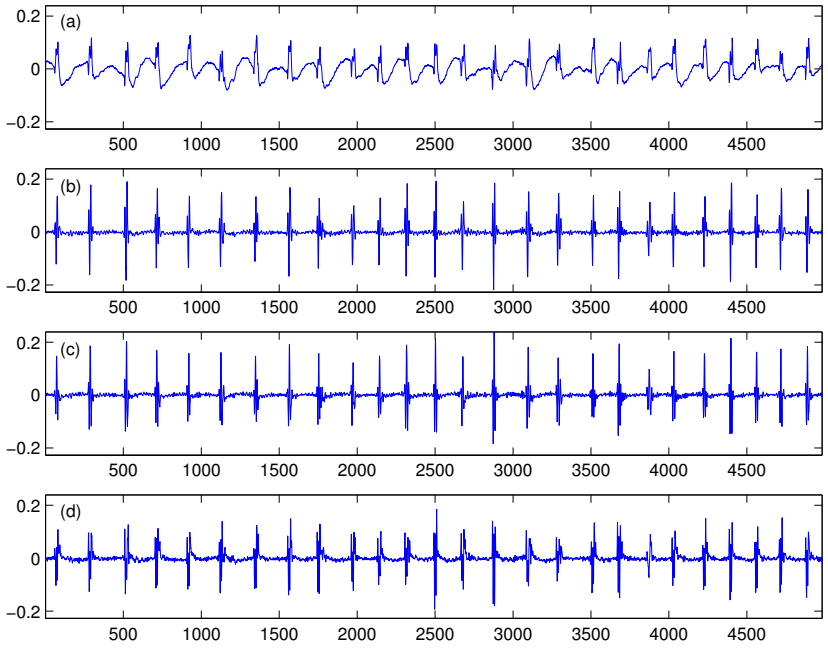

Figure 22: Projection of the trajectory matrix X onto the first four singular values. The first principal component shows a saw-tooth wave.

modes are harmonics of other modes and which contain dynamic independent of the other modes.

5.2 Nonlinear analysis

The key problem of the nonlinear analysis is to find out if there are nonlinear correlations between the principal components. This means we have to check if a function $f(x)$ exists such that

$$P_{i,k+1} \approx f(x_{i,k}) = f(P_{i,1}, P_{i,2}, ..., P_{i,k}) \tag{41}$$

where $x_{i,k} = (P_{i,1}, P_{i,2}, ..., P_{i,k})$ and $P_{i,j}$ is the ith component of the jth principal component. Since the measurements contain noise and some of the principal components consist of different kinds of dynamics each principal component can be expressed as a sum of three different components

$$P_{i,k+1} = f(x_{i,k}) + p_{i,k+1} + e_{i,k+1} \tag{42}$$

where $f(x_{i,k})$ is the harmonic of lower order principal components, $p_{i,k+1}$ is dynamic that is independent of the lower order principal components and $e_{i,k+1}$ is the noise.

Thus it is very difficult to find the function $f(x)$ explicitly and in the case of a simple mode identification not necessary. It is sufficient to find a good approximation $S(x)$ for $f(x)$ which enables us to identify the harmonics of the principal components. A good approximation of $f(x)$ can be obtained by using a sum of radial basis functions for $S(x)$

$$S(x) = \sum_{l=1}^{N} a_l \phi(\|x - x_{l,k}\|) \tag{43}$$

and calculating the a_ls by fitting the data with $S(x)$ [32], where ϕ is a suitably chosen function and $\|\cdot\|$ denotes the Euclidean norm. Basically equation (43) gives an interpolation problem where the $x_{i,k}$s are the interpolation points and the $P_{i,k+1}$s are the function values. The radial basis functions have been chosen for the approximation since they span a wide range in function space. This means that most nonlinear functions can be approximated by this class of functions. The radial basis functions can be considered as splines generalized to arbitrary dimensions. In this context the vectors $x_{l,k}$ are called centers. Popular examples of radial basis functions are [33]

- The thin-plate spline $\phi(r) = r^2 log(r)$
- The Gaussian $\phi(r) = exp(-cr^2)$
- The triharmonic spline $\phi(r) = r^3$

The approximation using the radial basis functions has the nice property that for almost every set of function values and interpolation points a smooth function $S(x)$ can be found that satisfies

$$P_{i,k+1} = S(x_{i,k}) \tag{44}$$

for every i, actually it is sufficient that $x_{i,k} \neq x_{j,k}$ for $i \neq j$ [34]. However this property has a disadvantage in our case, since we want to find out if $f(x)$ exists or not. To solve the problem of overfitting the data only a limited number p of centers are used which gives

$$S(x) = \sum_{l=1}^{p} a_l \phi(\|x - u_l\|) \tag{45}$$

where $u_l = (P_{i_l,1}, P_{i_l,2}, ..., P_{i_l,k})$. To find the optimum number of centers p_0 the given data has been divided into two equally big sets $S_1 = \{x_{1,k}, x_{2,k}, ..., x_{m,k}\}$ and $S_2 = \{x_{m+1,k}, x_{m+2,k}, ..., x_{N,k}\}$ and only S_1 has been used to calculate the coefficients a_l minimizing

$$E_1 = \sum_{i=1}^{m} \left\| P_{i,k+1} - \sum_{l=1}^{p} a_l \phi(\|x_{i,k} - u_l\|) \right\|^2 \tag{46}$$

afterwards the calculated coefficients have been used to calculate

$$E_2 = \sum_{i=m+1}^{N} \left\| P_{i,k+1} - \sum_{l=1}^{p} a_l \phi(\|x_{i,k} - u_l\|) \right\|^2 \tag{47}$$

For small values of p the fitting errors E_1 and E_2 are roughly the same and decrease for increasing p. If we increase p, only E_1 decreases further while E_2 stays constant or increases slightly, since increasing p only improves the fitting for the first set. Thus overfitting can be identified when E_2 is significantly larger than E_1. Thus p_o is the largest number of centers p for which the difference between E_1 and E_2 is not significantly large. After the optimum numbers of centers p_o has been found the residual σ'_{k+1} is calculated by minimizing

$$\sigma'_{k+1} = \sum_{i=1}^{N} \left\| P_{i,k+1} - \sum_{l=1}^{p_0} a_l \phi(\|x_{i,k} - u_l\|) \right\|^2 \tag{48}$$

In this minimization problem $e_{i,k+1}$ and $p_{i,k+1}$ appear as noise since they are uncorrelated with the lower order principal components. The σ'_ks are a measure for the fitting error and are connected to the singular values σ_k of the multichannel matrix. The comparison between the σ'_ks and the σ_ks shows how well the $(k+1)$th principal component can be expressed as a nonlinear function of the first k principal components. If $\sigma'_k \approx \sigma_k$ then the fitting error is big and no simple nonlinear dependence has been found, the principal components are uncorrelated. However if $\sigma'_k \ll \sigma_k$ most of the $(k+1)$th principal component can be expressed as a nonlinear version of the other principal components. Since noise is in most cases uncorrelated and cannot be predicted with nonlinear functions, the singular values and the corresponding residuals are the same for noise dominated principal components.

For the investigation of the nonlinear dependencies an embedding dimension of $n = 26$, the function $\phi(r) = r^3$ and to prevent overfitting 90 centers have been chosen for the fitting. The chosen data was taken from the time window from 0.17 to 0.195 seconds. During this period the plasma was stationary and the ELMs are well separated. The comparison between the singular values σ_k and

the residuals σ'_k (see fig. 23) shows that most of the principal components contain nonlinear contribution from lower order principal components.

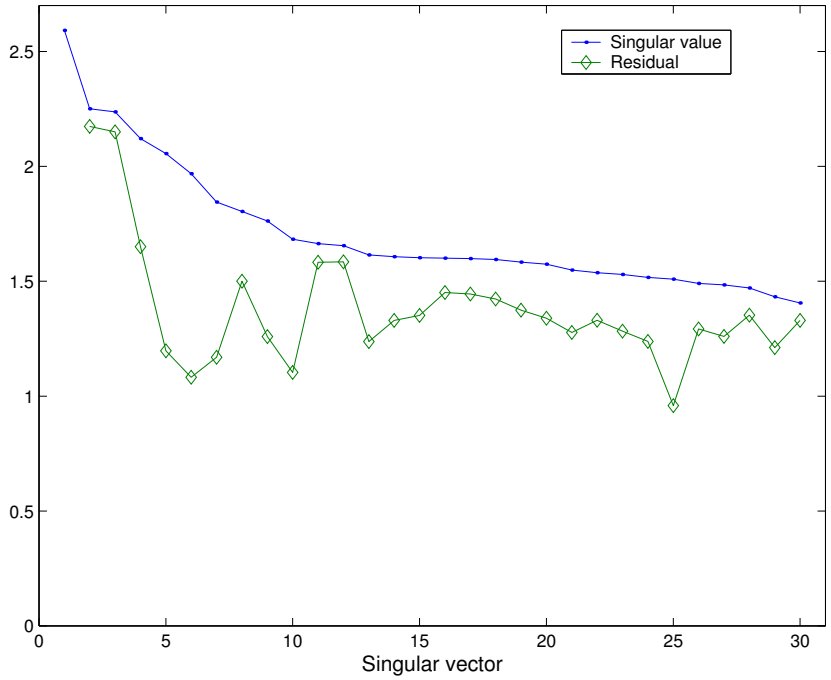

Figure 23: Singular value and residual spectrum of the extended multichannel matrix.

While the first three principal components are mostly independent of each other the spectrum of the residuals shows a significant drop for most of the higher order singular values. This indicates that these principal components can be predicted by the lower order ones using nonlinear functions. Almost all residuals drop to a constant value which can be identified as the noise level of the data. For principal components of order higher than 35, no significant difference between the singular values and residuals can be found. This suggests that these principal components are independent of the others and dominated by noise. However this conclusion can be misleading since the number of centers was fixed for the calculations which makes the fitting for higher order principal components less accurate.

Besides the large number of harmonic principal components some cannot be predicted by the other principal components; the residuals 1, 2, 3, 4, 8, 11 and 12 are comparable with the corresponding singular values. These principal components are independent of the others and represent the plasma modes. However since all lower order principal components have been used this analysis can give a too small number of independent modes. Assume for example that the principal component k is a real (independent) mode and the principal components $i, j < k$

have nonlinear contributions from the principal component k. Because of this it is possible, that the principal component k can be predicted with a nonlinear function using the principal components i and j and thus appears as a harmonic of other modes although it is a real mode.

In order to verify the mode identification a new nonlinear fit was calculated. In contrast to the one described above where all lower order principal components were used for the fit now only the principal components 1, 2, 3, 4, 5, 8, 11 and 12 are used. However, the calculation showed that these principal components are not sufficient to give the same result as figure 23. To get similar results as for the first fit the number of used principal components has to be expanded to 1, 2, 3, 4, 5, 8, 9, 11, 12, 17 and 18. Figure 24 shows the result of this fit. The comparison between the singular values and the residuals shows that in fact these 11 principal components are enough to predict the others, which means that the other principal components can be considered as harmonics.

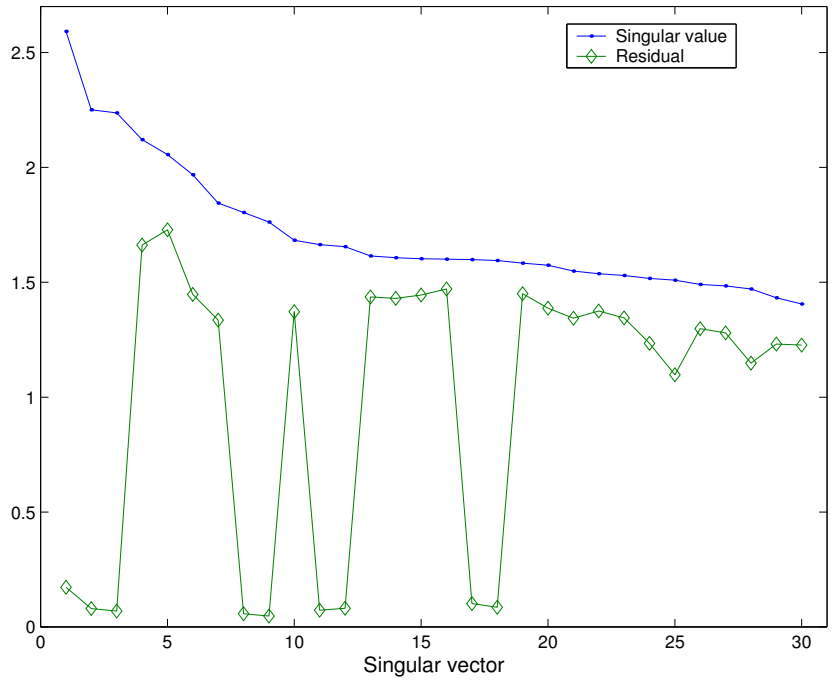

Figure 24: Singular value and residual spectrum of the extended multichannel matrix.

A clearer picture of the mode structure and of the rotation of the turbulence can be obtained by looking at the singular vectors. As mentioned in section 5.1 the singular vectors represent the spatial structure of the modes. The singular vectors of the extended multichannel matrix also have a block form. They consist of 8 blocks of length 26 and take the form

$$C_i = (c_{i,1}, c_{i,2}, ..., c_{i,208})^T = (C_{i,1}, C_{i,2}, ..., C_{i,8})^T \quad (49)$$

$$C_{i,j} = (c_{i,(j-1)\cdot 26+1}, c_{i,(j-1)\cdot 26+2}, ..., c_{i,j\cdot 26}) \quad (50)$$

Each individual block C_{ji} is related to the trajectory matrix X_j, which is associated with the Mirnov coil j, and has a waveform. The phase difference between the waves of the different blocks corresponds to the phase difference of the mode at the position of the different coils. In addition the amplitude of the wave for each block shows the contribution of the mode to the magnetic field at each coil. Thus the C_{ji} blocks show the spatio-temporal behaviour of the edge plasma. From these plots the phase difference between the different plasma positions can easily be identified which gives evidence of the rotation of the ELM turbulence. Figures 25, 26, 27 and 28 show the 3D plot of the C_{ij} blocks for the singular vectors 2, 8, 12 and 17 respectively. Looking at these figures a wave travelling through the plasma can clearly be identified.

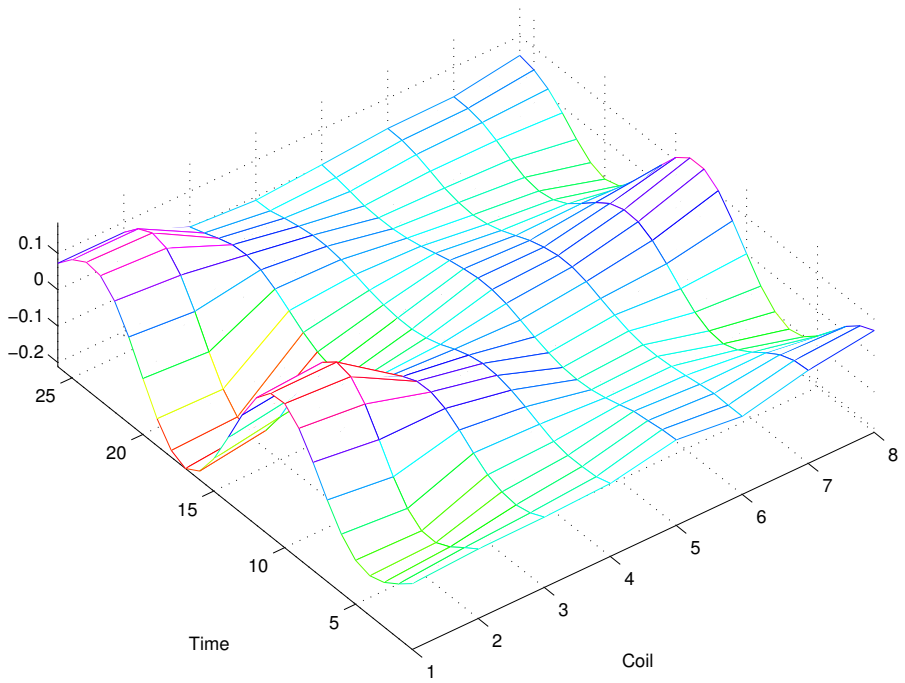

Figure 25: 3D plot of the 8 blocks of the second singular vector/outer mode.

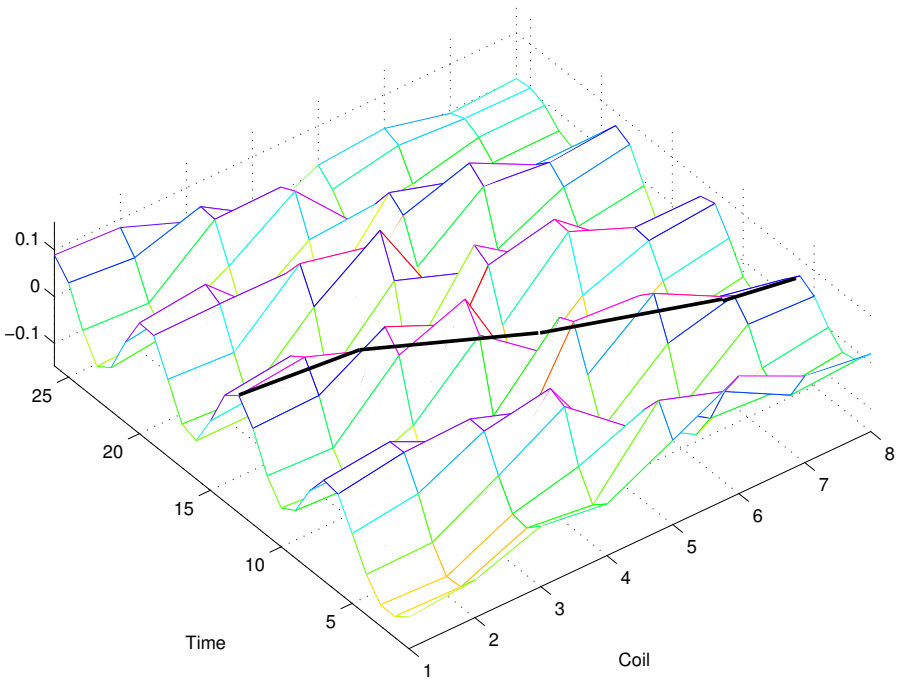

Figure 26: 3D plot of the 8 blocks of singular vector 8/common mode. The phase difference between the coils is indicated by the black line.

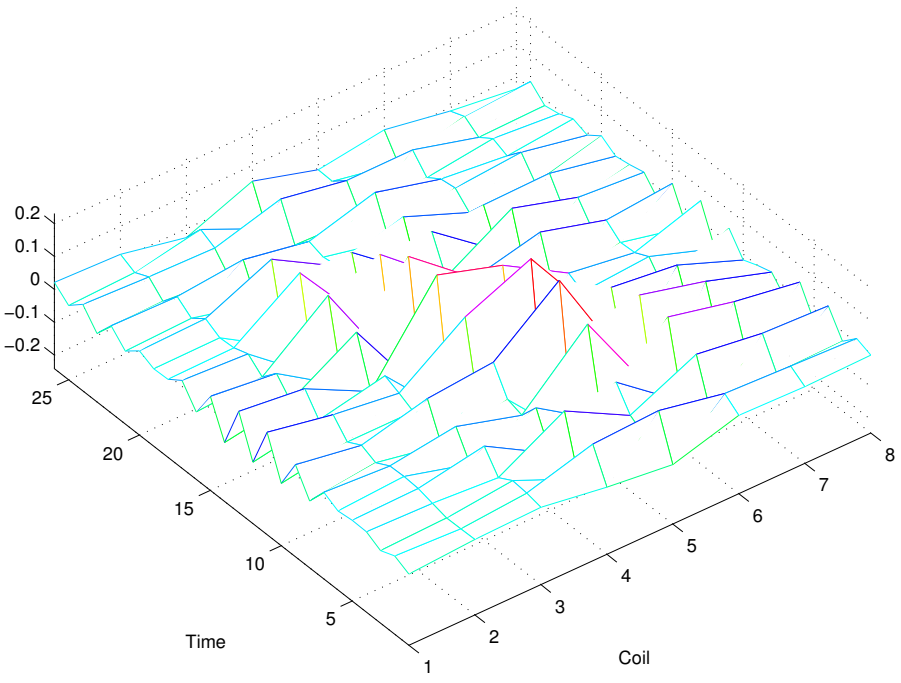

Figure 27: 3D plot of the 8 blocks of singular vector 12/Nyquist mode.

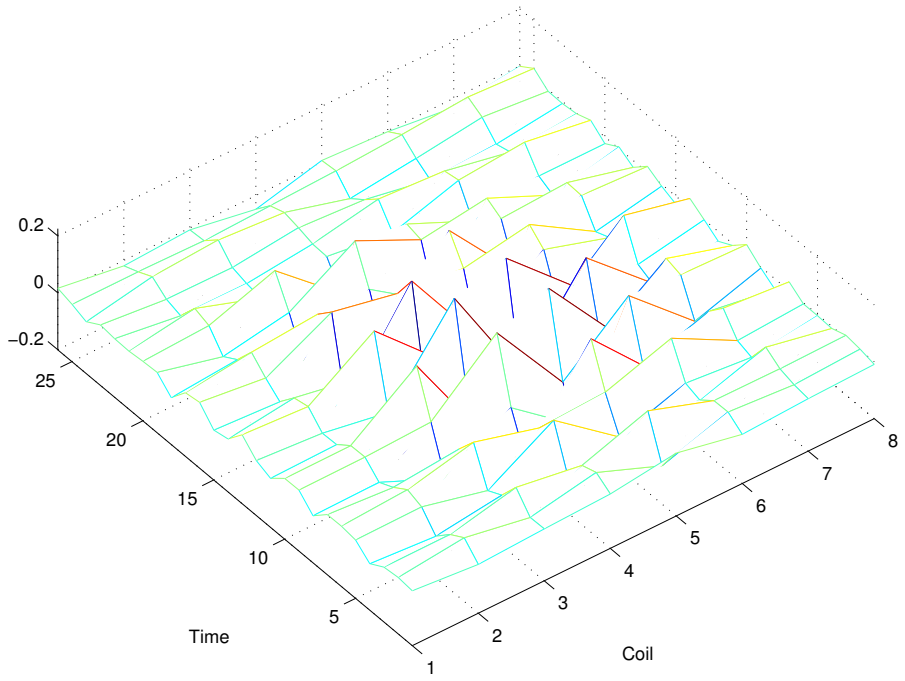

Figure 28: 3D plot of the 8 blocks of singular vector 17/inner mode.

In addition to the spatial mode structure the frequency of the precursor modes can be identified in the Fourier spectrum of the principal components. The contribution of these modes to the ELM at the different Mirnov coils can be estimated by the amplitude of the corresponding block of the singular vector. The Fourier spectrum of the corresponding principal components and the comparison of the singular vectors shows that except for the first singular vector all other singular vectors are paired and form a sine-cosine pair. The Fourier spectrum of the second and third principal component (figure 29) has only one peak centred at a frequency of about 14 kHz. Because of aliasing this frequency is not necessary the right frequency and could also be 186 kHz or 214 kHz. Figures 25 and 31 show that only the signal of coils # 5, 4 and 21 have a contribution from these modes. Coils # 5 and 4 have almost the same phase while coil # 21 is in anti phase to the first two coils. In the following this mode will be called the “outer mode”, because coils # 5, 4 and 21 have a greater distance from the plasma than the other coils.

The Fourier spectra of the fourth and fifth principal components (figure 30) are identical and show two peaks which are symmetric with respect to the frequency 14 kHz, the same frequency that was found for the second and third principal component. The contribution of this mode to the individual coils is similar to the contribution of the previous mode. These two properties - Fourier spectrum

and contribution to the coils - indicates that the principal components 2, 3, 4 and 5 should be interpreted as being the same mode. The projection of this mode onto four singular vectors could be caused by a high-dimensional ELM-envelope of this mode. Thus these four singular vectors can be considered as one single mode, whose dynamic is projected onto four singular vectors.

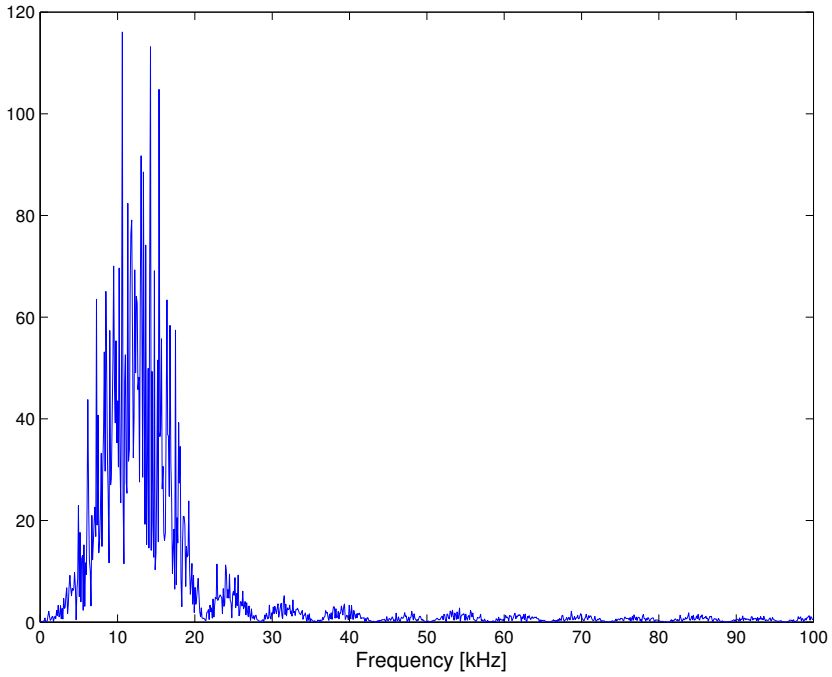

Figure 29: Fourier spectrum of the second and third principal component. The spectrum shows one peak centred at 14 kHz.

For the principal components 8 and 9 again only one peak centred at a frequency of 32 kHz can be found. In contrast to the mode above all coils have contributions from this mode (fig. 26, 31). The phase difference between the individual coils can clearly be identified and has a S-like shape as indicated by the line in figure 26. This S shaped phase difference is well known [15] and can also be found in figure 25 (here the amplitude of the inner coils is so small that a clear identification of the phase difference is difficult). In the following this mode will be called the "common mode".

For the principal components 11 and 12 the inner coils show a bigger contribution from this mode, which will be called the "Nyquist mode". The Fourier spectra of the two principal components are similar and show one peak centered at 93 kHz. The frequency of this mode lies close to the Nyquist limit which makes it difficult to identify the phase difference but it appears to be the same as for the modes before (fig. 27). The last two principal components 17 and 18 show a similar

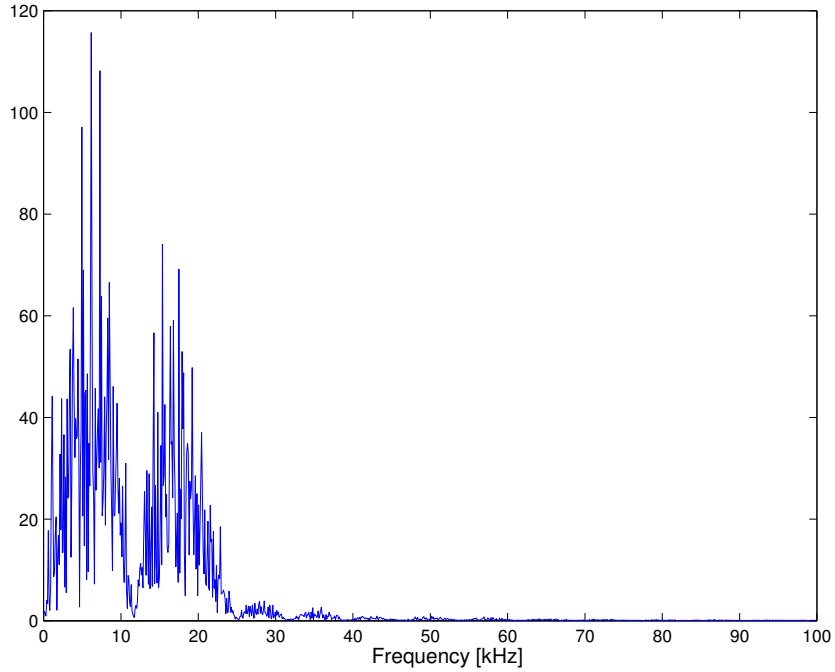

Figure 30: Fourier spectrum for the fourth and fifth principal component. The spectrum shows two peaks which are symmetric with respect to the frequency 14 kHz.

behaviour (fig. 28). Their Fourier spectra show a big peak at a frequency of 60 kHz. Again the inner coils show a bigger contribution from this mode. In the following it will be called the "inner mode". As mentioned before the contribution of the modes to the single measurements can be obtained by the amplitude of the corresponding block of the singular vector. Figure 31 shows the amplitude distribution for the identified modes. The sawtooth mode (singular vector 1) and the outer mode (singular vectors 2, 3, 4 and 5) are dominant for the outer coils 5, 4, 22 and 21. The common mode (singular vectors 8 and 9) is equally strong for all coils. The other two modes have big amplitudes for the inner coils 2, 1, 24 and 23. Since the magnetic field of a mode with mode number m decays with radius like $r^{-(m+1)}$ [31], a possible explanation for this distribution could be the different distance of the coils from the plasma which means that the identified modes could be located on different surfaces in the plasma and/or have different mode numbers.

So far the mode analysis was only performed for the period ranging from 0.17 to 0.195 seconds. During this period the plasma was in a quasi stationary state. For a more complete analysis of the modes the analysis was extended to the period from 0.15 to 0.195 seconds. For this the whole time interval was divided

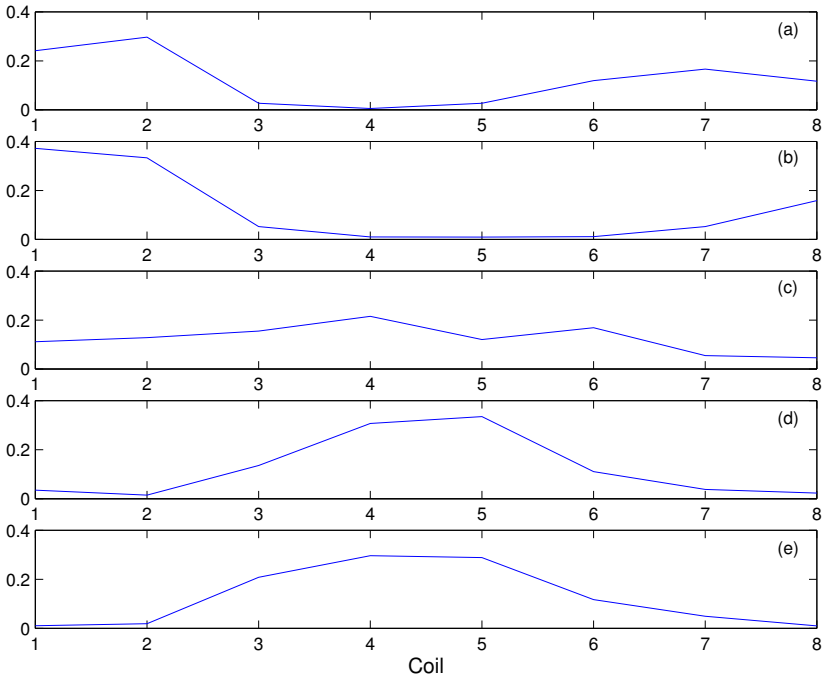

Figure 31: Contribution of the modes to the measured signal. The saw-tooth (a) and the outer mode (b) are dominant at the outer coils. The common mode (c) is equally strong for almost all coils. The last two modes, Nyquist and inner mode, (d and e) are very dominant for the inner coils.

into succeeding intervals of 10 ms and for each of these the mode analysis was performed. During each period the same number of independent modes could be found but the frequencies of these modes were found to change during the discharge. The outer mode is dominant for the outer coils # 5, 4 and 21. Its frequency varies between 12 and 16 kHz during the discharge. The singular values of this mode always appear at position 2 to 5 in the singular value spectrum. The frequency of the common mode also changes during the discharge and ranges from 33 to 36 kHz. The position of its singular values varies - in some periods they appear before, in others after the singular values of the Nyquist mode. This means that in some periods the common mode is the second most important mode while in others it is the Nyquist mode which dominates. The frequency of the Nyquist mode also varies and lies between 89 and 99 kHz. The singular values of the inner mode always appear behind the singular values of the other three modes. Its frequency ranges from 58 to 69 kHz. Since the mode number cannot be obtained from the singular vectors in this case it is not clear if the modes are unchanged during the investigated time and the change in the frequencies is due to noise and small changes of the plasma parameters or if the modes themselves are

changing, which means that in some periods some modes disappear while other modes evolve. However since the changes of the frequencies are small compared with the absolute value of the frequency and the behavior of the modes are quite similar during the periods it is more likely that the same modes are present during the discharge.

The identified modes are in good agreement with a recently published investigation of edge magnetic turbulence in COMPASS-D [22]. In this article several modes have been identified during ELMs and in ELM-free periods. Three of these modes - with frequencies 60, 120 and 280 kHz respectively - can be found in ELM-free periods as well as during ELMs. These modes seem to be invariant and permanent features of the discharge which are strongly excited during ELMs. If we take aliasing into account then these three modes are in good agreement with the Nyquist and inner mode. An additional characteristic of the modes is the fact that their activity can be seen on some of coils but not on all of them. The study of the ELMs showed ELM precursors around 220 kHz which appear prior to type I ELMs. However it is not clearly resolved whether on COMPASS-D the type I ELMs are really type I ELMs or actually large type III ELMs. If we compare these precursors with the earlier identified modes then we can see that the outer and common mode agree very well with these precursors. Bearing this in mind we get the following picture:

The Nyquist and inner mode are plasma modes that are present during the whole discharge. In ELMy H-mode they are strongly excited during ELMs and show an intermittent behavior. The outer and common mode appear only in ELMy H-mode and are the precursors of the ELMs. It is possible that the last two modes are the driving modes during the ELMs and drive the other two modes unstable.

For the further analysis it is necessary to investigate the single modes individually. Thus a filtering technique that separates the modes has to be applied to the measured data. Since the Fourier spectrum does not allow to identify the modes simple Fourier filter techniques fail. A better filter based on the mode identification presented above shows better results and will be described in the next section.

5.3 Separation of the modes

As shown in the previous section there exists a correspondence between the modes and the singular values of the singular value decomposition. Since the principal components of these singular vectors represent the time evolution of the corresponding coordinates of the delay vectors, the time evolution of the mode itself can be deduced from the coordinates. The key idea of the following mode separation is to use the principal components of one mode to create a new time series

that mostly contains contributions from the magnetic field created by this mode. A similar filtering technique for the separation of data from noise has been used by [23].

Suppose the signal $x_j(t_l)$ measured by the coil j, $1 \leq j \leq M$ and $1 \leq l \leq N_m$ can be written in the following form

$$x_j(t_l) = m_j(t_l) + n_j(t_l) \tag{51}$$

where $m_j(t_l)$ is the magnetic field created by the mode we want to separate and $n_j(t_l)$ is a second magnetic field created by all the other modes and noise. After embedding each time series $x_j(t_l)$ in R^n and creating M trajectory matrices X_j we get an N by $n \cdot M$ extended multichannel matrix as described earlier. Suppose that the singular value decomposition of the matrix

$$X = S\Sigma C^T \tag{52}$$

identifies the mode and the singular vectors $C_1, C_2, ..., C_k$, $k \leq n \cdot M$ are the identified singular vectors of this mode. A way to get a good approximation for $m_j(t_l)$ is to set all the singular values of order higher than k to zero. Thus we get a new singular value spectrum

$$\hat{\sigma}_i = \begin{cases} \sigma_i & , \quad 1 \leq i \leq k \\ 0 & , \quad k < i \leq n \cdot M \end{cases} \tag{53}$$

Using the singular values $\hat{\sigma}_i$ we can create an new diagonal $n \cdot M$ by $n \cdot M$ matrix $\hat{\Sigma}$ where the diagonal elements are the $\hat{\sigma}_i$s. The multiplication of the matrices S, $\hat{\Sigma}$ and C^T gives an new extended multichannel matrix $\hat{X}$

$$\hat{X} = S\hat{\Sigma}C^T = \left(\hat{X_1}|\hat{X_2}|...|\hat{X_M}\right) \tag{54}$$

that itself consist of M trajectory matrices $\hat{X}_j$. Each matrix $\hat{X}_j$ is an approximation of the trajectory matrix that would be created if $x_j(t_l) = m_j(t_l)$. Finally to get an approximation $\hat{m}_j(t_l)$ of $m_j(t_l)$ we have to average over the diagonals of $\hat{X}_j$ or in a mathematical notation

$$\hat{m}_j(t_l) = \frac{1}{l}\sum_{i=1}^{l} \hat{X}_{l-i+1,i} \qquad , 1 \leq l < n \tag{55}$$

$$\hat{m}_j(t_l) = \frac{1}{n}\sum_{i=1}^{n} \hat{X}_{l-i+1,i} \qquad , n \leq l \leq N \tag{56}$$

$$\hat{m}_j(t_l) = \frac{1}{N+n-l}\sum_{i=l-N+1}^{n} \hat{X}_{l-i+1,i} \quad , N < l \leq N+n-1 = N_m \tag{57}$$

The resulting M new time series $\hat{m}_j(t_l)$ can be interpreted as a new measurement function on the plasma. This new measurement function emphasizes the magnetic field created by the mode and in the context of delay embedding allows to recreate the dynamics of the mode. By applying this method to the measured data from the Mirnov coils the modes can be separated and analyzed.

5.4 Local linear model - growth rates

The application of the filter described in the previous section gives eight new time series for each mode. All time series show oscillatory behaviour around their mean value. This mean value can be interpreted as the magnetic signal of the stable plasma and represents a fixed point of the physical system. Thus the mean value was subtracted from each time series to simplify the embedding. From each time series the data from 0.15 to 0.195 s was embedded using several different embedding dimensions. During this time window, the ELMs appear and are clearly distinguishable. For each embedding dimension the dimension of the mode and a local linear model were calculated. For small and big embedding dimensions the calculated dimensions and eigenvalues changed with the embedding dimension. However, for embedding dimensions between $n = 20$ and $n = 30$ the calculated values were stable. The reason for this behaviour lies in the fact that a minimum embedding dimension is necessary to create an embedding and that for big embedding dimensions the measured points become uncorrelated. For the following analysis an embedding dimension of $n = 26$ was chosen.

For the estimation $\hat{m}$ of the dimensionality m of the dynamics of the modes a local and global singular value decomposition was performed. As mentioned in section 3.4 these two methods give two estimates for m. The results from the global singular value decomposition are shown in figures 32 and 33. For the outer, the common and the inner mode the global singular value decomposition shows the same picture. 8 singular values are separated from the noise floor which gives $\hat{m} = 8$ as an estimation for the dimensionality. The Nyquist mode shows a different behaviour. Here 10 singular values lie above the noise floor

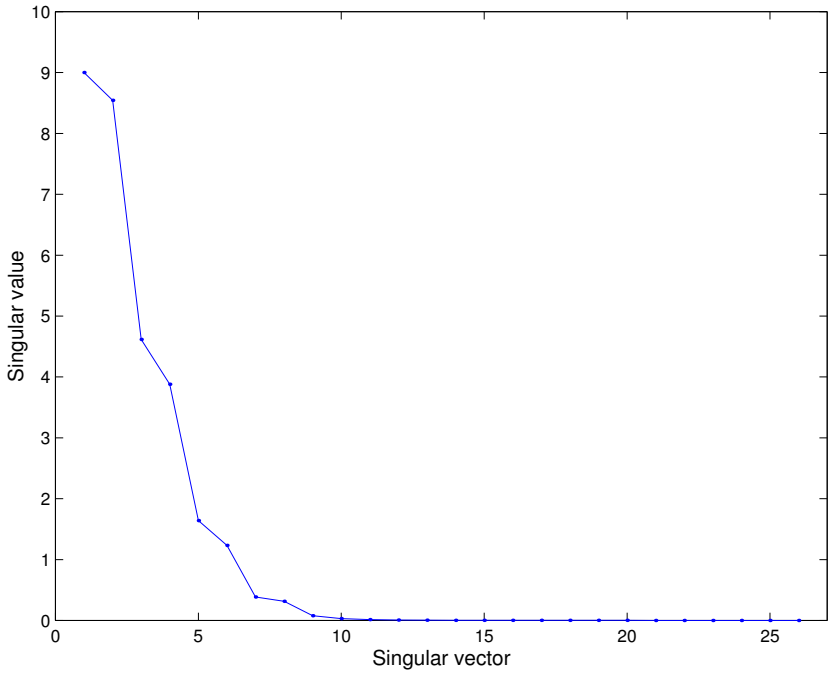

Figure 32: Singular value spectrum of the outer mode. The common and the inner mode show a similar picture

which gives an dimensionality of $\hat{m} = 10$. The two different numbers for $\hat{m}$ are no contradiction since there is no reason why the modes should have the same dimensionality.

A second estimate for the dimensionality can be obtained by the local singular value decomposition. The scaling of singular values is shown in figure 34 and 35. For comparison of the scaling a solid line with slope one is drawn in the figures. Now in contrast to the global singular value decomposition all scalings show a similar behaviour. The first 6 singular values scale linearly for small ball radii ε. All other singular values scale quadratically or have an even higher slope. This gives $\hat{m} = 6$ as an estimation for the dimensionality.

Using the results of the global and local singular value decomposition we get $6 \leq m \leq 10$ for the dimensionality of the modes. For the calculation of the local linear model all five dimensions (6, 7, 8, 9 and 10) have been used. However the increase of m from 6 to 10 resulted in an increase of eigenvalues with negative real parts while the eigenvalues with positive real parts kept constant. To identify which eigenvalues are part of the linear model and which are spurious eigenvalues, which result from using a too big dimension m, the time series were reversed in time and the eigenvalues were calculated for the reversed time series. In this calculation all the eigenvalues of the linear model should appear with reversed

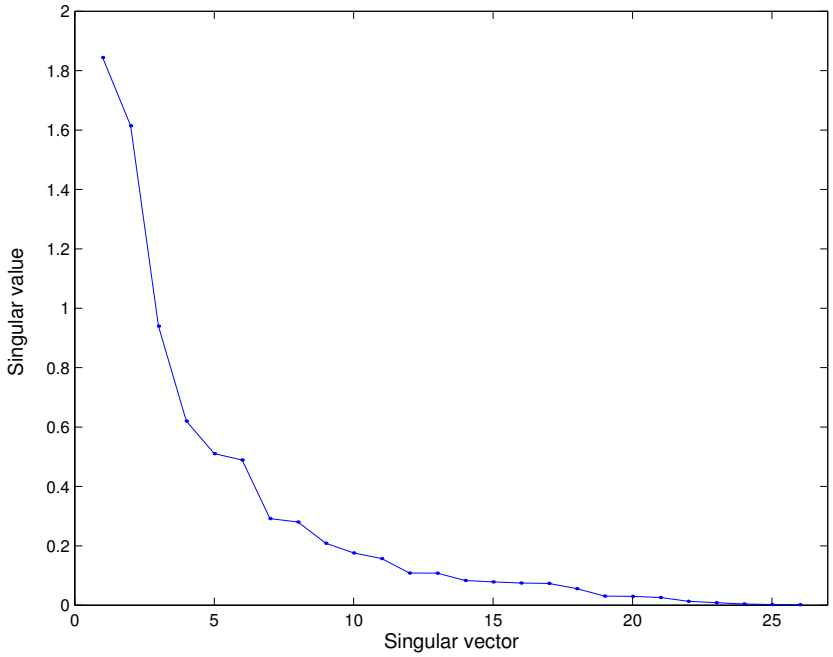

Figure 33: Singular value spectrum of the Nyquist mode.

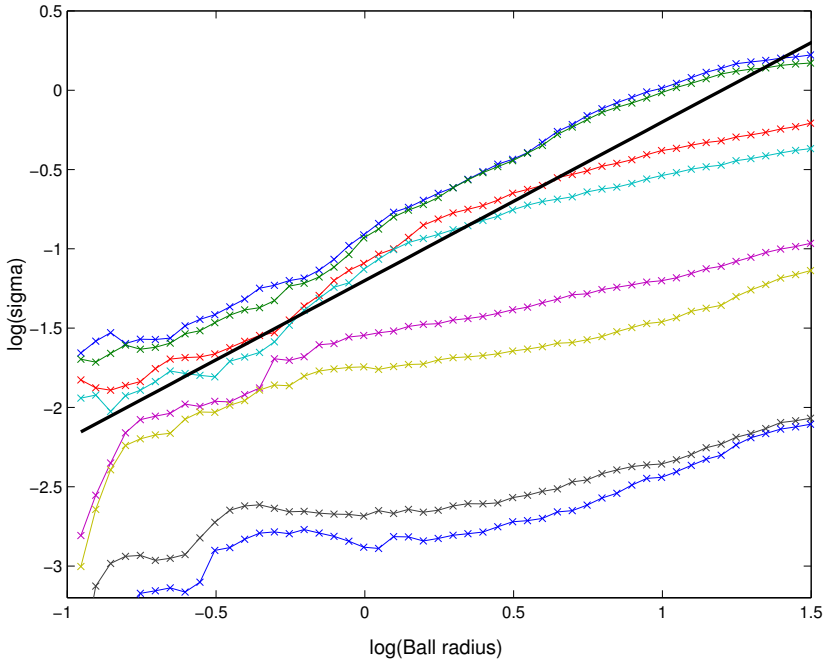

Figure 34: Scaling of the singular values for the outer, common and inner mode

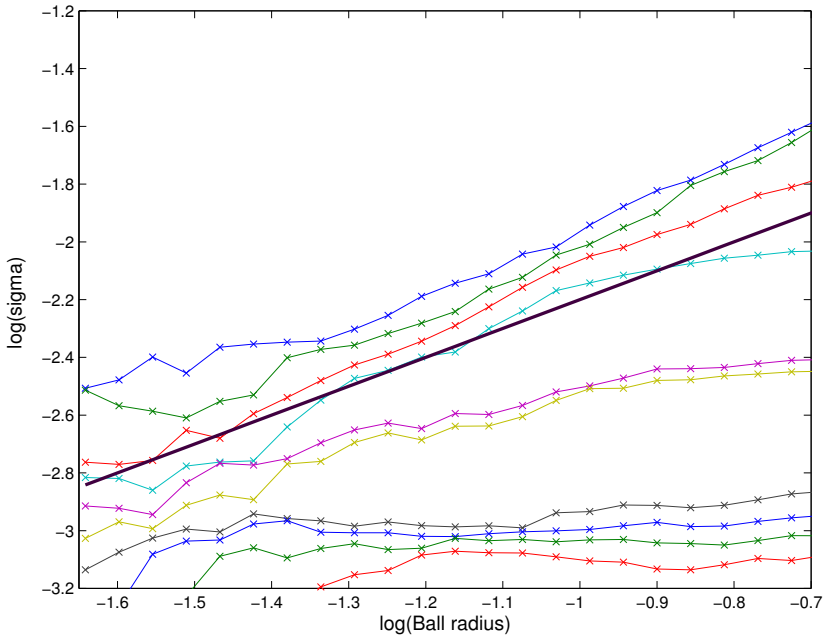

Figure 35: Scaling of the singular values for the Nyquist mode

signs and for all spurious eigenvalues new independent eigenvalues should appear. Using this method the dimensionality could be reduced to $m = 6$. However this method of a reversed time series has to be treated very carefully. As mentioned in [24] noise can cause true eigenvalues to appear spurious giving wrong results.

A typical scaling of the real and imaginary eigenvalues is shown in figure 36 and 37. For small ball radii the singular values change very fast since the noise is of the order of the signal. When we increase the ball radius the real parts become more positive or negative (depending on the sign of the real part) until they reach a maximum/minimum value. Near their maximum/minimum value the real parts are quite constant and give the best estimations for the eigenvalues of the linear model. If we further increase the ball radius the real parts tend to zero and take negative values with a small absolute value. The scaling of the imaginary values shows less variation when increasing the ball radius. For small radii the values change fast which is due to the noise. Increasing the radius gives relatively small changes in the values.

This behaviour can be explained in the following way. For small and medium radii the system is passing by the fixed point giving an inward flow and an outward flow. If we calculate the eigenvalues in this case we get complex eigenvalues with big real parts. The imaginary part of the eigenvalues can in some way be attributed to the frequency of the plasma rotation. If the radius increases further the system looks in phase space more like a circulating flow leaving and returning

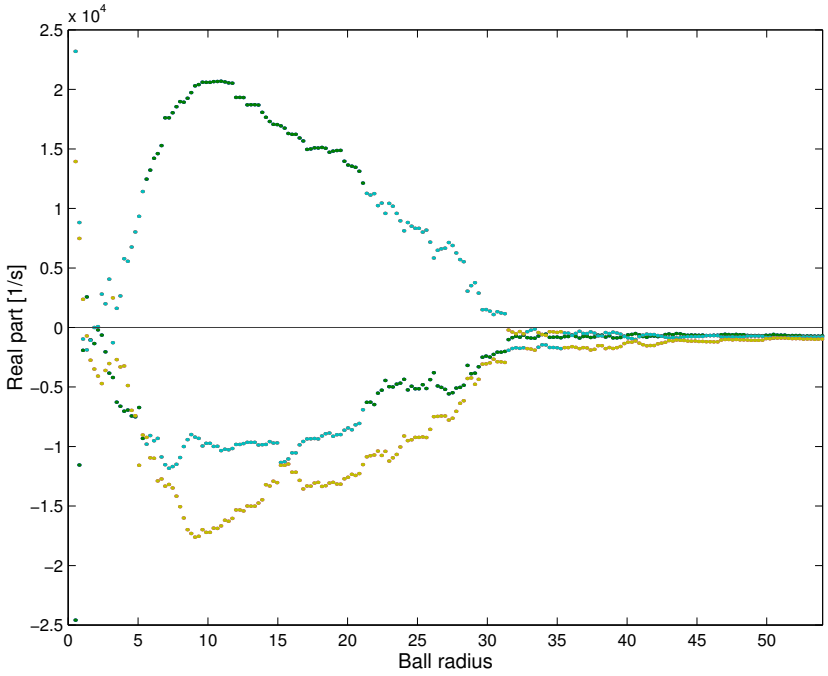

Figure 36: Scaling of the real part of the eigenvalues.

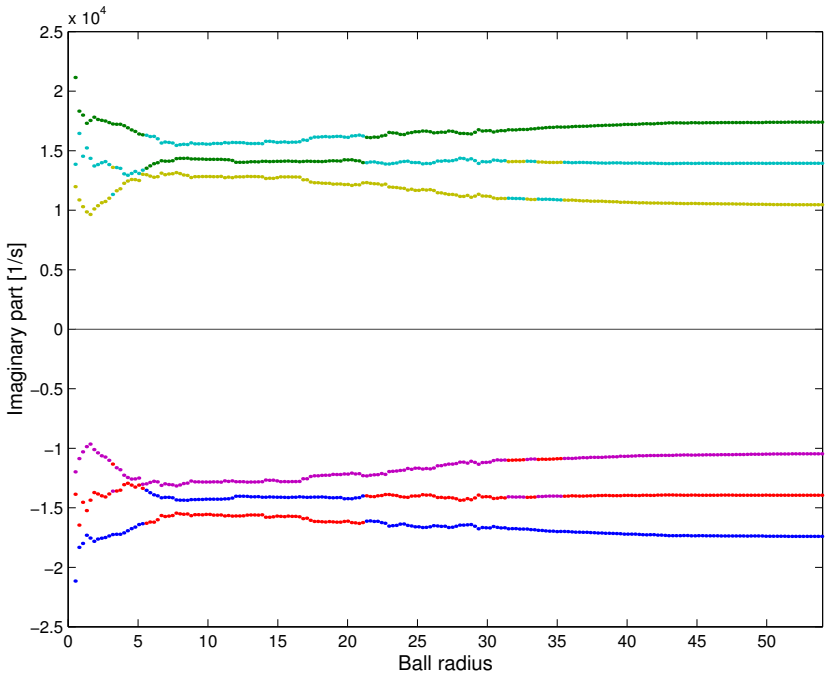

Figure 37: Scaling of the imaginary part of the eigenvalues.

to the fixed point. In this case the eigenvalues have almost vanishing real parts. The rotation frequency of the circulating flow causes a change in the imaginary part of eigenvalues, which can be seen in figure 37 for radii greater than 20. Another reason for the scaling behaviour is the fact that the linear model is only locally valid and for bigger radii the nonlinearities give wrong values, additionally since the global dimension of the embedding is bigger than the local dimension of the modes the projection of the higher space onto a smaller one causes wrong values for bigger radii.

A second criteria for the choice of the maximum radius for the estimation is given by the time evolution of the magnitude of the delay vectors. This magnitude is proportional to the amplitude of the ELM and thus the magnitude of the delay vectors shows an exponential growth similar to the growth of the amplitude of the ELM precursors. In figure 38 the magnitude of the delay vectors used for figures 36 and 37 is shown.

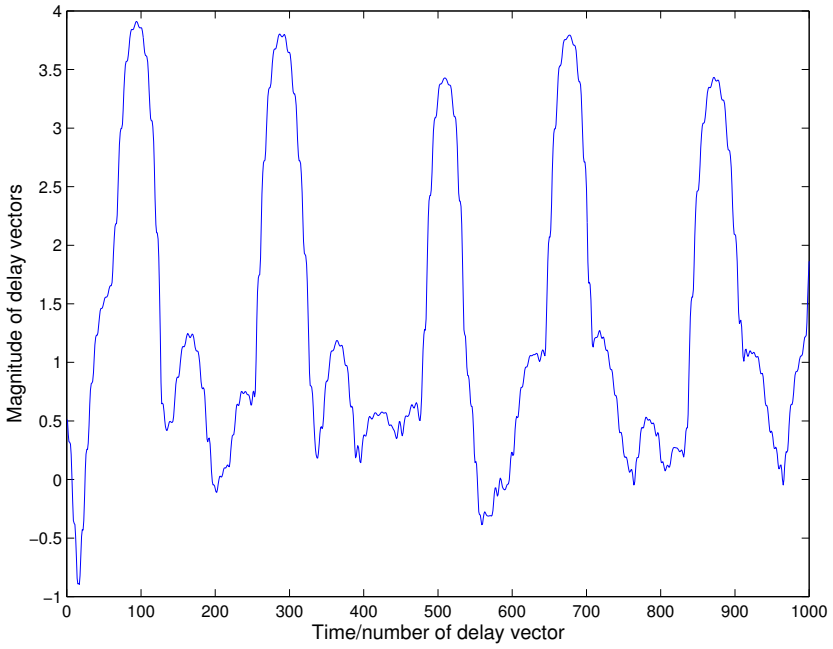

Figure 38: Time dependence of the natural logarithm of the magnitude of the delay vectors.

Here the number of the delay vector can be considered as the time. For radii smaller than 3 ($\log(3)\approx 1.1$) the effect of noise is very dominant and no clear time dependence can be identified. However for radii between 5 ($\log(5)\approx 1.6$) and 20 ($\log(20)\approx 3$) the magnitude increases exponentially with time. Since we are interested in this exponential growth this gives an lower and an upper bound for the radius that should be used in the estimation of the eigenvalues.

In order to calculate the time dependence of the linear model the chosen time window was divided into eight overlapping time windows of length 10 ms. For each time window the local linear model was calculated. The results for the outer mode are shown in table 3. The eigenvalues have been averaged over the stable regions of the scaling. For the first (0.15-0.16s) and second (0.16-0.17s) time window the forward calculation of the eigenvalues showed two regions where the eigenvalues were constant. Thus the eigenvalues have been calculated for both regions and are given in table 3. During the first two time windows the plasma changes from L- to H-mode. This change causes a great amount of perturbation in the plasma which causes difficulties for the calculation of the linear model. Thus the eigenvalues calculated in forward and reversed time do not agree very well, especially one of the three real parts has an opposite sign for the two time directions. From 0.17 seconds onwards the plasma is in ELMy H-mode. Here all three pairs of complex conjugate eigenvalues agree very well for both time directions. As table 3 shows the growth and decay rates increase during the transition from L- to H-mode and reach a constant level during the ELMy H-mode.

The common mode shows a similar behaviour. Two stable regions could be identified for the backward calculation in the first (0.15-0.16s) and for the forward calculation in the second (0.16-0.17s) time window. The agreement between the eigenvalues calculated in the forward and backward direction is slightly better than for the outer mode. Again the growth and decay rates increase during the transition from L- to H- mode but they reach a constant level during ELMy H-mode. However the absolute value of both the growth and decay rates of this mode is smaller compared with the corresponding rates of the first mode.

Since the Nyquist mode's frequency of 93 kHz (107 kHz) lies close to the Nyquist limit the separation of this mode from the other modes and noise is very difficult. In addition since only three samples per mode cycle are available the calculation of a linear model is very inaccurate. Therefore for the third mode no reasonable results could be obtained.

The Nyquist limit also causes small problems for the calculation of the eigenvalues of the inner mode. Since the Nyquist frequency should be bigger than twice the frequency of the mode it is a little bit too small for the fourth mode whose frequency is about 57 kHz. This might explain why the agreement between the backward and forward eigenvalues is less good as for the previous modes. For the eigenvalues two time windows with two stable regions could be identified and the eigenvalues for both regions were calculated. The time dependence of the growth/decay rates show a deviation from the rates of the other modes. The rates are increasing during the L- to H-mode transition and they reach a maximum value between 0.17 and 0.18s. In contrast to the previous modes this time the growth/decay rates do not saturate but become smaller after 0.18s.

Outer mode				
Time	Growth rate $[s^{-1}]$	Frequency [Hz]	Growth rate backward $[s^{-1}]$	Frequency backward [Hz]
0.15 -	7727.2	15096	4843.7	14952
0.16 s	-1632.7	15959	-3197.3	15812
	-5841.9	11486	1546.3	10791
0.15 -	2599.6	15805	-	-
0.16 s	-1485.1	15013	-	-
	-2993.2	10723	-	-
0.155 -	14140	14492	16179	14281
0.165 s	-6207	15325	-5225	15410
	-8274	11749	-5982	11967
0.16 -	11153	14083	13685	13543
0.17 s	-4142	14566	1069	14898
	-10239	12648	-10283	12781
0.16 -	1663	15721	-	-
0.17 s	-1917.6	14176	-	-
	-3198.3	11474	-	-
0.165 -	16782	14605	18537	14521
0.175 s	-18013	13492	-16439	13624
	-1669	13473	1213	13410
0.17 -	20123	13398	22024	14351
0.18 s	-13927	15728	-12427	15711
	-9261	11735	-7119	11943
0.175 -	19290	14066	21204	13844
0.185 s	-12068	15529	-9117	15483
	-11390	12608	-9518	12810
0.18 -	18589	13733	20187	13523
0.19 s	-15147	13976	-13711	13748
	-7914	15208	-4164	15588
0.185 -	20530	14281	20823	14049
0.195 s	-16938	12810	-11735	13049
	-9847	15603	-8059	15582

Table 3: Calculated growth rates and frequencies for the outer mode.

Common mode				
Time	Growth rate $[s^-1]$	Frequency [Hz]	Growth rate backward $[s^-1]$	Frequency backward [Hz]
0.15 -	3185.3	34056	5966.9	33367
0.16 s	-3163.1	33578	-5344.1	31502
	-3853.3	33512	-5960	36196
0.15 -	-	-	6130.3	33743
0.16 s	-	-	-1600.3	31106
	-	-	-2050.3	36286
0.155 -	8558.6	34014	11369	33954
0.165 s	-4233.6	32033	-2734	31807
	-9463.6	36142	-7520	36356
0.16 -	6996.5	33702	9634.8	33780
0.17 s	-6753	32188	-5340.0	31977
	-5499.1	35976	-3663.4	36048
0.16 -	11052	34071	-	-
0.17 s	-3114.3	36543	-	-
	-1676	31259	-	-
0.165 -	8858.1	33522	10460	33742
0.175 s	-9816.5	31641	- 7911	31695
	-879.7	36137	470	35957
0.17 -	9107	33377	11339	33209
0.18 s	-8595	32204	-7545	32105
	-2002.7	36227	-2103	36205
0.175 -	6912.1	33045	8775.0	33035
0.185 s	-7075.7	32476	-5398.5	32541
	-2589.1	36681	-1185.1	36671
0.18 -	-10466	31696	-7746.5	31582
0.19 s	6745	33161	7891.4	33164
	325	36589	1369.9	36409
0.185 -	-11453	31912	-9212.5	31924
0.195 s	8211	32877	9711.3	32923
	474	36063	1412.7	36007

Table 4: Calculated growth rates and frequencies for the common mode.

Inner mode				
Time	Growth rate $[s^-1]$	Frequency [Hz]	Growth rate backward $[s^-1]$	Frequency backward [Hz]
0.15 -	5510	56592	10118	57107
0.16 s	-10751	56046	-4130	55040
	-842	60066	2007	60068
0.155 -	2267.2	56950	3184.4	568778
0.165 s	-4352.8	59145	-2519.7	59220
	404.6	44020	8278.3	44136
0.16 -	8931	57999	11183	57952
0.17 s	-11029	58479	-8622	58352
	-11961	44917	1706	43545
0.165 -	14010	57890	15170	57740
0.175 s	-15640	58220	-12940	58220
0.17 -	12509	58449	15581	58900
0.18 s	-13077	58551	-10797	58430
	-6394	54977	1639	54893
0.17 -	-	-	18783	56755
0.18 s	-	-	-2190	58697
	-	-	-5554	55747
0.175 -	8473.4	57390	15172	57534
0.185 s	-9753.3	57087	-6396	56967
	-9686.6	60163	4893	59579
0.18 -	3686.5	57185	6174.2	57280
0.19 s	-5671.5	58615	-3546.3	58503
	-6623.3	52725	3670.8	52713
0.18 -	9586	56459	-	-
0.19 s	-3175	58238	-	-
	-12891	54819	-	-
0.185 -	2268.0	55191	9833	56070
0.195 s	- 9278.8	56118	-2655.3	52369
	-252.7	43363	-910.0	58363

Table 5: Calculated growth rates and frequencies for the inner mode.

The analysis of the linear model shows that the fixed point, which corresponds to a stationary plasma, is a saddle with one unstable direction and two stable directions. To compare the growth rates and their time dependence for each time window the average between the forward and backward growth rates has been calculated and the results are given in table 6 and figure 39. The growth rates of the three modes increase during the L-H transition and reach a maximum value between 0.17 and 0.18s. The growth rates of the outer and common mode slightly decrease afterwards but this effect could be due to measurement and rounding errors of the calculation. However the growth rate of the inner mode shows a significant drop in the ELMy H-mode phase that cannot be explained by measurement or rounding errors.

Time	Outer mode	Common mode	Inner mode
0.15 - 0.16 s	6285.5 ± 1441.8	4576.1 ± 1390.8	3758.5 ±1751.5
0.155 - 0.165 s	15159.5 ± 1019.5	9963.8 ± 1405.2	2725.8 ± 458.6
0.16 - 0.17 s	12419 ± 1266	8315.7 ± 1319.2	10057 ± 1126
0.165 - 0.175 s	17659.5 ± 877.5	9659.1 ± 801.0	14590 ± 580
0.17 - 0.18 s	21074 ± 951	10223 ± 1116	14045 ± 1359
0.175 - 0.185 s	20247 ± 957	7843.5 ± 931.5	11823 ± 3349
0.18 - 0.19 s	19388 ± 799	7318 ± 573	4930.4 ± 1243.9
0.185 - 0.195	20676 ± 147	8961 ± 750.2	6050.5 ± 3782

Table 6: Time dependence of the growth rates for the outer, the common and the inner mode.

These results seem to contradict the observations. Although the plasma becomes more stable in the H-mode, indicated by the increasing time between successive ELMs, the growth rates of the ELM precursors increase, which means that the instabilities become stronger. In general one would expect that the growth of the instabilities becomes smaller until they disappear and thus the plasma becomes stable by suppressing the instabilities. The contradiction becomes even more obvious when theories of the L-H transition are considered. Here the H-mode is considered as a stable fixed point which becomes unstable in ELMy H-mode. However the analysis of the data shows, that the H-mode is a saddle fixed point and apparently never stable throughout the discharge.

However, in the context of a saddle fixed point there exists a second mechanism that can stabilize the plasma, a homoclinic bifurcation. In a homoclinic bifurcation a periodic orbit moves towards a saddle fixed point and finally forms a homoclinic orbit, including the saddle. A homoclinic orbit is an orbit that starts and ends in the same fixed point. The plasma trajectory is then attracted by the homoclinic orbit and circles along the homoclinic orbit. The time between successive passings of the fixed points increases until it finally reaches infinity. Since the

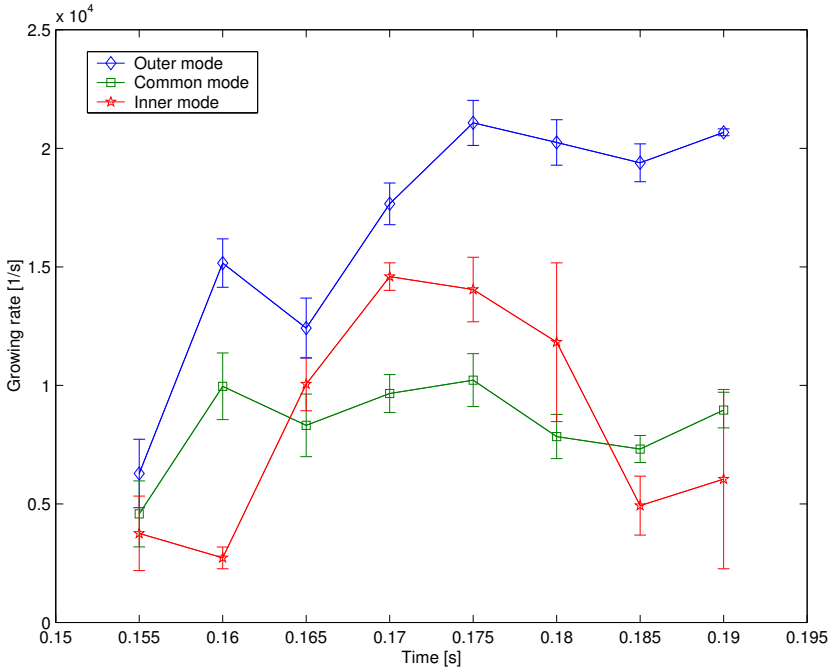

Figure 39: Time dependence of the growth rates

trajectory spends most of the time of each cycle near the fixed point the plasma becomes more and more stable. A similar explanation has been proposed for the stabilization of turbulence in the boundary layer of fluids [35], where the fluid velocity perpendicular to the boundary of the fluid shows a behavior similar to the radial plasma transport in ELMy H-mode. Figure 40 shows this mechanism.

Since near the fixed point the homoclinic orbit is asymptotic to the two planes spanned by the pair of eigenvectors whose eigenvalues have the smallest positive real part and the pair of eigenvalues with the least negative real part of all eigenvalues respectively, it is important to determine which of eigenvalues of the saddle has the dominant effect. If $\lambda_u < \lambda_s$ the trajectory near the saddle is drawn close to the planes before it escapes. Conversely, if $\lambda_u > \lambda_s$ the trajectory seems to escape "early" from the neighborhood of the saddle. In this sense one can speak of attracting or repelling planes since the trajectory seems to be bent towards or away from the planes near the saddle. However, one has to bear in mind that the planes are not real attractors and this picture is only valid locally. Whether the planes locally attract or repel trajectories depends on the saddle index which is the ratio $\frac{\lambda_s}{\lambda_u}$, where $-\lambda_s$ is the real part of the eigenvalue with the least negative real part and λ_u is the real part of the eigenvalue with the smallest positive real part. Since the dynamics of each of the four modes is more dominated by the eigenvalue with the smaller negative real part for λ_s the real part of this eigenvalue has been used. In addition we have to consider the

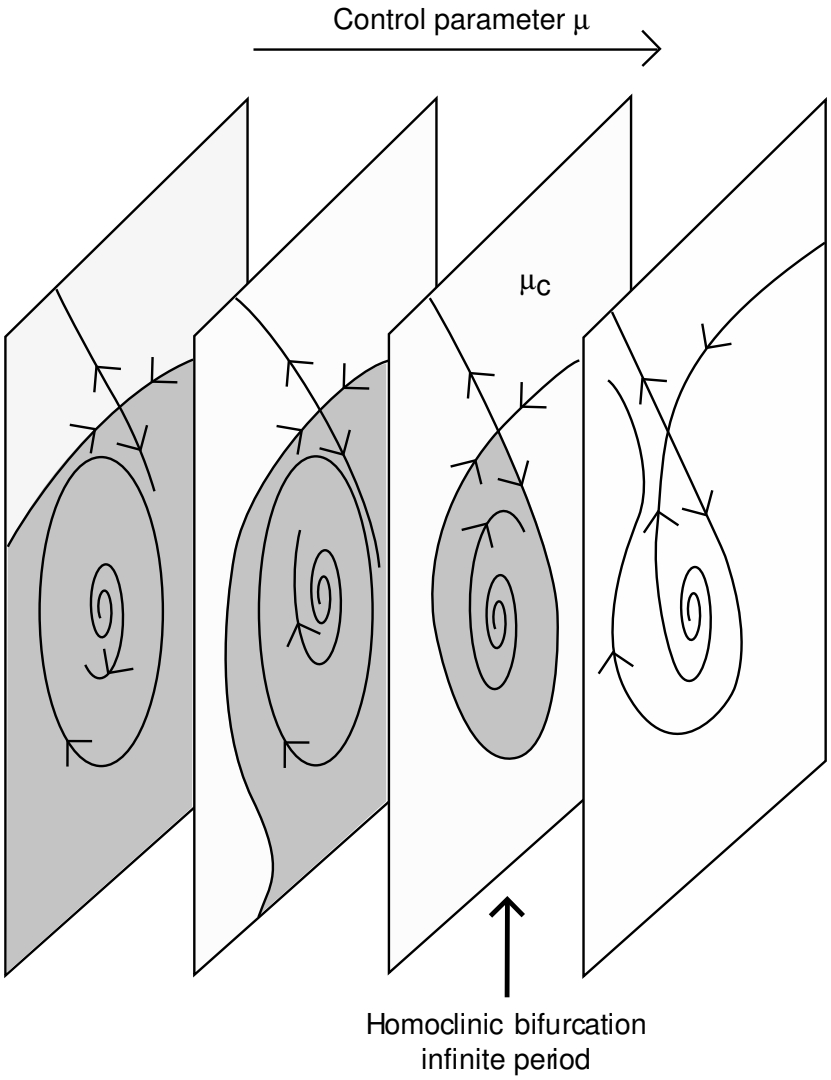

Figure 40: Limit cycle moving towards a saddle resulting in a homoclinic orbit. From reference [36].

interaction of the modes. Thus we have to take all eigenvalues into account and get only one saddle index and not an individual saddle index for each mode. The time dependence of the saddle index is shown in figure 41. During the transition from L- to H-mode the ratio $\frac{\lambda_s}{\lambda_u} < 1$ which indicates that the planes are repelling the trajectory. However the ratio increases during the transition and reaches values greater than or close to one in the H-mode. This behavior suggests the following model:

At the beginning of the transition the planes are repelling the trajectory and no homoclinic orbit exists. This is accompanied by instabilities and a high level of

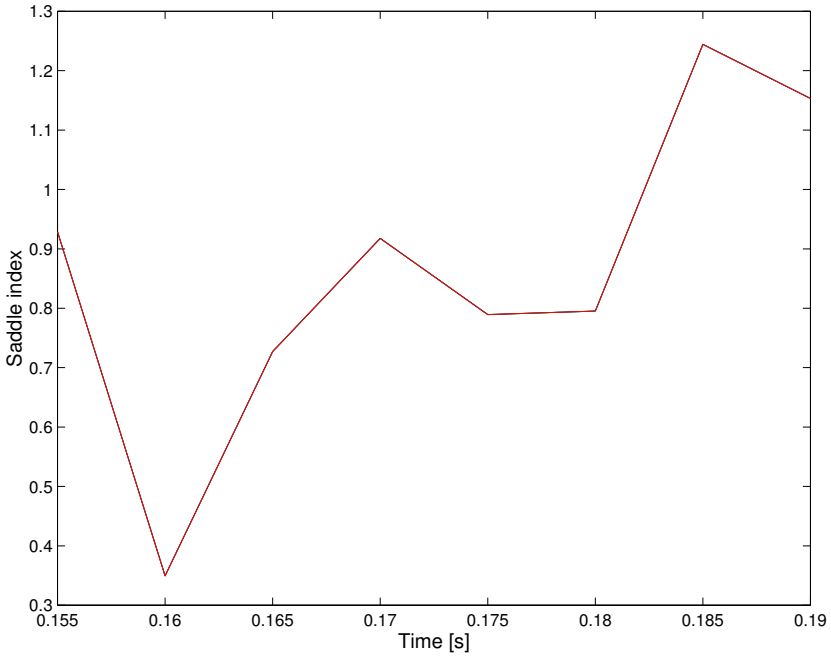

Figure 41: Time dependence of the saddle index $\frac{\lambda_s}{\lambda_u}$.

fluctuations. During the L-H transition the planes start to attract trajectories, reducing turbulence and stabilizing the plasma. This change of the saddle index strongly points towards an attracting periodic orbit, also called limit cycle, and a homoclinic bifurcation. However it cannot prove the existence of the orbit. A different approach to prove the existence of a limit cycle will be shown in the next section.

5.5 The existence of the limit cycle

Because of the sampling and noise problems mentioned earlier, the existence of the limit cycle cannot be proved for the whole 18 dimensional system (three modes with six eigenvalues each). However, if a limit cycle exists then one should be able to find a limit cycle for each individual mode. Thus the data is split up into the modes and each mode is investigated individually. Since the eigenvalues of the linear maps are complex we have to change our coordinate system into an extended polar coordinate system with three radii x, y, z and three angular frequencies θ_x, θ_y, θ_z for each mode. To simplify the later calculation the angular frequency of the modes is neglected and the analysis is restricted to the radii. Since in this case the limit cycle must be attracting the proof of its existence can be done in a very easy way. Consider a small rectangular neighborhood of length δ around the fixed point as shown in figure 42:

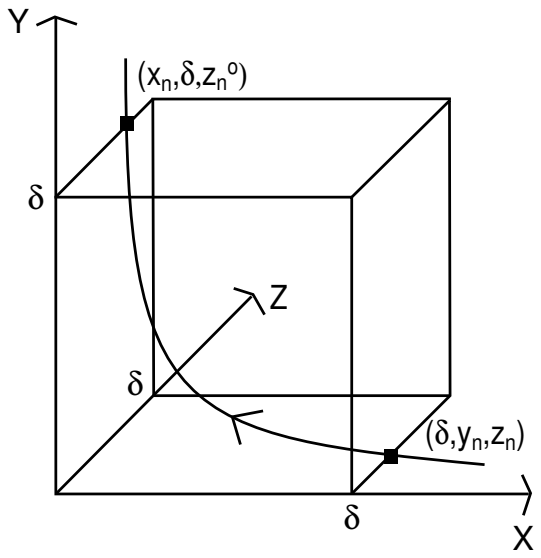

Figure 42: Trajectory passing by a saddle.

The trajectory enters the neighborhood at the point (δ, y_n, z_n) and leaves it at (x_n, δ, z_n^o). If a limit cycle exists the sequence $\{(y_n, z_n)\}$ converges to a limit point $\{(y_0, z_0)\}$. In order to prove the existence of the limit point the map $(y_{n+1}, z_{n+1})\} = F(y_n, z_n)$ has to be found. Actually this map is known since $(\delta, y_{n+1}, z_{n+1}) = \varphi_{t_n}(\delta, y_n, z_n)$, where φ_t is the flow of the plasma and t_n the time it takes to move from $(\delta, y_{n+1}, z_{n+1})$ to (δ, y_n, z_n). This map can be split up into two maps, one valid in the neighborhood of the fixed point and the other for flow outside the neighborhood. In the neighborhood of the fixed point the flow of the trajectory can be approximated with the linearized flow:

$$\delta = y_n e^{\lambda_u t_n} \tag{58}$$
$$x_n = \delta e^{-\lambda_s t_n} \tag{59}$$
$$z_n^o = z_n e^{\lambda_z t_n} \tag{60}$$

where $-\lambda_s < 0$ is the real part of the eigenvalue with the least negative real part, $\lambda_u > 0$ the real part of the eigenvalue with the smallest positive real part and λ_z the real part of the third eigenvalue. However since the following maps will be fitted to measured data, which means that it is noisy and the points of entrance and exit of the neighborhood are not always measured (but points very close to them), the equation has to be replaced by

$$y_n^o = y_n e^{\lambda_u t_n} \tag{61}$$
$$x_n = x_n^o e^{-\lambda_s t_n} \tag{62}$$
$$z_n^o = z_n e^{\lambda_z t_n} \tag{63}$$

where x_n^o and y_n^o are roughly δ. Eliminating t_n from equations (61)-(63) gives

$$x_n = x_n^o \left(\frac{y_n}{y_n^o}\right)^{\gamma_1} \tag{64}$$
$$z_n^o = z_n \left(\frac{y_n^o}{y_n}\right)^{\gamma_2} \tag{65}$$

where $\gamma_1 = \frac{\lambda_s}{\lambda_u}$ and $\gamma_2 = \frac{\lambda_z}{\lambda_u}$. The return map (flow leaving the δ-neighborhood and returning to it) can be expanded in a Taylor series, where all terms except for the linear term can be neglected. This gives

$$\begin{pmatrix} x_{n+1}^o \\ y_{n+1} \\ z_{n+1} \end{pmatrix} = \begin{pmatrix} \varphi_{x_0} \\ \varphi_{y_0} \\ \varphi_{z_0} \end{pmatrix} + \begin{pmatrix} \frac{d\varphi_x}{dx} & \frac{d\varphi_x}{dy} & \frac{d\varphi_x}{dz} & \frac{d\varphi_x}{dt} \\ \frac{d\varphi_y}{dx} & \frac{d\varphi_y}{dy} & \frac{d\varphi_y}{dz} & \frac{d\varphi_y}{dt} \\ \frac{d\varphi_z}{dx} & \frac{d\varphi_z}{dy} & \frac{d\varphi_z}{dz} & \frac{d\varphi_z}{dt} \end{pmatrix} \cdot \begin{pmatrix} x_n - x_0 \\ y_n^o - y_0 \\ z_n^o - z_0 \\ t_n - t_0 \end{pmatrix} \tag{66}$$

or to write it with a set of coefficients

$$\begin{pmatrix} x_{n+1}^o \\ y_{n+1} \\ z_{n+1} \end{pmatrix} = \begin{pmatrix} a_1 \\ a_2 \\ a_3 \end{pmatrix} + \begin{pmatrix} b_{11} & b_{12} & b_{13} & b_{14} \\ b_{21} & b_{22} & b_{23} & b_{24} \\ b_{31} & b_{32} & b_{33} & b_{34} \end{pmatrix} \cdot \begin{pmatrix} x_n \\ y_n^o \\ z_n^o \\ t_n \end{pmatrix} \tag{67}$$

The coefficients can be found by fitting equation (67) to the measured data. To perform this fit the measured data is separated into the modes and each mode is embedded using the method of delays. Afterwards the eigenvalues of the local linear model are calculated and the embedded data is projected onto the basis of the eigenvectors. As before the data is divided into succeeding periods of 0.1 seconds an for each period the calculations are performed. To check the validity of this linear approximation the original data for x_{n+1}^o, y_{n+1} and z_{n+1} has been compared with the values obtained by using the fitted linear map for the measured values of x_n, y_n^o, z_n^o and t_n. Figure 43 shows the comparison of the measured data and the corresponding values of the linear approximation of the flow. As can be seen, the measured data and the calculated values match very well, which justifies the use of the linear map.

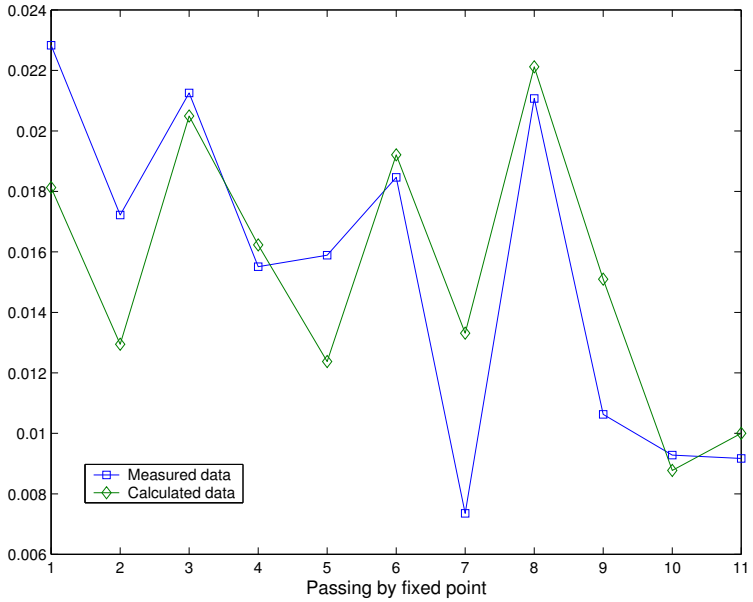

Figure 43: Comparison of the measured data with the calculated values using the estimated linear map for eleven passings of the fixed point. The comparison of the points show that the values agree quite well, which justifies the use of the linear approximation for the return map.

After finding the coefficients we can set $x^o_{n+1} = \delta$ and $y^o_n = \delta$ and eliminate t_n from equation (67) to obtain

$$\begin{pmatrix} y_{n+1} \\ z_{n+1} \end{pmatrix} = \begin{pmatrix} a_2 \\ a_3 \end{pmatrix} + \begin{pmatrix} b_{21} & b_{22} & b_{23} \\ b_{31} & b_{32} & b_{33} \end{pmatrix} \cdot \begin{pmatrix} x_n \\ \delta \\ z^o_n \end{pmatrix} + \\ + \frac{\delta - a_1 - b_{11}x_n - b_{12}\delta - b_{13}z^o_n}{b_{14}} \cdot \begin{pmatrix} b_{24} \\ b_{34} \end{pmatrix} \tag{68}$$

or in a more compact form

$$\begin{pmatrix} y_{n+1} \\ z_{n+1} \end{pmatrix} = \begin{pmatrix} c_2 \\ c_3 \end{pmatrix} + \begin{pmatrix} d_{21} & d_{22} \\ d_{31} & d_{32} \end{pmatrix} \cdot \begin{pmatrix} x_n \\ z^o_n \end{pmatrix} \tag{69}$$

Using equations (64) and (65) we get

$$\begin{pmatrix} y_{n+1} \\ z_{n+1} \end{pmatrix} = \begin{pmatrix} c_2 \\ c_3 \end{pmatrix} + \begin{pmatrix} e_{21} & e_{22} \\ e_{31} & e_{32} \end{pmatrix} \cdot \begin{pmatrix} y_n^{\gamma_1} \\ z_n \cdot y_n^{-\gamma_2} \end{pmatrix} \tag{70}$$

Equation (70) is nonlinear map which allows to calculate (y_{n+1}, z_{n+1}) if (y_n, z_n) is given. Thus if a limit cycle exists, equation (70) must have a fixed point and if this fixed point is attractive then the limit cycle is attractive. However it is difficult to analytically calculate the fixed point of the map and to determine if the fixed point is attractive or not. Since we are only interested in an attracting fixed point, we can find the fixed point - if it exists - easily by using equation (70) as a fixed point iteration. Several initial values of have been used for each period and equation (70) was applied several times to get the sequence (y_n, z_n). Table 7 shows an example of a converging fix point iteration for $(y_0, z_0) = (0.001, 0.03)$ and $\delta = 0.03$.

y_n	0.001	0.0045	0.0025	0.0030	0.0029	0.0029	0.0029	0.0029	...
z_n	0.030	0.0368	0.0317	0.0335	0.0330	0.0332	0.0331	0.0331	...

Table 7: The sequence (y_n, z_n) of the fixed point iteration for $(y_0, z_0) = (0.001, 0.03)$ and $\delta = 0.03$.

All calculations showed that the sequence was converging in every period for all initial values (y_0, z_0) to the same limit point. This shows that an attracting limit cycle exists throughout the transition, as indicated in the previous section. Since the behaviour of the axis corresponding to the eigenvectors of the local linear model changes from repelling to attracting, it indicates that the limit cycle moves and expands towards the axis forming a homoclinic bifurcation or a near homoclinic orbit. However it cannot be proved that this bifurcation takes place since the ELM-free period was not reached in the discharge.

Before proceeding further it is time to give a summary of the results of the last two sections. During and after the L-H transition a limit cycle exists and is attractive during the whole time and the trajectory of the plasma moves along the limit cycle. In this context the ELM precursors correspond to the period when the trajectory is close to the saddle. During the ELM the trajectory moves away from the saddle but returns along the limit cycle to the saddle. The period between successive ELMs is determined by the time it takes for the trajectory to move around the limit cycle. This period increases with time since the limit cycle expands and moves towards the axes. During one cycle the trajectory spends most of the time near the saddle. Finally when the homoclinic orbit is formed the period goes to infinity resulting in an ELM-free H-mode. Since it is not clear if the type III ELMs disappear or if only their repetition frequency becomes very small it is not possible to tell if a homoclinic orbit is formed or if the limit cycle comes very close to the saddle. Another possibility is that the limit cycle increases and comes close to the saddle to form an ELM-free period but decreased for higher heating powers leading to type I ELMs.

6 A short Story of Transition and ELM Models

As mentioned in section 2.2 a wide variety of different models exist, that try to explain the transition from the L- to the H-mode. The idea, that the electric field is the driving force for the transition was brought up very early in [37] however the mechanism for the creation of the fields was unknown. Early theories explained the transition with the ion loss mechanism [38, 39], but later experiments showed that the assumptions of these theories were not justified [40].

At the same time different models were developed. One group of these models [41, 42, 43, 44, 45, 46, 47, 48] uses turbulent processes and Reynolds stress as driving force for the transition. At the moment these models can better describe the phenomena involved in the L-H transition, in particular the generation of the shear flow and its turbulence suppression is treated self-consistently within the framework of such models. In the following we shall take a closer look at these models.

6.1 The physical model

The interesting thing about the turbulence-Reynolds-stress-models is the fact that basically all of them start from the same type of dissipative MHD equations. Although the instability involved in the L-H transition differs from model to model, they all show similar qualitative behaviour. Thus instead of treating the different models separately, their common behaviour will be discussed. To give a very general treatment of the physical model, the model given in [41] is discussed. In this paper the equations are given in a very explicit and in the most general form.

Since the main physics of the L-H transition is considered to happen in the plasma edge, the model focuses on the physics of the scrape off layer (SOL) outside the separatrix. For the notation of the equations, SOL-specific coordinates are taken (fig. 44). Here x measures the radial distance outwards from the separatrix, y the poloidal and z the toroidal distance. In most cases the divertor is neglected and the coordinate system is simplified to an annulus. The equations are

Continuity equation:

$$\partial_t \rho + \nabla \cdot (\rho \vec{u}) \tag{71}$$

Momentum balance equation:

$$\rho \partial_t \vec{u} + \rho(\vec{u} \cdot \nabla)\vec{u} = -\nabla p - \nabla \cdot \overleftrightarrow{\Pi} + \frac{1}{c}\vec{j} \times \vec{B} \tag{72}$$

Energy balance equation:

$$\partial_t p + \vec{u}\cdot\nabla p + \frac{5}{3}p\nabla\cdot\vec{u} = \frac{2}{3}\left(\frac{1}{en_e}\vec{j}\cdot\vec{R}^{ei} - \nabla\vec{q} - \overleftrightarrow{\Pi}\colon\nabla\cdot\vec{u}\right) \tag{73}$$

Generalized Ohm's law:

$$\vec{j} = \frac{1}{\eta}\left(\vec{E} + \frac{1}{c}\vec{u}\times\vec{B}\right) \tag{74}$$

where ρ is the plasma density, $\vec{u}$ is the velocity of the electrons, p the pressure, $\vec{B}$ the magnetic and $\vec{E}$ the electric field. The pressure tensor $\overleftrightarrow{\Pi}$ is of the form $\overleftrightarrow{\Pi} = -\left(\overleftrightarrow{\mu}_e + \overleftrightarrow{\mu}_i\right)\cdot\overleftrightarrow{\nu}$, where $\overleftrightarrow{\mu}$ is the viscosity tensor and $\nu_{ij} = \nabla_i u_j + \nabla_j u_i - \frac{2}{3}\delta_{ij}\nabla\cdot\vec{u}$. The heat flux is given by $\vec{q} = -\overleftrightarrow{\kappa}_e\cdot\nabla T_e - \overleftrightarrow{\kappa}_i\cdot\nabla T_i + T_e\overleftrightarrow{\alpha}\left[\vec{E} + (1/c)\vec{u}\times\vec{B}\right]$ where $\overleftrightarrow{\kappa}_{e,i}$ is the tensor for the heat conductivity, $T_{e,i}$ the electron and ion temperatures and $\overleftrightarrow{\alpha}$ the tensor of the thermoelectric coefficients. Finally η is the parallel (to the magnetic field) resistivity and $\vec{R}^{ei} = \eta e n_e\left[\vec{j} + \frac{3}{5}(e/T_e)\vec{q}^{\,e}\right]$ is the friction force.

To simplify the later analysis the pressure and the density are split up into an equilibrium part and an fluctuating part, i.e. $p = p_0 + \tilde{p}$ and $\rho = \rho_0 + \tilde{\rho}$. After some algebra and rescaling of the variables these four equations can be transformed into two final equations:

Vorticity equation

$$\partial_t\nabla_\perp^2\varphi + \left\{\varphi, \nabla_\perp^2\varphi\right\} = -\nabla_\parallel^2\varphi - \partial_y\tilde{p} + \nu\nabla_\perp^4\varphi \tag{75}$$

Pressure equation

$$\partial_t\tilde{p} + \{\varphi, \tilde{p}\} = -\partial_y\varphi + \chi\nabla_\perp^2\tilde{p} \tag{76}$$

where φ is the electrostatic potential, $\nabla_\perp^2 = \partial_x^2 + \partial_y^2$, $\nabla_\parallel = \partial_z - x\partial_y$, $\{\varphi, A\} = \partial_x\varphi\partial_y A - \partial_y\varphi\partial_x A$ (the Poisson bracket), $\nu = (\tilde{\nu}_\perp T/X^2)$, $\chi = (\tilde{\kappa}_\perp T/X^2)$, $T = \sqrt{\rho_0/2|p_0'|g_0}$, $X^2 = c^2\eta\sqrt{2|p_0'|g_0}L_s^2/B_0^2$, L_s the shear length and g_0 is the scalar curvature of the magnetic field.

Using these two equations gives rise to several problems. First of all it is not known, if these two equations are able to describe the plasma behaviour during the L-H transition and in ELMy H-mode. A point of criticism is the fact, that the pressure is split up into an equilibrium pressure and a fluctuating part. Since equation (76) describes the time evolution of the pressure fluctuations a description of the change of the equilibrium pressure p_0 during the transition is missing.

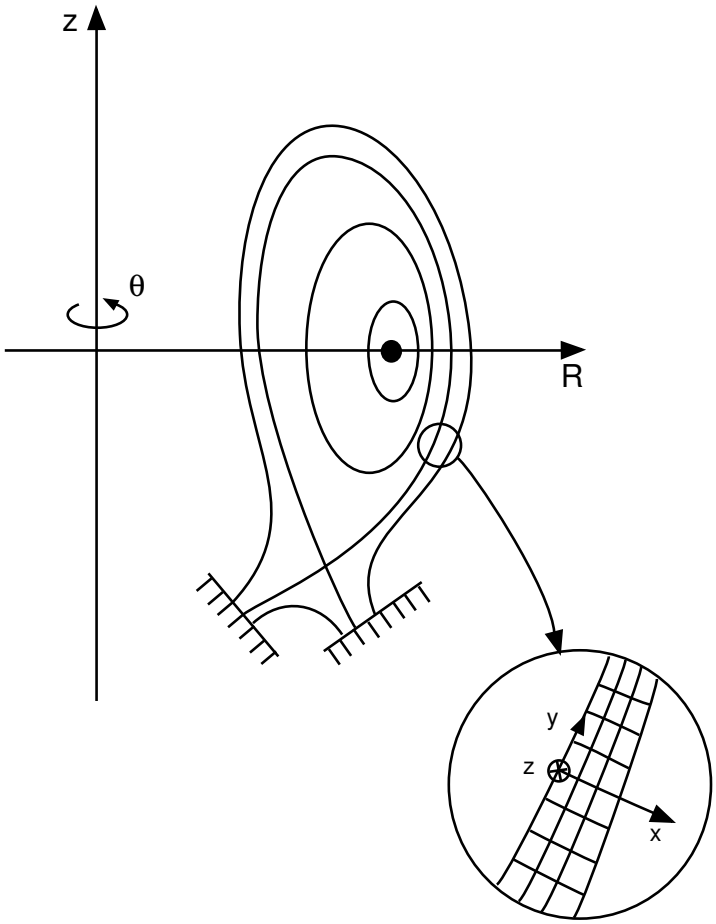

Figure 44: Typical tokamak geometry with separatrix, SOL and divertor. The SOL specific coordinate system used for the equations is magnified. From reference [42].

Furthermore the two coefficients χ and ν depend on the gradient of the equilibrium pressure p_0', however a relationship between the heating power and the pressure gradient is not included. A further problem is the fact, that the solutions of equations (75) and (76) are not known, which is a huge difficulty for the first mentioned problem, since the validity of the equations can only be proved by the comparison of their solutions with experimental data. Thus solving these partial differential equations is a key problem and has to be addressed numerically.

6.2 Numerical solutions

As mentioned before, the main interest of this section lies in the results of the numerical calculations rather than in the actual method of the numerical solu-

tion. Again, the solutions of the different models show qualitatively very similar properties. Thus only the results are summarized.

For the solution of the equations the z-direction is neglected and a two dimensional grid is used for the x- and y-direction, where $0 \leq x \leq L_x$ and $0 \leq y \leq L_y$. Earlier calculations showed that $\tilde{p}(0,y,t) = \tilde{p}(L_x,y,t) = 0$, $\varphi(0,y,t) = \varphi(L_x,y,t) = 0$ and $\nabla_\perp^2\varphi(0,y,t) = \nabla_\perp^2\varphi(L_x,y,t) = 0$ in the x-direction and $\tilde{p}(x,0,t) = \tilde{p}(x,L_y,t)$, $\varphi(x,0,t) = \varphi(x,L_y,t)$ and $\nabla_\perp^2\varphi(x,0,t) = \nabla_\perp^2\varphi(x,L_y,t)$ in the y-direction have to be used as boundary conditions. The coefficients ν and χ have been used as control parameters in the calculations. In the following the results of reference [41] are shown. Here two quantities are used to monitor the physical behaviour of the plasma:

the convective transport in the radial direction

$$< \tilde{p}v_x >:= -\frac{1}{L_xL_y}\int_0^{L_y} dy \int_0^{L_x} dx \tilde{p}\partial_y\varphi \tag{77}$$

and the strength of fluctuations

$$< v^2 >:= \frac{1}{L_xL_y}\int_0^{L_y} dy \int_0^{L_x} dx \left[(\partial_x\varphi)^2 + (\partial_y\varphi)^2\right] \tag{78}$$

For all calculations initial values for $\tilde{p}$ and φ have been used such that the plasma is in a state with almost zero monitor parameters, which corresponds to the start of a real discharge in an experiment. During each calculation χ and ν were constants and the calculations were stopped when the plasma reached a quasi steady state. For big values of χ both monitor quantities depart from their initial values exponentially but saturate after a certain time. This saturation corresponds to a plasma in stable L-mode. Figure 45 shows a typical example of this process.

Decreasing the control parameter χ changes the situation. The L-mode becomes unstable and the plasma moves to a new stationary state, the H-mode. Figure 46 shows this transition. The monitor parameters first saturate at a level which can be considered as an L-mode but finally move to a new state, the H-mode, with smaller values for the radial transport and the strength of the fluctuations. Although figure 46 shows a transition one has to bear in mind that the control parameter χ was constant during the whole calculation and the initial values correspond to a plasma at the beginning of a real discharge in experiments. Thus this calculation can be compared with a discharge, where an initially relative cold plasma is suddenly heated up to H-mode temperatures on a very short time scale, unlike in a real experiment, where the temperature changes on a longer time scale.

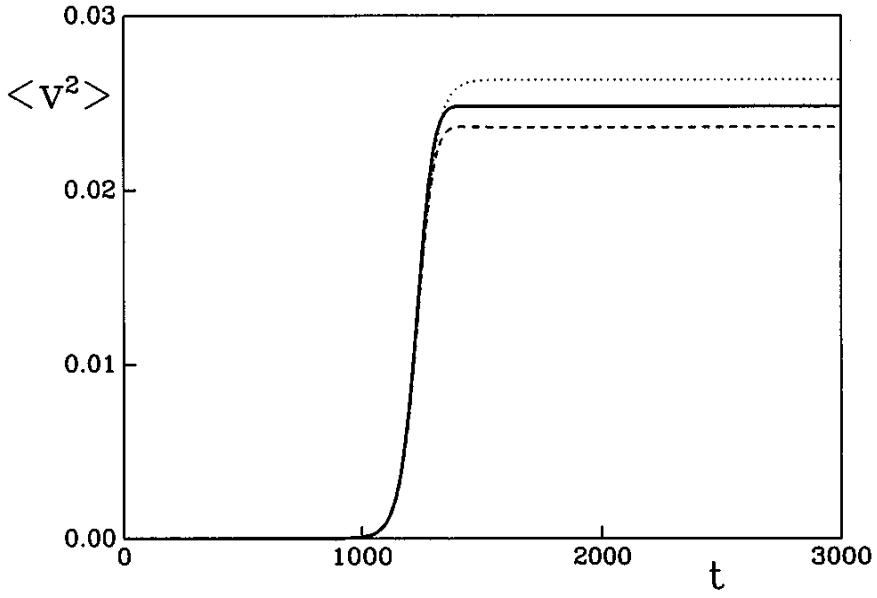

Figure 45: Strength of fluctuations $< v^2 >$ versus time t. After an exponential growth the fluctuations saturate. The solid line represents simulation results and the dotted line analytical results. The broken line shows the contribution from the $m = 1$ mode. From reference [41].

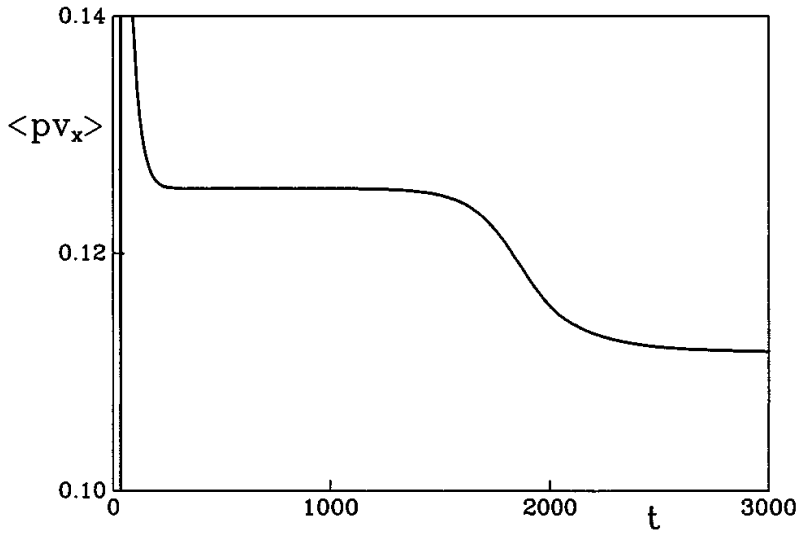

Figure 46: Convective radial transport $< pv_x >$ versus time t. First the plasma moves to the L-mode but finally bifurcates into the H-mode. From reference [41].

Further decrease in χ causes the H-mode to become unstable and a new oscillatory state develops. In most theories these oscillatory states are called ELMs, however [41] points out that these oscillations are different from ELMs. A significant difference between these oscillatory states and ELMs is that ELMs appear during the L-H transition and are not the result of an originally stable H-mode becoming unstable. In this point lies the biggest difference between the models. Except for [41] all models consider the L-H transition to happen in the following way:

For low heating powers only an stable L-mode exist. When a critical heating power is reached the L-mode becomes unstable and the plasma bifurcates to a new stable state, the H-mode. The ELMs appear when the heating power is further increased and the H-mode becomes unstable.

As mentioned in the last section this behaviour cannot be found in the data. In contrast to the theories the measurements indicate that the transition happens through the ELMy state. To solve this problem, in [41] an additional heating term

$$P_{ad} = (1-\alpha)\frac{1}{L_y}\int_0^{L_y} dy\{\varphi, \tilde{p}\} \quad , 0 \leq \alpha \leq 1 \tag{79}$$

is added to the right hand side of equation (76). This new term changes the situation dramatically. For large χ the plasma fluctuations saturate to the L-mode solution. Lowering χ causes the plasma to bifurcate to a stable H-mode, however this time the transition is accompanied by oscillations similar to dithering cycles. An even further decrease of χ results in a transition to an ELMy H-mode (see figure 47). Since the dependence of χ on the heating power, and thus the dependence of the ELM frequency on the heating power, is not known, the nature of the ELMs (type I or III) cannot be identified.

Again it should be noted that the transitions in these calculations are not real transitions as can be found in experiments where the control parameters are changing stepwise or gradually during the transition. In contrast to this a gradual increase of the control parameters can lead to very interesting results [42]. Figure 48 shows the dependence of the averaged particle flux Q at the boundary on the control parameter, here g_b. As g_b is increased the particles flux increases. Even when the critical value for the L-H transition is reached the particle flux increases further. The sudden decrease in the particle flux happens with the onset of an unstable H-Mode ($g_b \approx 5$). This behaviour gives rise to the question, what is the H-mode? While the theories consider the H-mode to be a stable solution of the plasma equations here the significant decrease of the particle flux happens when the so called H-mode solutions becomes unstable. Bearing this in mind it would make more sense to call the unstable H-mode solution the experimentally observed H-mode.

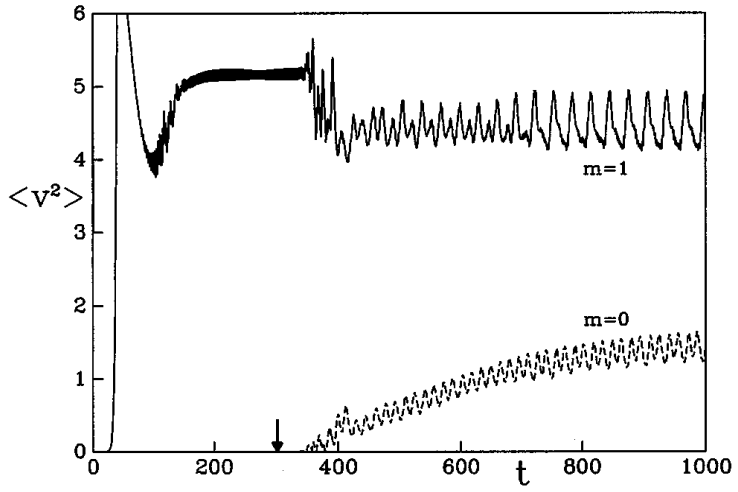

Figure 47: Strength of fluctuation $< v^2 >$ versus time t. The transition from the L-mode to an ELMy H-mode is accompanied by oscillations (dithering cycles). These oscillations develop into ELM-cycles. From reference [41].

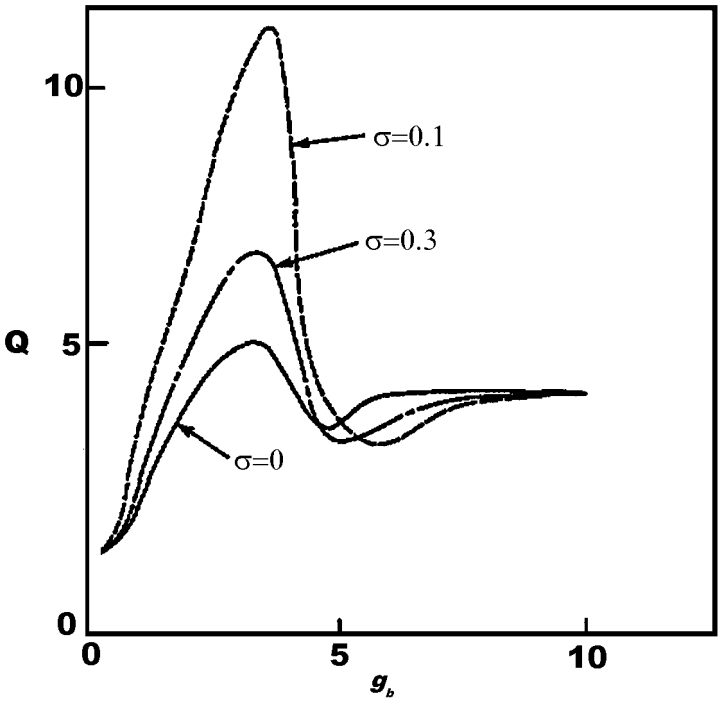

Figure 48: Dependence of time averaged particle flux at the boundary on the control parameter g_b and the conductivity σ. From reference [42].

Comparing the numerical results with experiments shows that equations (75) and (76) do not have the right transition characteristics, in particular dithering cycles and ELMs are missing. Adding a heating term gives results that are more consistent with the experimentally obtained picture. A big lack of all the theories is the missing relationship between the heating power and the used control parameters. Furthermore an equation for the time evolution of the equilibrium pressure gradient is missing.

Although the numerical calculations give some insight into the transition between the two confinement states, a qualitative and analytic understanding cannot be given. To tackle these problems low-dimensional models are derived from equations (75) and (76). These low-dimensional models can be divided into two classes, the first class, which will be discussed in the following section, uses expansions of orthogonal functions for the electrostatic potential φ and the pressure fluctuations $\tilde{p}$. The second class introduces new quantities and derives ordinary differential equations for these quantities from equations (75) and (76). The latter class will be discussed in the section 8.

7 Low-dimensional Models derived by Approximation of φ and $\tilde{p}$

For the approximation of the electrostatic potential φ and the pressure fluctuations $\tilde{p}$ several sets of orthogonal functions have been used. In the following an outline of the different approximations and, where possible, a discussion of the results will be given.

In [42, 43, 44] Galerkin approximations are used for φ and $\tilde{p}$. A Galerkin approximation is an expansion of φ and $\tilde{p}$ in a truncated series of basis functions like a Fourier series or a series of polynomials. This truncation corresponds to a projection of the dynamics onto a low-dimensional space and is called Galerkin projection. Since all approximations are special cases of [43] the results of this paper are represented. In [43] the z-direction is neglected and the following low-order mode approximation is chosen for Φ (which corresponds to φ in the last section) and p (here the ˜ is omitted):

$$\begin{aligned}\Phi(x,y,t) &= \Phi_0(t)sin(k_x x) + \Phi_1^s(t)sin(k_x x)sin(k_y y) \\ &\quad +\Phi_1^c(t)sin(k_x x)cos(k_y y) + \Phi_2^s(t)sin(2k_x x)sin(k_y y) \\ &\quad +\Phi_2^c(t)sin(2k_x x)cos(k_y y) \end{aligned} \tag{80}$$

$$\begin{aligned}p(x,y,t) &= p_0(t)sin(k_x x) + p_0'(t)sin(2k_x x) + p_1^s(t)sin(k_x x)sin(k_y y) \\ &\quad +p_1^c(t)sin(k_x x)cos(k_y y) + p_2^s(t)sin(2k_x x)sin(k_y y) \\ &\quad +p_2^c(t)sin(2k_x x)cos(k_y y) \end{aligned} \tag{81}$$

where $k_x = \frac{2\pi}{L_x}$ and $k_y = \frac{2\pi}{L_y}$. Substituting (80) and (81) into (75) and (76) gives a set of eleven ordinary first order differential equations. In this model the effective Rayleigh number $Ra^{eff} \propto \frac{1}{\chi\nu}$ is used as control parameter. In addition the parameters are chosen in such a way that the primary harmonic mode (Φ_1^{sc}, p_1^{sc}) is linearly destabilized and the secondary harmonic mode (Φ_2^{sc}, p_2^{sc}) is linearly stable. Increasing the effective Rayleigh number gives the following picture:

For small values of Ra^{eff} the subset of the modes (Φ_0, p_0, Φ_2^{sc}, p_2^{sc}) decays for any set of initial values to zero and thus the dynamics is restricted to a 5 dimensional subspace, spanned by (p_0', Φ_1^{sc}, p_1^{sc}). The modes are attracted by a limit cycle instead of a fixed point. This corresponds with the L-mode, as shown in figure 49 (a). On this limit cycle the amplitudes $\Phi_1^2 = (|\Phi_1^s|^2 + |\Phi_1^c|^2)$ and $p_1^2 = (|p_1^s|^2 + |p_1^c|^2)$ are constant and their projection onto the Φ_1^s-Φ_1^c-plane shows a nearly circular motion. This circular motion can be interpreted as a wave travelling through

the plasma in the y-direction (poloidal direction). If Ra^{eff} is increased beyond a critical value, a bifurcation takes place. Now the secondary modes are destabilized and the whole system settles down on a new limit cycle, the H-mode. On this new limit cycle all modes are excited but the fluctuation amplitude is smaller than in the L-mode. Figure 49 (b) shows the evolution of the plasma from the L-mode to the H-mode. For higher values of Ra^{eff} a second bifurcation takes place. Now the H-mode limit cycle is no longer stable and a new limit cycle appears on which Φ_0 and Φ_1 show an oscillatory behaviour (see figure 49 (c)). In [43] these oscillations are considered as ELMs.

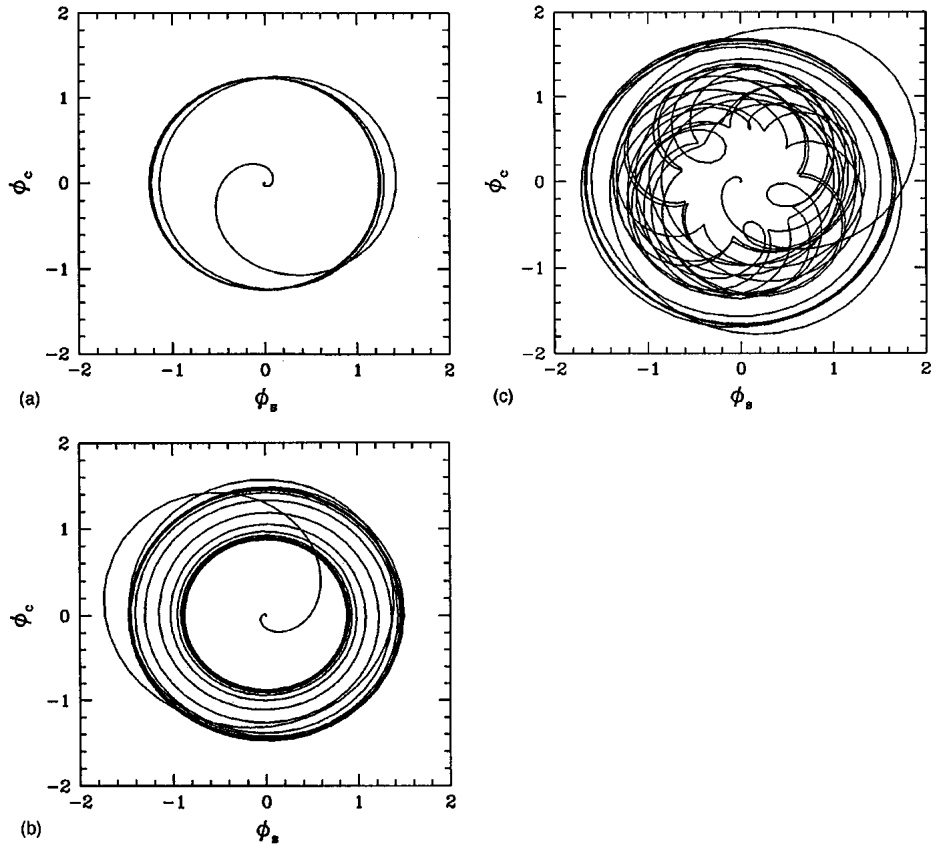

Figure 49: Projection of the phase space trajectory on the Φ_1^s-Φ_1^c-plane for the (a) L-mode limit cycle, (b) the L-H transition and (c) the ELMy H-mode. From reference [43].

According to [43] the repetition frequency of the ELMs first decreases with increasing Rayleigh number but increases with increasing Rayleigh number for higher values of Ra^{eff}. Since the Rayleigh number is proportional to the heating power we have first type III ELMs and for higher heating powers type I ELMs.

However although the observed oscillations are called ELMs they do not show the characteristics of experimental ELMs. Their phase space trajectory shows almost regular oscillations and not the pulse-like behaviour of the ELMs observed in experiments and numerical calculations. A reason for this difference could be the choice of the Galerkin approximation which is actually a truncated Fourier expansion for the y- and x-direction. Because of this the system of ordinary differential equations is very symmetric giving rise to the almost circular limit cycles.

Several other methods have been used for the approximation of φ and p. [41] for example uses Fourier expansion for the y- and z-direction and numerically calculated eigenfunctions for the x-direction. Although these approximations are more sophisticated, a better description of the plasma dynamics cannot be obtained. All these models show the same behaviour: with increasing control parameter a first stable L-mode becomes unstable and a stable H-mode develops. This H-mode becomes unstable for higher values of the control parameter. This coincides with the onset of oscillations, which are considered as ELMs in the models. However as mentioned above these ELMs are nearly regular oscillations and do not show the pulse-like behaviour of experimental ELMs. Thus these methods are only able to show the basic properties of the transition from a stable L-mode to a stable H-mode and the onset of the ELMs, but they are not able to reproduce the experimental observations in detail. In particular the slow transitions suggest that the L-H transition takes place via the ELMy state rather than the direct transition between two stable solution, as suggested by these models. A further striking point is, that in [42, 43] special heating terms are added to the ordinary differential equations. Again, this highlights the fundamental question as to whether equations (75) and (76) are sufficient to describe the physics of the L-H transition and the ELMy H-mode.

8 The Sugama and Horton Model

In contrast to the class of low-dimensional models discussed above, there is a second class of low-dimensional models which uses a different approach to tackle in part these problems. Three different 3-dimensional models of this type have appeared in the literature [42, 46, 47]. An interesting property of these models is the fact, that they are almost identical if the pressure gradient is constant. In the following the model of Sugama and Horton [46] will be discussed since it is the most promising candidate of the three. In earlier work [45] Sugama and Horton showed that resistive g-modes can generate Reynolds stress, which on the other hand enhances the generation of shear flow. Instead of using equations (75) and (76) and using approximations for φ and p, in their model new quantities are introduced:

Turbulent kinetic energy

$$K := \frac{1}{\delta}\int_{-\delta}^{0} dx \frac{1}{2}\left\langle \tilde{v}^2 \right\rangle \tag{82}$$

Background shear flow kinetic energy

$$F := \frac{1}{\delta}\int_{-\delta}^{0} dx \frac{1}{2} v_0^2 \tag{83}$$

and the potential energy related to the pressure profile

$$U := \frac{1}{\delta}\int_{-\delta}^{0} dx \frac{(-x)}{L_c}\frac{p_0}{n_0 m_i} \tag{84}$$

where $x = 0$ corresponds to the plasma surface (last closed flux surface) and δ represents the radial length of the shear flow layer. The angle bracket $< \cdot >$ denotes the average over a magnetic flux surface (y-z-plane). As before the velocity and the pressure are split up into an x-dependent average part and a fluctuating part $v = v_0(x) + \tilde{v}$ and $p = p_0(x) + \tilde{p}$; in the following the index 0 denotes the average values. $n_0 m_i$ is the average mass density, where n_0 is the average density and m_i is the mass of the ions. The unfavorable average magnetic curvature is represented by $1/L_c$. Using equations (75) and (76) in a simplified form the following energy balance equations can be obtained:

$$\frac{dU}{dt} = P_U - P_K \tag{85}$$
$$\frac{dK}{dt} = P_K - P_F - \epsilon_K \tag{86}$$
$$\frac{dF}{dt} = P_F - \epsilon_F \tag{87}$$

where the terms on the right hand side are given by

$$P_U = \frac{\langle \tilde{p}\tilde{v}_x \rangle \,|_{x=-\delta}}{L_c n_0 m_i} \tag{88}$$
$$P_K = \frac{1}{\delta}\int_{-\delta}^{0} dx \frac{\langle \tilde{p}\tilde{v}_x \rangle}{L_c n_0 m_i} \tag{89}$$
$$P_F = \frac{1}{\delta}\int_{-\delta}^{0} dx \, \langle \tilde{v}_x \tilde{v}_y \rangle \, \frac{dv_0}{dx} \tag{90}$$
$$\epsilon_K = \frac{1}{\delta}\int_{-\delta}^{0} dx \left\{ \mu \left\langle \left(\frac{\partial \tilde{v}_i}{\partial x_j} \right)^2 \right\rangle + \frac{\eta}{n_0 m_i} \left\langle \tilde{J}_\parallel^2 \right\rangle \right\} \tag{91}$$
$$\epsilon_F = \frac{1}{\delta}\int_{-\delta}^{0} dx \mu \left(\frac{dv_0}{dx} \right)^2 \tag{92}$$

here μ is the (kinematic) viscosity, η the resistivity and $\tilde{J}_\parallel = -\eta^{-1}\nabla_\parallel \Phi$ the parallel current. Φ is the electrostatic potential and the velocity is given by $v = -\frac{c}{B_0}\nabla\Phi \times \hat{z}$. The terms on the right hand side of equations (85)-(87) can be separated into two classes. The first class, consisting of P_K and P_F describes the exchange of energy between the quantities U, K and F. The second class, consisting of P_U, ϵ_K and ϵ_F, deal with the interaction with the core plasma and dissipative effects. P_U is the production of potential energy caused by the energy input from the plasma core. ϵ_K stands for the viscous and Joule dissipations of the fluctuations and ϵ_F for the viscous dissipation of the average flow. Adding equations (85)-(87) gives a differential equations for the total energy of the system

$$\frac{d}{dt}(U + K + F) = P_U - \epsilon_K - \epsilon_F \tag{93}$$

Equation (93) shows that the heating term is needed to maintain or increase the total energy of the system and without it, the total energy would decay to zero. To solve equations (85)-(87) we have to express the terms on the right hand side

in terms of U, K and F. Assuming a linear profile for the averaged pressure of the form

$$p_0(x) \cong p_0(x=0) + \frac{dp_0}{dx}x \tag{94}$$

we get for U

$$U \cong \frac{1}{3}\frac{\delta^2}{L_c n_0 m_i}\left|\frac{dp_0}{dx}\right| + \frac{1}{2}\frac{\delta p_0(x=0)}{L_c n_0 m_i} \tag{95}$$

here $dp_0/dx \leq 0$ and $n_0 \cong const$ are assumed. Assuming further that $p_0(x = 0) = const$ we can redefine the pressure gradient as

$$U \equiv \frac{1}{3}\frac{\delta^2}{L_c n_0 m_i}\left|\frac{dp_0}{dx}\right| \tag{96}$$

It turns out that most of the terms (88)-(92) depend on the time scale τ_c in the g mode turbulence which is given by

$$\tau_c \sim \sqrt{\frac{L_c n_0 m_i}{|dp_0/dx|}} \tag{97}$$

Using (96) we get

$$\tau_c \sim \delta\sqrt{U} \tag{98}$$

Thus for the terms the following estimates can be derived

$$P_K \sim \tau_c^{-1} K \sim \delta^{-1} U^{1/2} K \tag{99}$$

$$P_F \sim \tau_c K\left(\frac{dv_0}{dx}\right) \sim \delta^{-1} U^{-1/2} F K \tag{100}$$

$$\epsilon_K \sim D_L^{-1} K^2 \tag{101}$$

$$\epsilon_F \sim \mu\delta^{-2} F \tag{102}$$

where $D_L = D_L(U)$, the L-mode anomalous diffusivity, and $\mu = \mu(U)$ are both functions of U. By estimating the terms above new physics comes into the equations that is not contained in the original PDEs (75) and (76). Finally a closed set of equations for U, K and F can be obtained

$$\frac{dU}{dt} = P_U - C_K\delta^{-1}U^{1/2}K \tag{103}$$
$$\frac{dK}{dt} = C_K\delta^{-1}U^{1/2}K - C_F\delta^{-1}U^{-1/2}FK - C'_K D_L^{-1}K^2 \tag{104}$$
$$\frac{dF}{dt} = C_F\delta^{-1}U^{-1/2}FK - C'_F\delta^{-2}\mu F \tag{105}$$

where the C's are constants and $P_U(>0)$ is regarded as an external parameter. The stationary solutions of (103)-(105) can easily be found and they give some interesting results:

For the L-mode solution we get

$$U = U_L \tag{106}$$
$$K = \delta^{-1}C_K C'^{-1}_K D_L(U_L)U_L^{1/2} \tag{107}$$
$$F = 0 \tag{108}$$

where U_L is given by the solution of

$$D_L(U_L)U_L = C'_K C_K^{-2}\delta^2 P_U \tag{109}$$

Equation (109) shows that the L-mode solution is strongly dependent on $D_L(U)$ which causes some problems since the exact functional form of $D_L(U)$ is not known. However simulations [49] and scaling theory [50] showed that $D_L(U)$ is proportional to the pressure gradient and thus to U_L. In the following it is assumed for simplicity that $D_L(U) = C_D U$. Thus we get

$$U_L = \sqrt{C_D^{-1}C'_K C_K^{-2}\delta^2 P_U} \tag{110}$$

The L-mode solution is characterized by the lack of a shear flow. In addition, both the average pressure gradient and the turbulent energy increase with increasing heating power. A second stationary solution, the H-mode solution, is given by

$$U = U_H \tag{111}$$
$$K = \delta^{-1}C_F^{-1}C'_F\mu(U_H)U_H^{1/2} \tag{112}$$
$$F = C'_K C_F^{-1}U_H D_L^{-1}(U_H)[C_K C'^{-1}_K D_L(U_H) - C_F^{-1}C'_F\mu(U_H)] \tag{113}$$

Since F is an kinetic energy and thus has to be positive the H-mode solution only exists, when the anomalous diffusivity exceeds the viscosity, or to be more precise when

$$C_K C'^{-1}_K D_L(U_H) \geq C_F^{-1} C'_F \mu(U_H) \tag{114}$$

Essentially this requires that the edge ion temperature is sufficiently high. Again U_H is a function P_U and given by the solution of

$$\mu(U_H) U_H = C'^{-1}_F C_F C_K^{-1} \delta^2 P_U \tag{115}$$

As before the functional form of $\mu(U)$ is not known. For the high pressure gradient limit we get $\mu(U) \sim U$. For small pressure gradients two cases have to be distinguished: in the banana regime (case A) $\mu(U) \sim U^{-3/2}$ and in the transitional regime (case B) $\mu(U) \sim U^{-1}$ is valid. Putting these two limits together in a simple way we get

for case A

$$\mu(U) = U^{-3/2}(c_{A1} + c_{A2} U^{5/2}) \tag{116}$$

and for case B

$$\mu(U) = U^{-1}(c_{B1} + c_{B2} U^2) \tag{117}$$

Before splitting up the analysis into the two cases let's have a look at the common properties. For the H-mode solution the shear flow kinetic energy is not zero, which means that a shear flow develops as observed in experiments. The pressure gradient of the H-mode solution U_H is bigger than the one of the L-mode solution U_L and the turbulence level K is smaller for the H-mode solution. Thus the H-mode solution shows the properties of the experimentally observed H-mode.

The transition from L- to H-mode happens when

$$C_K^{-1} \delta^2 P_{c1} = C_K C'^{-1}_K U_{c1} D_L(U_{c1}) = C_F^{-1} C'_F U_{c1} \mu(U_{c1}) \tag{118}$$

For both cases only one solution of (118) exists. Before proceeding further it is convenient to introduce the following normalized variables:

$$\begin{gathered} u = U/U_{c1} \qquad k = K/U_{c1} \qquad f = F/U_{c1} \qquad \tau = C_K \delta^{-1} U_{c1}^{1/2} t \\ d(u) = C_K C'^{-1}_K \delta^{-1} U_{c1}^{-1/2} D_L(U) \qquad m(u) = C_F^{-1} C'_F \delta^{-1} U_{c1}^{-1/2} \mu(U) \\ q = C_K^{-1} \delta U_{c1}^{-3/2} P_U \qquad c = C_F/C_U \end{gathered} \tag{119}$$

Thus equations (103)-(105) can be rewritten as

$$\begin{aligned} \frac{du}{d\tau} &= q - u^{1/2}k && (120)\\ \frac{dk}{d\tau} &= u^{1/2}k - cu^{-1/2}fk - d^{-1}(u)k^2 && (121)\\ \frac{df}{d\tau} &= cu^{-1/2}fk - cm(u)f && (122) \end{aligned}$$

with

$$\begin{aligned} d(u) &= u\\ m(u) &= u^{-3/2}(0.95 + 0.05u^{5/2})\\ \text{or } m(u) &= u^{-1}(0.97 + 0.03u^2) \end{aligned}$$

The stationary solutions are now given by (u_L, k_L, f_L) and (u_H, k_H, f_H) where

$$\begin{aligned} k_L &= u_L^{1/2}d(u_L) \qquad f_L = 0 && (123)\\ k_H &= u_H^{1/2}m(u_H) \qquad f_H = c^{-1}u_H d^{-1}(u_H)(d(u_H) - m(u_H)) && (124) \end{aligned}$$

where u_L and u_H depend on the external heating q via

$$u_L d(u_L) = u_H m(u_H) = q \tag{125}$$

the critical condition for the existence of the H-mode now reads as

$$d(u_H) \geq m(u_H) \tag{126}$$

and the critical heating for the transition is given by

$$u_{c1}d(u_{c1}) = u_{c1}m(u_{c1}) = q_{c1} \tag{127}$$

Now let's have a closer look at the two cases. For case A three critical heating powers exist: q_{c1}, q_{c2} and q_{c3}. For $q < q_{c2}$ only one stationary solution exists, the L-mode solution. To determine the stability of the L-mode solution we linearize equations (120)-(122) around (u_L, k_L, f_L). The eigenvalues of the linearized map are given by

$$\lambda_{L1} = c(d_L - m_L) \qquad \lambda_{L+} \qquad \lambda_{L-} \tag{128}$$

where $\lambda_{L\pm}$ are the solutions of

$$\lambda^2 + \left(\frac{1}{2}d_L + u_L^{1/2}\right)\lambda + u_L^{1/2}\left(u_L d_L\right)' = 0 \tag{129}$$

here $d_L = d(u_L)$ and $m_L = m(u_L)$. $'$ denotes the derivative with respect to u. Since both u_L and d_L are positive we get $Re(\lambda_\pm) < 0$. Thus the L-mode solution is unstable if and only if $d_L > m_L$. From equation (127) we see that the instability criterion for the L-mode solution coincides with the transition from L- to H-mode.

Thus for $q_{c2} < q < q_{c1}$ the L-mode solution remains stable. However two stationary H-mode solutions H_- and H_+ appear. Both have non-vanishing shear flow energy and a higher pressure gradient and smaller turbulent energy than the L-mode solution. The eigenvalues of the linearized flow around the H-mode solutions are given by the solution of

$$\lambda^3 + A\lambda^2 + B\lambda + C = 0 \tag{130}$$

where

$$\begin{aligned} A &= m_H\left(\frac{1}{2} + \frac{u_H^{1/2}}{d_H}\right) \\ B &= u_H^{1/2} m_H\left[(1+c)\left(1 - \frac{m_H}{d_H}\right) + \frac{m_H\left(u_H d_H\right)'}{d_H^2}\right] \\ C &= c u_H^{1/2} m_H\left(u_H m_H\right)'\left(1 - \frac{m_H}{d_H}\right) \end{aligned} \tag{131}$$

where $m_H = m(u_H)$ and $d_H = d(u_H)$. Since only the case in which the H-mode solution exists is considered we have $d_H > m_H$ and thus A and B are positive. For the H-mode solution H_- we have $C < 0$ and thus H_- is unstable since equation (130) has one real and positive solution in this case. For the other H-mode solution H_+ one eigenvalue is real and negative since now $C > 0$. The other two eigenvalues are either both real and negative or form a pair of complex conjugate values. H_+ becomes unstable when $C > AB$ or more explicit

$$\frac{\left(u_H m_H\right)'}{m_H} > \left(1 + c^{-1} + c^{-1}\frac{m_H/d_H}{1 - m_H/d_H}\frac{\left(u_H d_H\right)'}{d_H}\right)\left(\frac{1}{2} + \frac{u_H 1/2}{d_H}\right) \tag{132}$$

this criterion is fulfilled, when $q > q_{c3}$. Thus for $q < q_{c3}$ the H-mode solution H_+ is stable. Figure 50 shows position of the L- and H-mode solutions in the u-q-plane, where the stable solutions are indicated by a solid line and the unstable ones by a dotted line respectively.

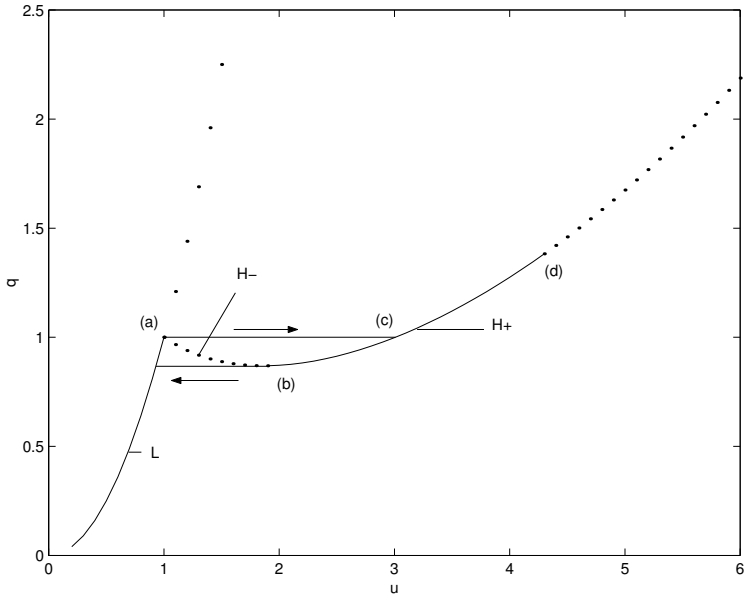

Figure 50: Stationary solutions in the u-q-plane. The forward transition happens between the points (a) and (c) and is indicated by an arrow. At point (d) the H-mode solution becomes unstable and limit cycles appear. The stability of the L- and H-mode solutions are indicated by dotted (unstable) and solid (stable) lines. The backward transition happens at point (b) and is indicated by an arrow.

The existence of two stable solutions for $q_{c2} < q < q_{c1}$ could offer an explanation for the dithering cycles. If we take into account that this three dimensional model is most probably a simplification of a higher dimensional model and that in a real plasma there are always small fluctuations then the dithering cycles could be movements of the plasma between these two stationary solutions. As the heating power increases, the L-mode solution becomes unstable and the plasma finally moves to the H-mode solution. Additionally the existence of the two stable fixed points offers an explanation for the hysteresis observed in many experiments. When the plasma is heated up it stays in L-mode until $q = q_{c1}$ is reached, when the forward transition to the H-mode happens (indicated by the right arrow in figure 50). However when the H-mode plasma is cooled down (as it is the case at the end of the discharge) the plasma stays in H-mode until $q < q_{c2}$, before it moves to the L-mode (indicated by the left arrow in figure 50). Since $q_{c2} \neq q_{c1}$ the forward and backward transitions happen at different heating powers. For $q_{c1} < q < q_{c3}$ only the H-mode solution H_+ is stable and the plasma is in H-mode. For $q > q_{c3}$ H_+ becomes an unstable focus and a limit cycle is formed.

In case B the situation changes slightly, the main difference arises from the fact

that only one H-mode solution exists instead of two. For $q < q_{c1}$ only one stationary solution exists, the L-mode solution. Since the eigenvalues of the L-mode solution are identical with the one in case A this solution is stable. At the critical heating power q_{c1} the L-mode solution becomes unstable and a new stable stationary solutions appears, the H-mode solution. Note that in this case no hysteresis can be found since only one H-mode solution occurs. Finally the H-mode solution becomes unstable for $q > q_{c3}$ and a stable limit cycle forms. Figure 51 shows this behaviour in the u-q-plane.

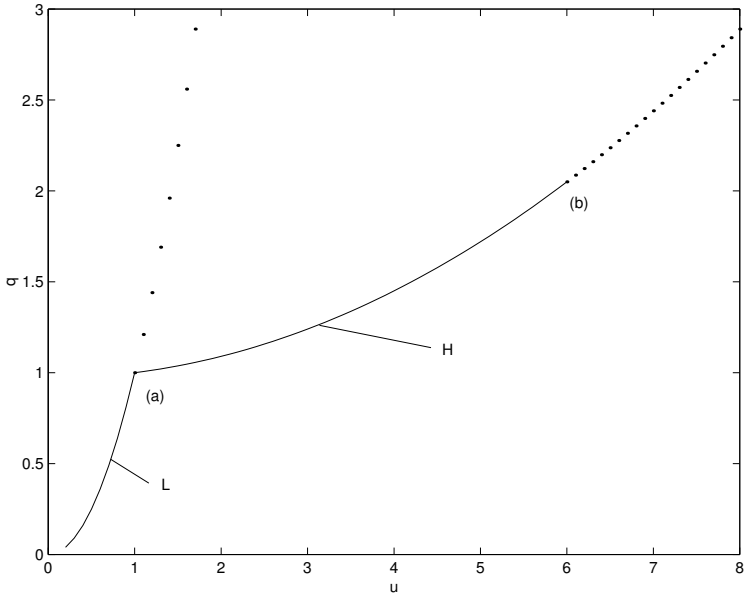

Figure 51: The stationary solutions for case B. At point (a) the transition from L- to H-mode happens. The H-mode solution becomes unstable at point (b) and limit cycles appear.

So far we get the following picture for both cases: a stable L-mode solution becomes unstable and at the same time a stable H-mode solution appears. This H-mode solution becomes unstable for higher heating powers and a stable limit cycle is formed. Except for the explanation of the hysteresis this picture is more or less the same as for all other methods presented in the last section and it seems that the Sugama and Horton model does not improve the picture. However the transition and the stable limit cycle show very interesting properties. In order to model the transition a stepwise increasing and continuous heating power q was used for the solutions of equations (120)-(122). Figure 52 shows the time evolution of the heating power q, the pressure gradient u, turbulent kinetic energy k and the shear flow energy f for case A. The time evolution for case B is qualitatively the same, only the hysteresis is missing.

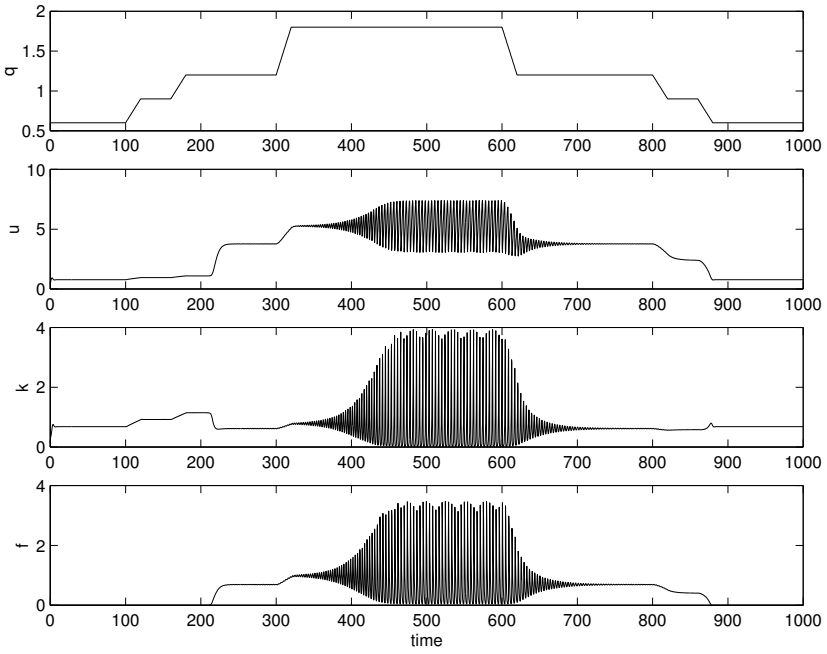

Figure 52: Time evolution of the of the heating power q, the pressure gradient u, turbulent kinetic energy k and the shear flow energy f.

After the second increase of heating power at $t = 180s$ the L-H transition happens between $t = 210s$ and $t = 230s$. It is noteworthy that the transition does not coincide with the increase of the heating powers. The discrepancy can be explained by the fact that the L-mode solution is still stable in two directions and thus the plasma trajectory is attracted by this solution for a certain time. Although H_+ is a stable focus the plasma trajectory does not settle down to this solution. In contrast it circulates around the solution and clear oscillations can be found for u, k and f. The reason for this is that the contraction onto H_+ is very weak and the time to settle down on H_+ is longer than the time between the heating steps. Figure 53 shows the time evolution of u, k and f for $t = 230-275s$.

After the third increase of the heating power at $t = 300s$ a limit cycle appears. Its size increases with increasing heating power until the limit cycle approaches the planes defined by $k = 0$ and $f = 0$. At the same time the period of the limit cycle increases. Figure 54 shows numerical simulations of equations (120)-(122) for $q > q_{c3}$ (which is fulfilled for $t > 300s$). The turbulent energy and the shear flow energy show pulse-like relaxation oscillations like ELMs in experiments. Most of the time of one cycle k and f spend near their zero values, which has the appearance of a quasi-stable plasma. The pressure gradient shows a sawtooth-like behaviour that looks very similar to the measured data, used for the investigation.

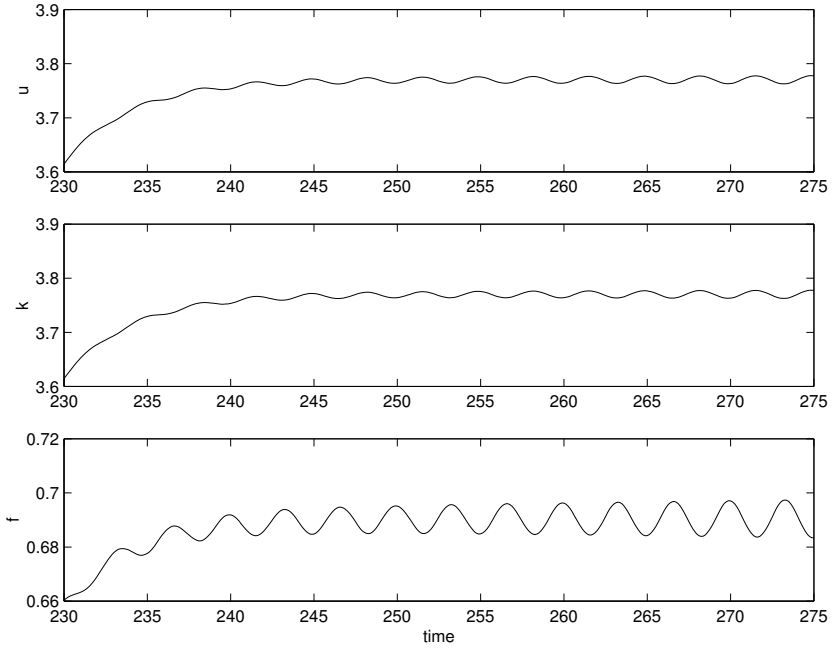

Figure 53: Time evolution of the of the pressure gradient u, turbulent kinetic energy k and the shear flow energy f for $t = 230 - 275s$.

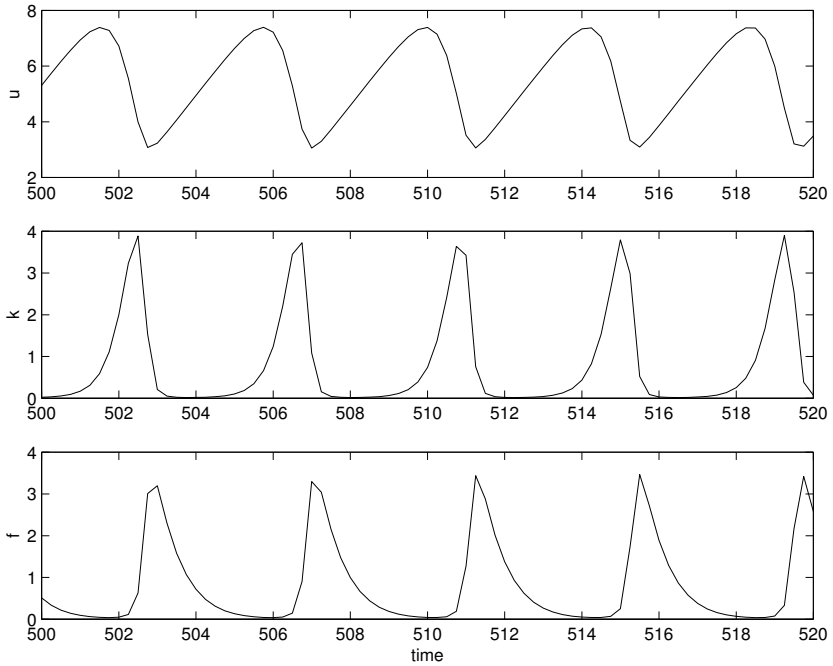

Figure 54: Time evolution of the of the pressure gradient u, turbulent kinetic energy k and the shear flow energy f for $t = 500 - 520s$.

In section 5.1 it was found that the first principal component had a similar sawtooth-like behaviour that was caused by the change of the pressure in the plasma edge. Considering the fact, that we removed this sawtooth-movement with the applied filter, this suggest that in section 5.4 the dynamics of the projection onto the k-f-plane was investigated rather than the whole dynamics of the full system. This might explain why two of the complex conjugate pairs showed good agreement in forward and backward time directions while the third pair did not give a consistent picture. It suggests that this third direction corresponds to the dynamics of the pressure gradient, which was almost removed by the filtering. In this context it is reasonable to have a closer look at the dynamics projected onto the k-f-plane.

Figure 55 shows the projection of the plasma trajectory onto the k-f-plane for case A. The position of the stable H-mode solution H_+ before and after the third heating pulse $t = 300s$ is indicated with arrows. The plasma trajectory spirals away from H_+ towards the attracting limit cycle. By spiraling the plasma trajectory follows an expanding limit cycle. Since the limit cycle expands towards the axes of this plane until it approaches them we have the picture of a homoclinic bifurcation in this plane, a mechanism suggested before by the analysis of the experimental data.

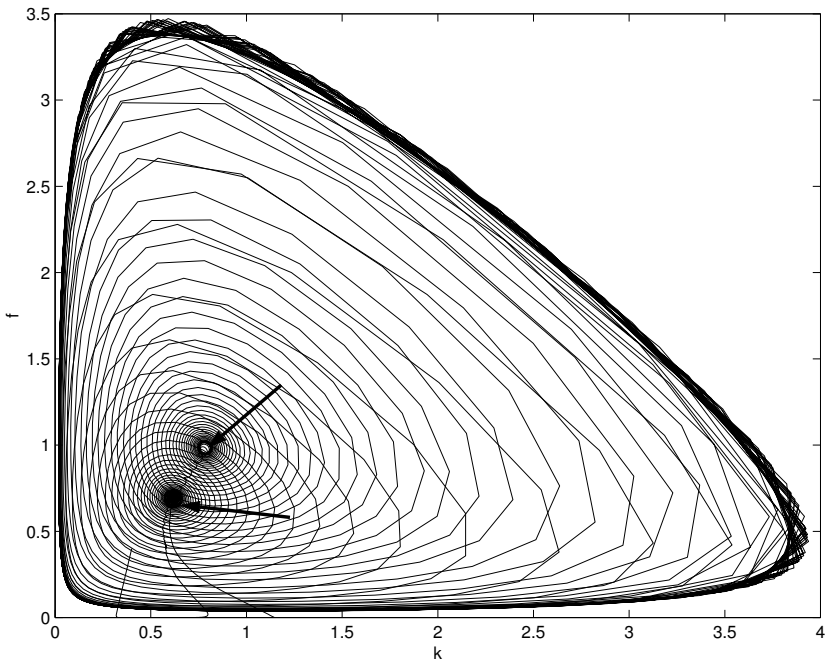

Figure 55: Projection of the plasma trajectory onto the k-f-plane. The position of H_+ before and after the third heating pulse is indicated with arrows.

If we linearize the projection of equations (120)-(122) onto the k-f-plane around $(k_0, f_0) = (0, 0)$, which actually is a fixed point in this plane, we get

$$\frac{d}{d\tau}\begin{pmatrix}\tilde{k}\\ \tilde{f}\end{pmatrix} = \begin{pmatrix}u^{1/2} & 0\\ 0 & -cm(u)\end{pmatrix}\begin{pmatrix}\tilde{k}\\ \tilde{f}\end{pmatrix} \tag{133}$$

where $k = k_0 + \tilde{k}$ and $f = f_0 + \tilde{f}$. The eigenvalues of (133) are given by

$$\lambda_- = -cm(u) \tag{134}$$
$$\lambda_+ = u^{1/2} \tag{135}$$

As expected the k-direction (the turbulent energy) is the unstable direction. The driving force of the instability is the pressure gradient $u^{1/2}$. The stable direction near the quasi fixed point (k_0, f_0) is the f-axis, the shear flow energy. This is consistent with experiments since the shear flow is the stabilizing force. The strength of the contraction onto the quasi fixed point is proportional to $m(u)$, the viscosity. Both the stable and unstable eigenvector are increasing with increasing u and thus are increasing with increasing heating power. This behaviour agrees very well with the results found in section 5.4, where the real parts of the stable and unstable eigenvalues were also increasing with increasing heating power. To make the comparison between the results of the Sugama and Horton model and the analyzed data complete we have to look at the saddle index of the quasi fixed point. The saddle index is given by

$$\delta = -\frac{\lambda_-}{\lambda_+} = \frac{cm(u)}{u^{1/2}} \tag{136}$$

Figure 56 shows the saddle index versus u for the cases A and B. For small pressure gradients $\delta > 1$. However for intermediate pressure gradients the saddle index drops below 1. Finally for high pressure gradients the saddle index becomes greater than 1. However we have to bear in mind, that the actual functional form of δ depends strongly on the functional form of $m(u)$, but the decrease for small pressure gradients and the increase for high pressure gradients, which coincides with small and high heating powers respectively, is common for all forms of $m(u)$, because of the experimentally found scaling formulas for $m(u)$. The same decrease-increase behaviour can be seen in the calculated saddle index of the measured data. For $t = 0.155s$ the saddle index is close to one. Between $t = 0.155s$ and $t = 0.165s$ it reaches a minimum much smaller than 1, before δ becomes greater than 1 for $t > 0.18s$.

Again this behaviour points towards a near homoclinic bifurcation as the mechanism for the stabilization of the H-mode, which leads to an ELM-free H-mode.

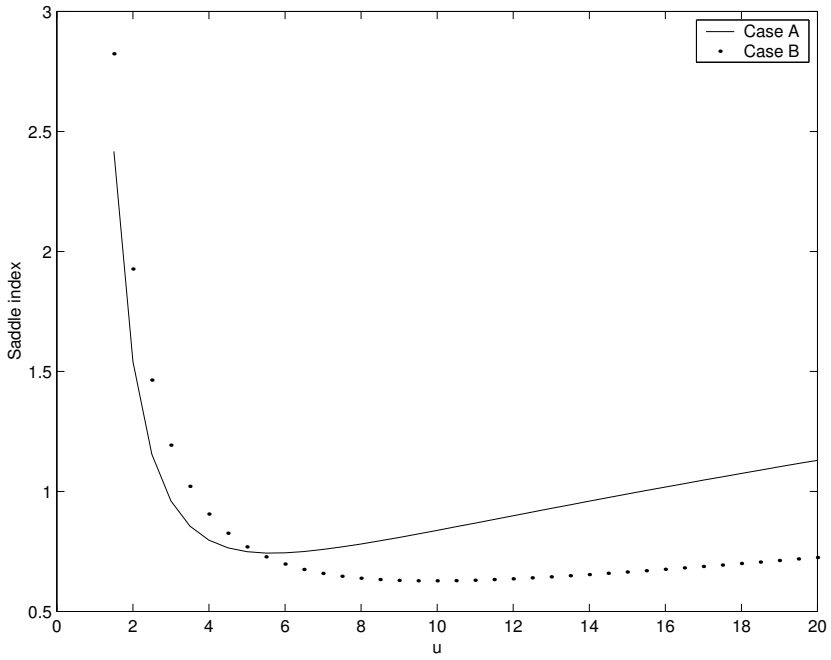

Figure 56: Dependence of the saddle index on the pressure gradient.

However, this explanation raises a fundamental question: what exactly is the H-mode? As mentioned above in all models the H-mode is treated as a fixed point which becomes unstable leading to ELMs. In contrast to this, the analysis above showed three different objects should be called H-mode. Shortly after the transition the plasma moves towards the stable H-mode solution, which justifies the naming of this solution. However for higher heating powers the plasma trajectory moves along an expanding limit cycle. On this limit cycle the turbulent energy decreases further (before ELMs) which would justify calling this limit cycle the H-mode. Finally this limit cycle undergoes a nearly homoclinic bifurcation, leading to the biggest decrease in the turbulence and a nearly unlimited increase in the pressure gradient. According to this the invariant line $(u, k = 0, f = 0)$ should be called H-mode.

Summarizing the comparison above we can say that - given this broader interpretation - the Sugama and Horton model contains all the results obtained from the COMPASS-D data. It gives a self-consistent description of the creation of the shear flow which cases the transition to the H-mode and expresses all coefficients in terms of dynamical variables of the model. However for $m(u)$ and $d(u)$ approximations have been used, since their correct functional form is not known. These functional forms on the other hand are very important since the properties of the model depend strongly on them. A further issue for future studies lies in the fact, that all low-dimensional models of the second class are almost identical

if the pressure gradient is fixed. Thus a good description of the pressure gradient and the incorporation of the pressure gradient into the remaining two equations for k and f seems to be the most important physical problem of the models and might lead to a better understanding of the L-H transition and the H-mode.

9 Conclusions

For the analysis of the transition from L- to H-mode and of the H-mode itself the poloidal field component of the magnetic field was analyzed. The singular value decomposition and nonlinear analysis of the data showed that during and after the transition at least four different plasma modes exist. For the separation of the modes a new filtering technique was developed and applied to the data. For each mode the local linear model was estimated using the method of delays. The calculation showed that the important parts of the dynamics of the modes is contained in a six-dimensional space.

To estimate the growth rates of the modes the data was divided into eight time windows and for each time window the local linear model was calculated. To identify real eigenvalues from spurious ones, caused by noise, the linear models have been calculated in forward and backward time. It turned out that four of the six eigenvalues agree quite well for both time directions while the other two give different results for the two time directions. This can be explained by the fact, that these two eigenvalues are connected with the pressure. However, since the saw-tooth like behaviour of the main plasma, which is directly connected to the plasma pressure, was removed by the filtering technique, most of the properties of the pressure may have also been removed from the data. The comparison of the estimated with theoretically calculated growth rates allows the identification of the plasma modes that are causing the ELMs. The analysis showed that the growth rates of the modes increase with time. However a further investigation of the dependence of the growth rates on plasma parameters like electron temperature or density could not be done, since the corresponding measurements are not available for the analyzed discharge.

The stationary plasma solution, which is a fixed point in the six-dimensional space, is a saddle with one unstable and two stable directions. The saddle index, which determines whether the saddle is attracting or repelling trajectories, shows that the saddle repels at the beginning of the transition but becomes attracting during the transition. In addition to the saddle fixed point an attracting limit cycle exists. This limit cycle expands in size and moves towards the saddle fixed point to form a near homoclinic bifurcation. The experimentally observed ELMs can be explained as the trajectory of the plasma around this limit cycle. The period between successive ELMs increases with increasing size of the limit cycle until they nearly vanish in the case of the near homoclinic bifurcation.

In order to check the validity of these results a comparison with existing models was done. Most of these models depend on two partial differential equations for the plasma pressure and the plasma velocity, which are split up into an equilibrium part and a fluctuating part. These equations have two important limitations. Since the equilibrium parts are treated as parameters in these models, no

equation for the time evolution of these quantities is given. However this equation is very important since the equilibrium parts change during the transition and during the ELMs. The second problem arises from the lack of a heating term in the equations. This lack becomes more significant since for most of the low-dimensional models derived from these equations it has been necessary to arbitrarily add a heating term to their equations.

The low-dimensional models can be divided into two classes. The first class reproduces the basic qualitative behaviour in the sense that it shows the transition from the initially stable L-mode to the stable H-mode, when a critical condition is fulfilled. When a second critical condition is fulfilled the H-mode becomes unstable and oscillations appear, which are called ELMs in these models. However these ELMs are almost regular oscillations and do not show the experimentally observed pulse-like oscillations of ELMs. The second class of the low-dimensional models introduces new physics, not contained in the partial differential equations, into their equations. Common features of this class are the use of a heating term, and that the models are almost identical when the pressure gradient is fixed. From this class the most promising candidate for the description of the L-H transition was identified, the Sugama and Horton model.

The ELMs of the Sugama and Horton model show the right pulse-like behaviour. In addition the model shows the same behaviour for the growth/decay rates and the saddle index as found for the COMPASS-D data. A further feature of this model is the existence of a limit cycle which undergoes an almost homoclinic bifurcation. Because of this the period between successive ELMs increases and the plasma appears quasi stable. However this stable behaviour can only be found for the turbulent energy and the shear flow energy. The pressure gradient increases during these quasi stable periods, which is also consistent with measurements.

The results obtained in the earlier sections gives rise to a very important conceptual question: what is the H-mode? In this report it was shown that three different objects have the properties of the H-mode and it can be justified to call each of them the H-mode. The answer to this question is an interesting problem for future studies.

References

[1] F Wagner et al., Regime of Improved Confinement and High Beta in Neutral-Beam-Heated Divertor Discharges of the ASDEX Tokamak, Phys. Rev. Lett. 49, (1982) 1408

[2] R J Goldston, P H Rutherford, Introduction to Plasma Physics, IOP Publishing Ltd 1995

[3] J Hugill, Edge turbulence in tokamaks and the L-mode to H-mode transition, Plasma Phys. Control. Fusion 42 (2000) R75-R91

[4] P H Diamond, Y M Liang, Self-Regulating Shear Flow Turbulence: A Paradigm for the L to H Transition, Phys. Rev. Lett. 72, 2565 (1994)

[5] J W Connor, H R Wilson, A review of theories of the L-H transition, Plasma Phys. Control. Fusion 42 (2000) R1-R74

[6] S J Fielding et al., H-modes on COMPASS-D with high-power ECRH, Plasma Phys. Control. Fusion 40 (1998) 731-735

[7] D M Thomas, State Transitions, Hysteresis, and Control Parameters on DII-D, 25th EPS Conference on Controlled Fusion and Plasma Physics

[8] K H Burrell, Effects of ExB velocity shear and magnetic shear on turbulence and transport in magnetic confined devices, Phys. Plasmas 4, (1997) 1499

[9] J W Connor, Edge-localized modes-physics and theory, Plasma Phys. Control. Fusion 40 (1998) 531-542

[10] J W Connor, A review of models for ELMs, Plasma Phys. Control. Fusion 40 (1998) 191-213

[11] H Zohm, Edge localized modes (ELMs), Plasma Phys. Control. Fusion 38 (1996) 105-128

[12] H Zohm, The physics of edge localized modes (ELMs) and their role in power and particle exhaust, Plasma Phys. Control. Fusion 38 (1996) 1213-1223

[13] A L Colton, L Porte, Correlation between ELMs and the Edge Plasma Profiles during the L-H Transition in JET, JET-C(93)10

[14] A L Colton et al., ELM studies on the COMPASS-D tokamak, Plasma Phys. Control. Fusion 38 (1996) 1359-1365

[15] O. Klüber, H. Zohm, et al., MHD Mode Structure and Propagation in the ASDEX Tokamak, Nucl. Fusion 31 (1991) 907

[16] G P King, R Jones, D S Broomhead, Phase portrait from a time series, Nucl. Physics B, 2 (1987) 379-390

[17] T Eickermann, K H Spatschek, Anomalous particle transport in a low-temperature plasma without magnetic shear, Phys. Plasmas 3, (1996) 2869-2878

[18] D S Broomhead, G P King, Extracting qualitative dynamics from experimental data, Physica D 20 (1986) 217-236

[19] A M Albano, J Muench, C Schwartz, A I Mees, P E Rapp, Singular-value decomposition and the Grassberger-Procaccia algorithm, Phys. Rev. A 38 3017 (1988)

[20] M B Kennel, R Brown, H D I Abarbanel, Determining embedding dimension for phase-space reconstruction using geometrical construction, Phys. Rev. A 45, 3403-3411 (1992)

[21] J P Eckmann, D Ruelle, Fundamental limitations for estimating dimensions and Lyapunov exponents in dynamical systems, Physica D 56 185 (1992)

[22] W E Han et al, Spectral characteristic of edge magnetic turbulence in COMPASS-D, Plasma Phys. Control. Fusion 43 (2000) 181-201

[23] R Vautard, P Yiou, M Ghil, Singular-spectrum analysis: A toolkit for short, noisy chatic signals, Physica D 58 (1992) 95-126

[24] H Kantz, T Schreiber, Nonlinear time series analyis, Cambridge University Press 1997

[25] O Akman, Non-linear time series analysis of congenital nystagmus waveforms, Departments of mathematics and optometry and neuroscience UMIST

[26] T. Dukok de Wit, A.-L. Pecquet, J.-C. Vallet, The biorthogonal decomposition as a tool for investigating fluctuations in plasmas, Phys. Plasmas 1 (10), 1994

[27] P G Carolan et al, Charactersitics of Ohmic H-modes in COMPASS-D, Plasma Phys. Control. Fusion 36 (1994) A111-A116

[28] C. Nardone, Multichannel fluctuation data analysis by the singular value decomposition method. Application to MHD modes in Jet, Plasma Phys. Control Fusion 34 1447 1465

[29] D S Broomhead, G P King, On the qualitative analysis of experimental dynamical systems, Nonlinear Phenaomena and Chaos 113-144, Adam Hilger Ltd 1986

[30] P L Read, Phase portrait reconstruction using multivariate singular systems analysis, Physica D 69 (1993) 353-365

[31] P Mantica, G Vayakis, J Hugill et al., Broadband fluctuations and particle transport in the edge plasma during ECRH in DITE, Nucl. Fusion, Vol 31, 9 (1991)

[32] J J Healey, Identifying finite dimensional behaviour from broadband spectra, Physics Letters A 187 (1994) 59-66

[33] M J Powell, The Theory of Radial Bisis Function Approximation in 1990, Numerical Analysis Reports, University of Cambridge

[34] C A Micchelli, Interpolation of scattered data: distance matrices and conditionally positive definit functions, Constr. Approx., Vol. 2 (1986) 11-22

[35] N Aubry, P Holmes, J L Lumley, E Stone, The dynamics of coherent structures in the wall region of a turbulent boundary layer, J. Fluid Mech 192 (1988) 115-173

[36] J Thompson, H Stewart, Nonlinear Dynamics and Chaos, 1986 John Wiley & Sons

[37] T Chiueh et al., Effects of a radial electric field on tokamak edge turbulence, Phys. Fluids 29 (1986) 231

[38] K Itoh, S I Itoh, Model of L-H transition in Tokamak, Phys. Rev. Lett. 60 (1988) 2276

[39] K C Shaing, E C Crume, Bifurcation Theory of Poloidal Rotation in Tokamaks: A Model for the L-H Transition, Phys. Rev. Lett. 63 (1989) 2369

[40] M Tendler, Different scenarios of transition into improved confinement, Plasma Phys. Control. Fusion 39 (1997) B371-B382

[41] P Beyer, K H Spatschek, Center manifold theory for the dynamics of the L-H-transition, Phys. Plasmas 3 (1996) 995-1004

[42] O Pogutse et al., The resistive interchange convection in the edge of tokamak plasmas, Plasma Phys. Control. Fusion 36 (1994) 1963-1985

[43] G Hu, W Horton, Minimal model for transport barrier dynamics based on ion-temperature-gradient turbulence, Phys. Plasmas 4 (1997) 3262-3272

[44] A Takayama et al., Comparison of Lorenz type and plasma fluid models for nonlinear-interchange-mode generation of shear flow, Plasma Phys. Control. Fusion 40 (1998) 775-778

[45] H Sugama, W Horton, Shear flow generation by Reynolds stress and suppression of resistive g modes, Phys. Plasmas 1 (1994) 345-355

[46] H Sugama, W Horton, L-H confinement mode dynamics in three-dimensional state space, Plasma Phys. Control. Fusion 37 (1995) 345-362

[47] P H Diamond et al., Self-Regulating Shear Flow Turbulence: A Paradigm for the L to H Transition, Phys. Rev. Lett. 72 (1994) 2565-2568

[48] V B Lebedev et al., A minimal dynamical model of edge localized mode phenomena, Phys. Plasmas 2 (1995) 3345- 3359

[49] S Hamaguchi, Anomalous transport arising from nonlinear resistive pressure driven modes in a plasma, Phys. Fluids B 1 (1989) 1416

[50] J W Connor, Invariance Principles and Plasma Confinement, Plasma Phys. Control. Fusion 30 (1988) 619